GaN TECHNOLOGIES FOR MICROWAVE HEATING AND BROADBAND RECEIVER APPLICATIONS

by

MEGAN CERIDWEN ROBINSON

B.S., University of Colorado Boulder, 2018

M.S., University of Colorado Boulder, 2020

A thesis submitted to the

Faculty of the Graduate School of the

University of Colorado in partial fulfillment

of the requirements for the degree of

Doctor of Philosophy

Department of Electrical and Computer Engineering

Spring 2023

Committee Members:

Dist. Prof. Zoya Popović

Prof. Gregor Lasser

Prof. Taylor Barton

Prof. Vadim Yakovlev

Prof. Cresten Mansfeldt

Prof. Peter Aaen

Robinson, Megan Ceridwen (Ph.D., Electrical Engineering)

GaN Technologies for Microwave Heating and Broadband Receiver Applications

Thesis directed by Distinguished Professor Zoya Popović

This thesis entitled, “GaN Technologies for Microwave Heating and Broadband Receiver Applications,” consists of two parts. Part I discusses galium nitride (GaN) for high-power transmitters used in a solid-state microwave waste-to-fuel reactor. As the global population is producing and consuming more, there is a worldwide need for more efficient methods of reducing, reusing, recycling, and upcycling produced waste. Pyrolysis for municipal solid waste is investigated through a scalable solid-state microwave heating cavity. The detailed analysis of different power combining methods at 2.45 GHz was covered in the comprehensive exam and will be briefly summarized in this defense.In Part II, the high-power handling and linearity of GaN is examined for use in RF receivers. Broadband receivers are susceptible to interference and a large interfering signal can saturate multiple systems including the low noise amplifier, mixer, and analog to digital converter. Interference suppression circuits using GaN tunable delay lines are explored for suppressing out-of-band interfering signals. Multiple hybrid 2-4 GHz tunable notch boards were designed, fabricated, and characterized for this study. This defense will focus onanalog interference suppression circuit design and performance

DEDICATION

To my parents, my sisters, my advisor, my friends and all those who helped support me through this process. Zoya thank you so much for putting in so much time and care into helping me grow as a researcher, scientist, and person. Your dedication to your students and this field has been an unfathomable resource and inspiration during the past seven years. To my family without your understanding and support I could not be here today, I don't have the words to express how much you mean to me. Martin thank you for helping me during the writing process and with every aspect of life outside of work these past few months, I am so excited to see where the future takes us. I want to personally express my appreciation for the group chat that made me laugh throughout every moment of this journey. Each of you has helped me have the confidence to make the decision that got me here in research and in life. The coffee chats, long walks, and weekend gatherings got me through the hard times of grad school. For my non-PhD friends thank you for letting me take space to focus on prelims, paper deadlines, comps, and thesis writing. I love you all for never thinking less of me for focusing on my studies and sometimes being a less than great friend. To Paige, Jack, and Laila thank you for the spending the late nights in lab doing measurements and paper revisions, I am not a morning person and thank you for understanding and working with me. To all of those that will never read this, I have grown so much as a person since I started my graduate studies and you helped me through this process in thanks to you. Finally, if you are reading this thank you because caring about this work and growing upon it is why we do research.

ACKNOWLEDGMENTS

Advisor: Professor Zoya Popović

Ph.D. Committee: Professor Gregor Lasser, Professor Taylor Barton, Professor Vadim Yakovlev, Professor Cresten Mansfeldt, and Professor Peter Aaen.

Institutions/Sponsors: University of Colorado Boulder, DARPA, Lockheed Martin, GAANN fellowship, NSF, WiN Semiconductors, and Qorvo.

Colleagues: Paige Danielson, Jack Molles, Jose Estrada, Shane Verploegh, Laila Marzall, Aman Samaiyar, Akim Babenko, Tim Sonnenberg, Rob Streeter, Erik Kwiatkowski, Pattrick Blum, Maxwell Duffy, Mauricio Pinto, Philip Zureck, Allison Duh, Caitlyn Cooke, Amy Robinson, Connor Nogales, Seth Johannes, Tony Romano,Jooeun Lee, Alec Russell, Sofia Mvokany, Reyes Lucero, Stefan Stroessner, Kaitlin Hall, Georgia Sandidge, and Gabriel Santamaria.

University of Colorado Boulder staff: Adam Sadoff, Jarka Hladisova, Lori Meehan, Patricia Femrite.

Special thanks to Professor Dana Anderson.

CONTENTS

List of Tables

LIST OF FIGURES

CHAPTER 1

INTRODUCTION

This thesis consists of two parts, both using wide bandgap galium nitride (GaN) semiconductor technology. Part I introduces an application for GaN for high-power transmitters, while Part II focuses on a receiver application. In Part I microwave pyrolysis for waste-to-fuel conversion is investigated. Waste-to-fuel conversion is currently being used in both civilian and military settings as a waste management solution. The goal of this project is to demonstrate a scalable system for waste-to-fuel conversion that can be more portable than the current truck-sized or larger options. Solid-state GaN power amplifiers sources are used to investigate the system benefits of efficient circuit and spatial power combining. The advantage of GaN for transmitter power amplifiers is in the high power density of GaN HEMTs, as well as convenient impedances that can result in broadband circuits through relatively straightforward matching network design. Along with the 70 W power amplifier design, the cavity parameters are investigated through full wave and multiphysics simulations to understand the heating and evaluate performance of the system. An efficiency estimate and heating measurements are done for personal sized 1.4 and 5.2 L systems. Both single stream and mixed waste heating measurements demonstrate the control of heating uniformity through the use of relative phase control with spatially combined sources. Part II covers the implementation of a GaN based interference suppression, where the high power handling enables receivers that can operate in the presence of high power interferers. Interference signals are problematic for receivers as they can saturate or destroy receiver

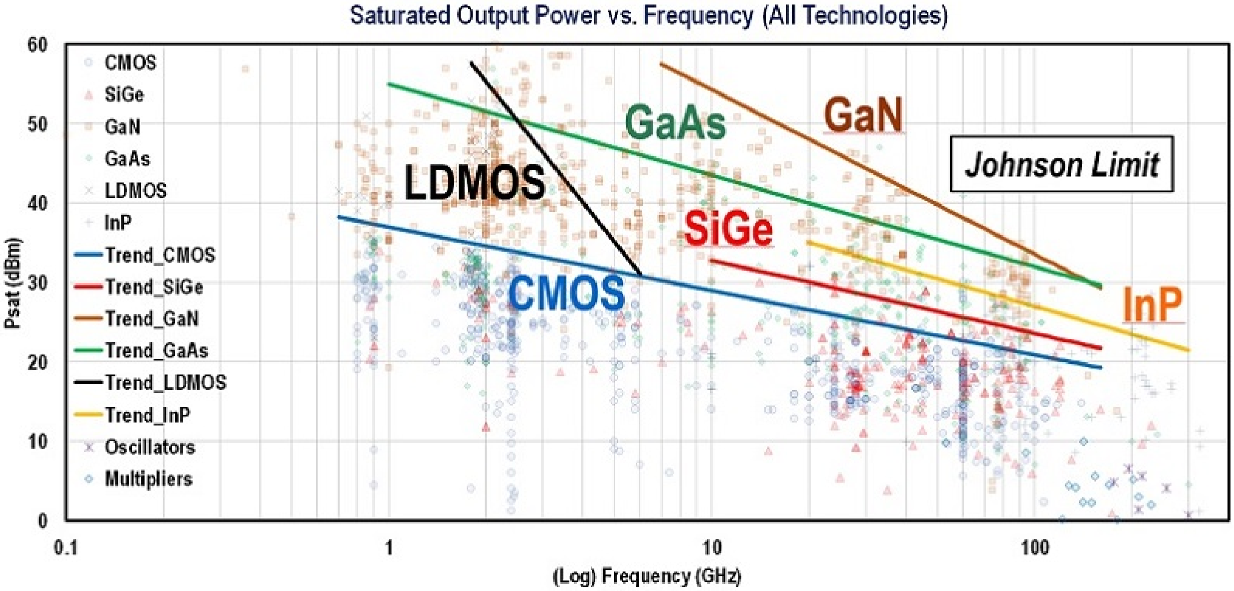

Figure 1.1: A comparison of trends in output power capabilities of a variety of technologies from [15].

components, i.e. LNA, mixer or ADC. Broadband receivers are particularly susceptible to interference. Part II presents 2–4 GHz interferometer based interference suppression circuits designed to suppress high power interferers. This introductory chapter highlights the most relevant properties of GaN and summarizes the transmit and receive parts of the thesis.

1.1 Overview of Current GaN Technologies for Microwave Applications

High electron mobility transistors (HEMT) are nonlinear devices formed by a junction between materials with different band gaps and are useful for RF design due to high-frequency performance and lower noise values than other transistor technology. HEMTs are commonly fabricated using III-V semiconductors, of which Gallium Arsenide (GaAs), Gallium Nitride (GaN), and Indium Phosphate (InP) are the currently common process technologies. InP heterogenous electron mobility transistors (HEMTs) and InP heterojunction bipolar transistors (HBT) are more prevalent in the high millimeter-wave and terahertz (THz) frequency ranges, with GaAs HEMTs also showing low noise. Figure 1.1 shows how the output power of different technologies perform over frequency with GaN out-performing all the other technologies above 5 GHz.

In addition to the high output power GaN also performs better than GaAs and Silicon (Si) in a few other

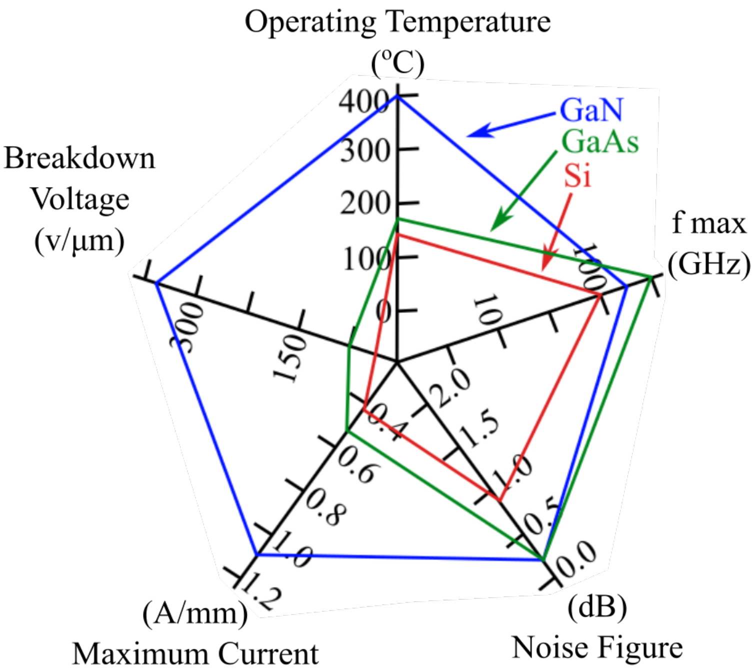

Figure 1.2: GaN, GaAs and Si technologies in the microwave frequency range, with tradeoffs in maximum operating frequency, operating temperature, breakdown voltage, maximum current, and noise figure [16].

key metrics such as operational voltage, maximum current, and operating temperature, depicted in Fig. 1.2. GaAs and GaN are reported to have similar noise figures, but GaAs has usually been preferred for low-noise amplifiers (LNAs) due to the lower cost. However, GaN receivers can handle significantly higher input power, making them more linear when large interference signals are present. Additionally, the potential of fully integrating PAs and LNAs on the same chip becomes more attractive as GaN technology matures.

The high voltage operation/breakdown make GaN better than other technologies for power handling, impedance matching for high powers, and linearity, which is discussed in later sections. In terms of impedance matching, the simple relationship between RF power and supply voltage voltage can give an insight into impedances. For example, using $P = V^2/R$ for a 100 W device operating at 25 V supply, the resistance of the device is approximately 6.3 Ω. This is much higher than the resistance for comparable-power LDMOS devices, and easier to match 50 Ω over a wider bandwidth. At a supply voltage of 50 V, the resistance for the same output power becomes 25 Ω, which is easy to match to and improves overall efficiency. The high power density of GaN allows for fewer devices and therefore less combining for more power and efficiency, Fig. 1.3.

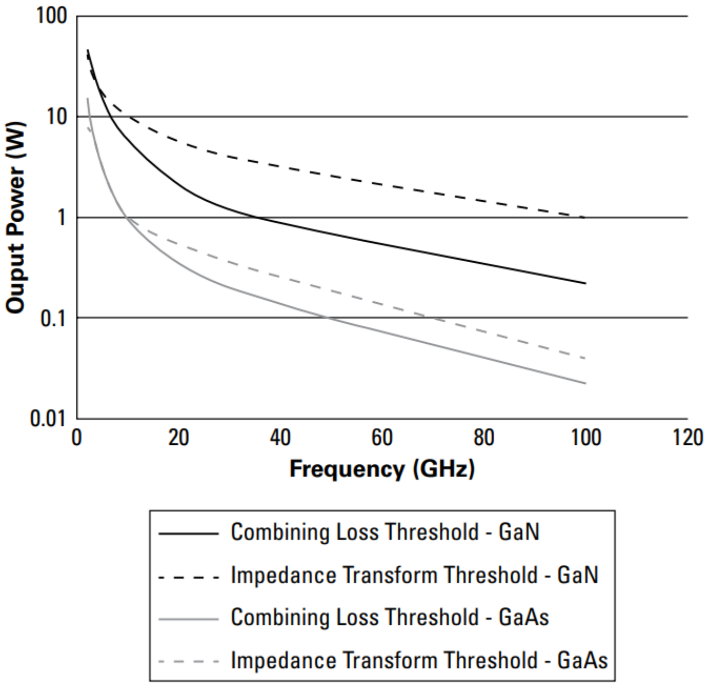

Figure 1.3: A comparison of the power capabilities of GaAs and GaN technologies (from [17].

1.2 Thesis Outline

In Part I the high power output of GaN is investigated for use in a solid-state microwave waste to fuel reactor. This topic is investigated through a scalable solid-state microwave heating cavity. Part I of the thesis is organized as follows:

- Chapter 2 presents some background in waste processing, and highlights advantages of microwave pyrolisis for this application. This chapter also presents a high-level theory of mixed-waste heating, and quantifies the total energy balance and efficiency for a microwave waste-to-fuel system for various waste materials.

- Chapter 3 expands on the microwave heating analysis and presents eigenmode, driven modal, and FDTD multiphysics simulations of a 1.4 L cavity.

- Chapter 4 introduces the measurement setup to explore the simulated conclusions and compare to measured heating results. These experiments cover multiple materials for single and multiple excitations with experimental variations that show improvement from the simulated cavity set-up.

- Chapter 5 explores future work on the microwave heating cavity including: volume scaling; and frequency modulation and modified boundary conditions for improving field uniformity.

The high power handling and linearity of GaN for use in RF transceivers is explored in Part II, through the use of GaN tunable delay lines for analog interference suppression circuits (AISCs) and a comparison of GaAs and GaN delay-line based phase shifters. Part II of the thesis is organized as follows:

- Chapter 6 provides a background in interference suppression techniques, and also introduces the theory behind the operation of the AISC.
- Chapter 7 presents a simplified theory for an ideal interferometer circuit used as a basis for two branch and four branch interometers for interference suppression.
- Chapter 8 covers the design and performance of the 2–4 GHz GaN MMIC delay lines used in the AISC architecture. A uniformly-loaded lumped element transmission line with HEMTs configured as variable capacitors is compared to a non-uniform design in terms of tunability, match, loss and group delay across the octave.
- Chapter 9 presents two hybrid AISCs using the above delay lines, and designed for notching a single interfering signal. The tuning of the notch is measured across frequency in small-signal operation. Additionally, the high power operation and linearity of the two circuits is examined with multiple simultaneous tones.
- Chapter 10 expands the applicability of variable delay line circuits to phase shifters and to higher frequency (28 GHz) delay lines. In particular, a comparison of the GaN loaded-line phase shifters with their GaAs counterparts is shown both theoretically and experimentally, demonstrating the higher linearity of GaN.
- Chapter 11 explores other avenues for future work, specifically an extension of the AISC topology to a dual-notch tunable response, with integrated LNAs. This demonstrates (a) the extension to suppressing

more than one interfering signal and (b) the ability of the architecture to provide low-noise gain at the front end receiver.

In summary, this thesis presents two microwave front end applications that use unique properties of GaN technology, with Part I focusing on an efficient narrowband high-power transmitter used in waste processing, and Part II focusing on interference suppression for broadband receivers with high linearity.

Chapter 2

Part I: Microwave Pyrolysis; Introduction and Background

2.1 Introduction

As the global population is producing and consuming more, there is a worldwide need for more efficient methods of reducing, reusing, recycling, and upcycling the produced waste. Excess waste is becoming a global issue, as many countries in the third world are running out of landfill space and low-quality plastic is often sent back from recycling plants to the country of origin [23, 24], as seen in Fig.2.1(a). This figure also shows one of many photographs of ocean waste, which is difficult to process after collection since it is wet and salty [25], and requires washing and drying, which in turn uses fresh water and energy. In 2018, the United States produced 292.4 million tons of municipal solid waste equivalent to 4.9 pounds of waste per person per day. Of the municipal waste generated, approximately 69 million tons were recycled and 25 million tons were composted, equivalent to a 32.1% recycling and composting rate [20]. This is an increase from the 268.7 million tons generated in 2017 and the 208.3 million tons in 1990, as shown in Fig.2.2. Fig.2.3 shows the percentage of different types of municipal waste, showing that the largest fractions are from paper/cardboard and food, which motivates the investigation into a solid-state microwave pysolysis

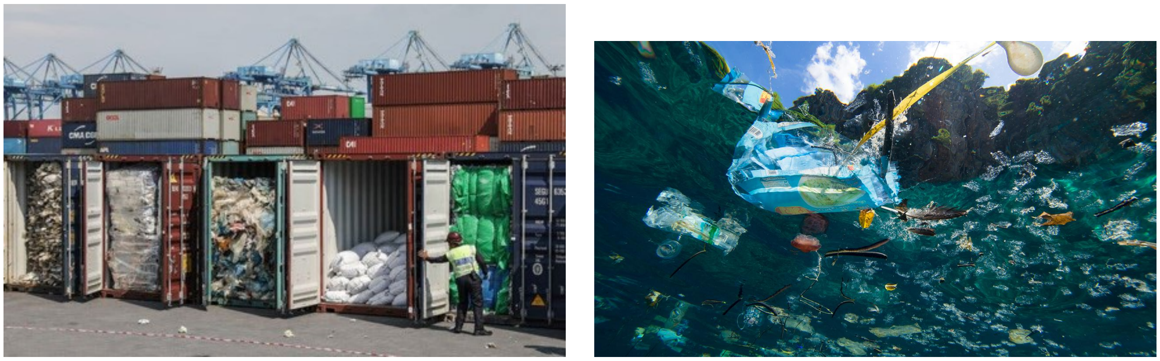

(a) (b)

Figure 2.1: (a) Imported plastic waste in cargo containers at Port Klang in Malaysia waiting to be returned to its country of origin [18]. (b) Photo of ocean waste that is difficult to process for recycling [19].

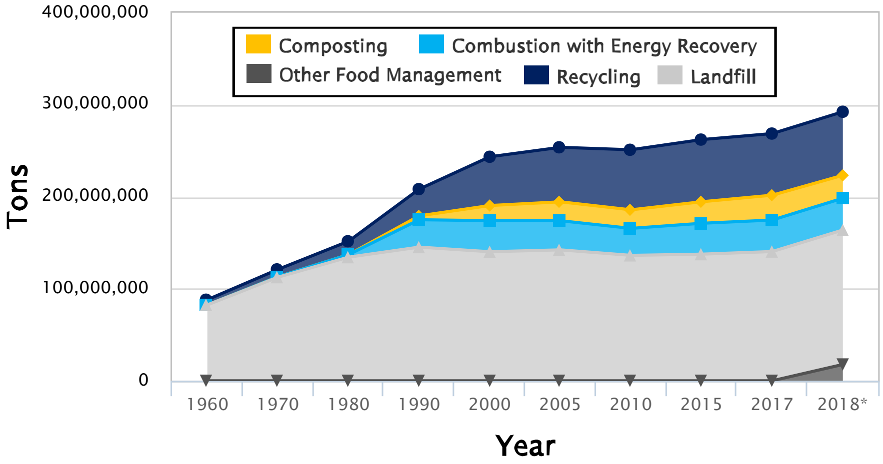

Figure 2.2: Growth of municipal waste in the US from 1960 through 2018 according to the Environmental Protection Agency (EPA) [20].

reactor.

In addition to municipal waste problems, military waste is a significant portion of total national waste, e.g. the average soldier produced about 8 lbs/soldier/day in 2016 [21]. This amount of waste is problematic for smaller stealth missions, temporary smaller bases, or naval activities where space is limited. Most current waste-management systems are not taking full advantage of energy resources contained in the waste. To utilize the energy stored in the waste materials, thermochemical processes such as pyrolysis, incineration, gasification, etc., are currently in use in both municipal and military sectors. These methods are used to generate energy, typically heat and electricity, from waste material [26–28]. Incineration and gasification directly use the breakdown of the material to generate electricity [27]. This can be more efficient on large scales for generating electricity, but do not as efficiently scale down to smaller volumes.

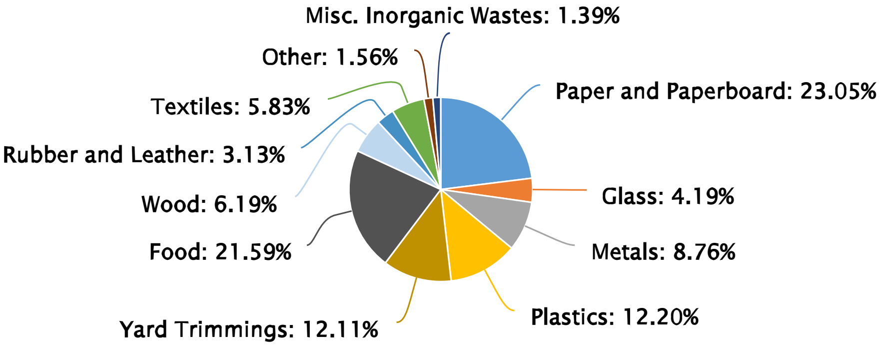

Figure 2.3: Percentage of different materials that constitute municipal waste in the US based on the most recent available data in 2018 from the Environmental Protection Agency (EPA) [20].

In the US Navy, the waste is compressed or shredded and needs to be stored or thrown overboard. For example, the USS John C. Stennis aircraft carrier produced 100,000 lbs of plastic, 3000,000 lbs of metal and glass and 200,000 lbs of cardboard waste in 2011 [29]. This was incinerated using JP-5 jet fuel. In submarines, the waste can be pumped or blown out into the ocean and poses a large security risk, while some of the waste needs to be stored on board. In the US Army, a large-scale gasification system processes 3 tons of waste per day and this battalion-size facility requires 26 kW to operate. The Tactical Garbage to Ethanol Refinery (TGER) system, developed at Purdue University [27] uses incineration to produce synthetic gas (Syngas) fuel and processes 1 ton/day. Typical incineration and gasification systems are large and do not scale efficiently to smaller volumes. An incinerator deployed on a military base in Afghanistan is shown in Fig.2.4, along with a TGER system which is the size of a truck.

The goal of this research is to investigate a scalable waste-to-fuel conversion method that can scale in terms of waste volume, from the currently used systems to a portable version. In this investigation microwave pyrolysis at the scale of personal trashcan, 1.4 L is used for determining the benefits of different power combining methods. Pyrolysis is “the thermochemical decomposition of organic material at high temperature and in the absence of oxygen or in an atmosphere of inert gases” [30] and does not directly process the waste for energy production, but converts it into intermediary compounds that can be used for chemical up-conversion to solid fuel, oil, SynGas [31], or environmentally safe products that can be used for fertilization [32]. Pyrolysis has been investigated for feasibility in the municipal solid waste (MSW) sector, where convection-based heating methods for a wide variety of materials have been used, e.g. wood [33],


(a) (b)

Figure 2.4: Photographs of two waste to energy converters used by the military. (a) Two 8-ton capacity incinerators at Forward Operating Base Salerno [21]. (b) The Tactical Garbage to Ethanol Refinery (TGER) built at Purdue University for use by the US Army [22].

paper [34], textiles [35], mixed food [36], and plastics [37]. These materials are common in municipal waste in most areas, as shown in Fig.2.3, and are therefore the main focus of research in this thesis.

Most published experiments on pyrolisis use non-electrical energy sources, or do not mention the energy usage of the heating apparatus and rather focus on improvements to the chemical outputs and conversion method. Limited work with microwave heating has shown improvement in thermal efficiency, increased speed of reactions, and, in some cases, advantageous modifications of the breakdown process [38]. Electromagnetic waves generate heat inside the medium, improving the system efficiency by reducing the amount of heat dissipated outside of the waste material compared to convection heating. Microwave heating has been shown to be much faster than conventional electric heating in hydrothermal treatments [39]. Most microwave industrial heating is done with magnetrons (100 W – 35 MW) in the 915 MHz and 2.4 GHz Industrial, Scientific and Medical (ISM) bands, and the frequency is not easily tunable nor are mulitple magnetrons easily injection-locked for power combining [40]. Small and even hand-held solid-state microwave ovens using LDMOS devices have been demonstrated [41]. RF systems include one or more feeds that monitor the absorbance of the electromagnetic energy in the cavity and provide real-time adjustments to the RF energy output. These adjustments have the potential for precise energy application and better heating for variety of different foods. Since solid-state devices can operate continuously, a 500 W solid-state setup can replace an

1100 W magnetron pulsed source, meaning that these systems have the potential to be more energy efficient. In 2016 multiple solid-state RF ovens, the Dialog, Wayv Adventurer, and Midea ovens, were announced for release in 2017. However, no commercially available systems for the home market have appeared in the United States prior to 2022, with the Wayv Adventurer and Midea ovens not being released and having no communication of progress since 2016 [42]. The current market for solid-state ovens are in systems where high reliability and heating control are required, but are currently too expensive for use in everyday household applications.

The first part of this thesis focuses on a 2.45-GHz active microwave cavity with solid-state (GaN) spatially power-combined sources for scalable waste volumes, as illustrated in Fig. 2.5. Many aspects of this system have been explored including cavity volume scaling, frequency modulation, waste mixture properties, modified boundary conditions (frequency selective surfaces (FSS)), and feeding methods for a variety of materials.

2.2 Microwave Heating Theory

Heating materials with electromagnetic waves at microwave frequencies is a result of energy absorption in the material due to its high-frequency conductivity, σ that converts microwave energy into heat. In a home microwave oven heating is performed at Industrial, Scientific and Medical (ISM) frequencies of 2.45 GHz or 915 MHz, in a shielded rectangular metal cavity which is larger than a wavelength in each dimension. Such a loaded electrically-large cavity is over-moded, implying that many modes are superimposed together and the electromagnetic field distribution is complicated and not uniform. The heating rate and temperature distribution depend on the thermal properties of the material and field distribution in the cavity. The field distribution depends on the power, frequency, cavity geometry, boundary conditions, feeding method, and loading, as well as the complex permittivity. Another important factor is the penetration depth of the field into the material and here the standard dispersive skin depth, $\delta = 1/\sqrt{\pi f \sigma \mu}$, for a plane wave can be used as a guideline for penetration depth of the field into a given material. However to get a more accurate idea of the field strength within the volume in an over-moded cavity filled with a lossy dielectric

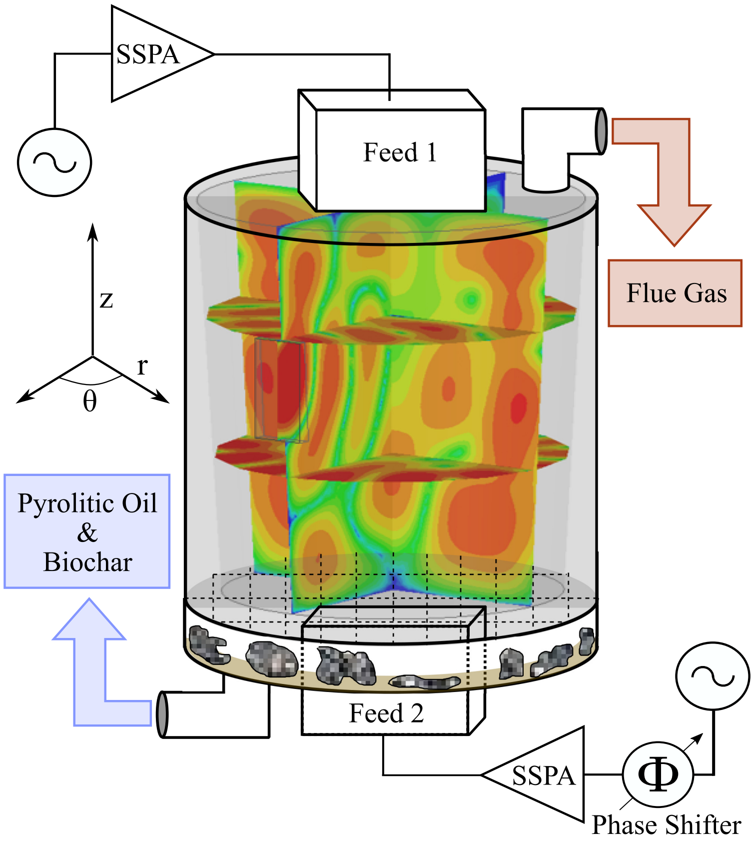

Figure 2.5: Block diagram of an active microwave cavity reactor for waste to fuel conversion. The cavity is fed by several solid-state power amplifiers (SSPAs) with waveguide probes and in several configurations, discussed in later chapters. Absorption of microwave energy results in waste conversion into solid fuel: biochar; pyrolitic oil which can be converted to liquid fuel; and flue gas which can be converted to synthetic gas fuel (SynGas).

material, full-wave simulations are needed and should be coupled with thermal simulations which include temperature-dependent material properties.

2.2.1 Electrical and Thermal Properties of Some Waste Materials

Electrical and thermal properties of typical waste materials at 2.45 GHz and 25°C are shown in Table 2.1, showing the variation in relative permittivity (ϵ_r), conductivity (σ), specific heat (c), mass density (ρ), and thermal conductivity (κ). Here the complex permittivity is $\epsilon = \epsilon_0 \epsilon_r - j\sigma/\omega$. The parameters for the materials used in the following efficiency analysis are highlighted with bold text in the table.

Table 2.1: Table of typical material properties at 2.45 GHz and 25° [1–10]

Material	Percentage of Waste [43]	ϵ_r	σ [$\frac{\text{mS}}{\text{m}}$]	c [$\frac{\text{kJ}}{\text{Kkg}}$]	ρ [$\frac{\text{kg}}{\text{m}^3}$]	κ [$\frac{\text{W}}{\text{Km}}$]
Wood	29.8	1.2-2.1	4.9-8.6	1.3-2.4	400-750	0.15-0.19
Plastics	7.6	2-3.5	1.3-2.4	1.3-1.9	540-800	0.03-0.5
Textiles	3.4	1.4-6	3.8-16.3	1.6	560	0.03-0.25
Paper	11.9	2.5	10.2	1.336	80-190	0.05
Starches	N/A	30	2042	3.7	1050	1
Fruit & Veg.	N/A	4.6	31.3	3.8-4.1	840-1320	0.3-0.7
Bread	N/A	3.1-4.2	40-105	4.5	200	0.1
Meat	N/A	50-65	2000-2600	2.7-3.7	960-1060	0.4-0.5
LDPE and Polystyrene	**N/A**	**2.25**	**.092**	**2.3**	**950**	**0.28**
Textiles	**3.4**	**3.0**	**0.12**	**0.33**	**1100**	**0.05**
Food Mixture	**10.9**	**42**	**1710**	**1.7**	**950**	**0.85**
Paper	**11.9**	**2.2**	**9.0**	**0.33**	**1150**	**0.05**

2.3 ENERGY BALANCE ESTIMATION

In the energy balance calculations, the input energy into the system consists of the waste chemical energy and the dc electrical energy used to obtain the RF power with an efficiency that can reach 70% for kW power levels. The efficiency of RF power conversion to heating rate in the waste mass is calculated from full-wave simulations for four waste mixtures, input power, and operating temperature. The output energy estimates are collected from various pyrolysis process descriptions, e.g. [30], with the total energy being that of the solid fuel (biochar) (35 MJ/kg) and liquid fuel (oil) caloric values, e.g. 40 MJ/kg for plastics and about 10-15 MJ/kg for non-plastics [37] Another byproduct is flue gas, which can be converted to synthetic gas fuel (Syngas) as described in, e.g. [44].

2.3.1 DC TO RF CONVERSION

The two methods to obtain kW-level power at GHz frequencies are solid-state power amplifiers and tubes. In the 2 GHz range, GaN shows impressive efficiencies at high powers demonstrated with a PA at 1.315 GHz having 83.7% PAE at 127 W output power [45] and a 238 W PA with 71.4% PAE at 2.45 GHz [46]. The devices can be further power combined, both through circuit and spatial combing methods to achieve higher powers with similar efficiencies. Magnetrons have also been power combined with power combining efficiencies above 90% to achieve power levels around 30 kW [47]. The analysis in this chapter is not specific to a particular type of RF power generation, and is described by a conversion efficiency which is assumed to be 70%, a reasonable assumption for this narrowband frequency.

2.3.2 Field Simulations

In this initial study Ansys HFSS is used for both the electric and thermal simulations. The fields inside the waste volume produce heat through Joule losses. The material properties are assumed to be constant over temperature, which is not a good assumption since during breakdown the material changes substantially. However, the change in properties will depend on the waste composition which is difficult to predict. It is important to note that even without chemical breakdown, the waste material properties change over temperature, which is observed experimentally and discussed further through multiphysics modeling in the next chapter. The thermal power produced in the cavity depends on the filling material properties, relative permittivity (ϵ_r), conductivity (σ), geometry of cavity and type of excitation, as discussed previously and is calculated at discrete points from:

$$P_{Th} = \sum_{k=0}^{n} \sigma |E(x, y, z)|^2 \Delta v \tag{2.1}$$

where $E(x, y, z)$ is the magnitude of electric field found from full-wave simulations and is defined by the mesh in the finite-element numerical code. The volume of each element in the summation Δv come from the simulation finite mesh size. Ideally the smallest Δv is chosen so the summation approaches the actual integral expression. The choice of a mesh size to accurately represent the system while maintaining efficient simulation time and computational resources is key to good simulations. It is desirable to keep the power density of Joule losses uniform through the heating process, because that usually results in the best time-average efficiency and chemical conversion. The analysis is done using a single waveguide port excitation. The cavity size is important as larger cavities support more modes helping improve uniformity, but have less penetration further into the cavity reducing the heating rate away from the excitation probe. Several rectangular and cylindrical cavities, with volumes ranging from 0.0008 m^3 to 0.15 m^3, were compared using a full-wave eigen-mode solver (Ansys HFSS) to determine the modal content around the operating frequency

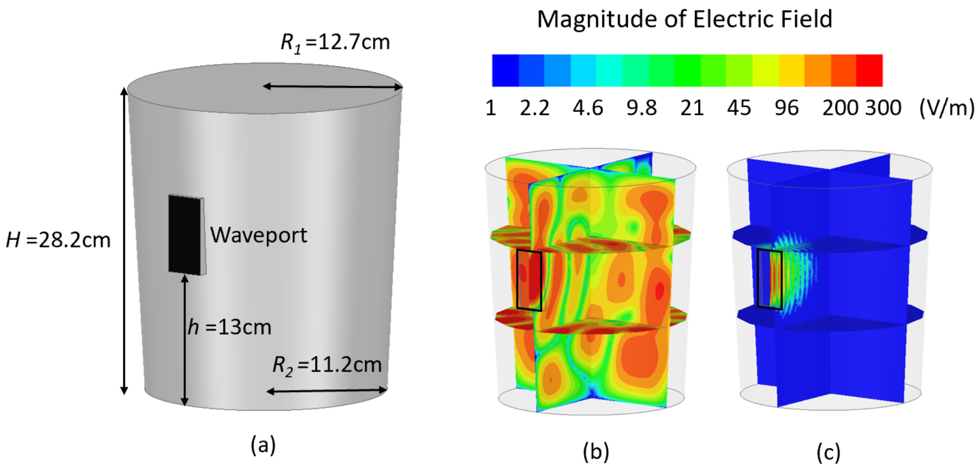

Figure 2.6: Simulated magnitude of the electric field for a single waveguide port excitation of a cavity completely filled with various materials. (a) Simulated cavity with dimensions labeled. (b) Cavity filled with LDPE and polystyrene $\epsilon_r = 2.25$ and $\sigma = 0.09$ mS/m, and (c) cavity filed with food mixture $\epsilon_r = 42$ and $\sigma = 1.7$ S/m. The field value is normalized to a 1 W incident power at 2.45 GHz on waveguide port.

of 2.45 GHz. The chosen cavity has the volume close to that of an actual 5.2 L trash-can, cylindrical in shape, Fig.2.6. For the simulations, the radii of the bases are chosen to be $R_1 = 12.7$ cm and $R_2 = 11.2$ cm, with a height of $H = 28.2$ cm. The feed is an S-band (WR340) waveguide port with a lower edge 13 cm above the bottom of the cavity. The feed location is chosen through a parametric sweep with different loadings to determine modal coupling.

The fields can be found using a full-wave EM solver, given a specific geometry, electrical properties, and excitation. Plots of the magnitude of the electric field throughout the cavity are shown for two extremes of the four cases in Fig. 2.7. The breakdown of the food mixture is not detailed in reference [35] and for this analysis a mixture of 45% meats and starches, 35% fruits and vegetables, and 20% fats was assumed. If the materials are uniformly mixed with particle sizes smaller than a wavelength (at least a tenth of a wavelength or smaller so that scattering from the individual materials is negligible) the mixture behaves as a single dielectric with ϵ_{eff}. To determine the effective dielectric parameters of the mixed waste, the Maxwell-Garnett formula with the Bruggeman approximation is used as follows:

$$\sum_i v_i \frac{2\epsilon_{ri} - \epsilon_{eff}}{\epsilon_{ri+2\epsilon_{eff}}} = 0, \tag{2.2}$$

where ϵ_{eff} is the effective relative permittivity that is found based on known mixture parameters relative

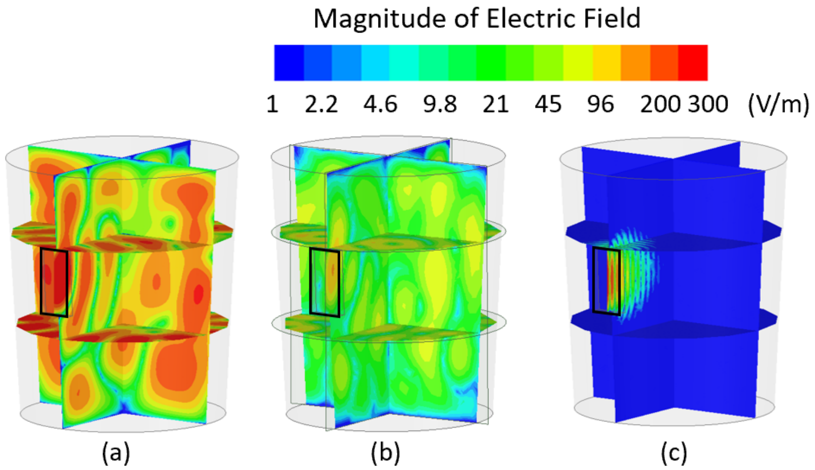

Figure 2.7: Simulated magnitude of the electric field, with 1 W incident power at 2.45 GHz, inside cavities completely filled with (a) LDPE and Polystyrene, ϵ_r of 2.25, $\sigma = 0.09$ mS/m, thermal conductivity of $\frac{\mathrm{W}}{\mathrm{m}^\circ\mathrm{C}}$, density of 950 $\frac{\mathrm{kg}}{\mathrm{m}^3}$ and specific heat of 2300 $\frac{\mathrm{J}}{\mathrm{kg}^\circ\mathrm{C}}$, (b) Textiles, ϵ_r of 3, $\sigma = 0.12$ mS/m, thermal conductivity of 0.05 $\frac{\mathrm{W}}{\mathrm{m}^\circ\mathrm{C}}$, density of 1100 $\frac{\mathrm{kg}}{\mathrm{m}^3}$ and specific heat of 0.33 $\frac{\mathrm{J}}{\mathrm{kg}^\circ\mathrm{C}}$, (c) Food mixture, ϵ_r of 42, $\sigma = 1.7$ S/m, thermal conductivity of 0.85 $\frac{\mathrm{W}}{\mathrm{m}^\circ\mathrm{C}}$, density of 950 $\frac{\mathrm{kg}}{\mathrm{m}^3}$ and specific heat of 1.7 $\frac{\mathrm{J}}{\mathrm{kg}^\circ\mathrm{C}}$, and (d) Paper, ϵ_r of 2.2, $\sigma = 9.0$ mS/m, thermal conductivity of 0.05 $\frac{\mathrm{W}}{\mathrm{m}^\circ\mathrm{C}}$, density of 1150 $\frac{\mathrm{kg}}{\mathrm{m}^3}$ and specific heat of 0.33 $\frac{\mathrm{J}}{\mathrm{kg}^\circ\mathrm{C}}$.

permittivity, ϵ_{ri}, and the volume fraction, v_i, of each material. Equation 2.2 was solved for the effective complex permittivity of the food mixture used in the field simulations. The food mixture, with high permittivity and loss, shows high absorption near the feed with low field penetration away from the feed. Adding multiple excitations would improve the uneven heating due to the distance from the feed. Notice that the low-density polyethylene, LDPE, and polystyrene mixture, low permittivity and loss, has high electric field magnitude throughout the cavity. Despite the high field magnitude the low loss of the material limits the power that can be absorbed and reduces the heating generation.

2.3.3 THERMAL HEATING RATE SIMULATIONS

The electrical and chemical processes that occur when there is an electromagnetic field inside a material are linked through the heating rate caused by Joule losses as:

$$\sigma|E(x,y,z)|^2 = \rho c \frac{d}{dt}\mathrm{T}(x,y,z) - \nabla \cdot (\kappa \nabla \mathrm{T}(x,y,z)), \tag{2.3}$$

where ρ is the mass density of the filling material, c is the specific heat of the material, $\mathrm{T}(x,y,z)$ is the temperature at a specific point within the material, and κ is the thermal conductivity. An analytical solution

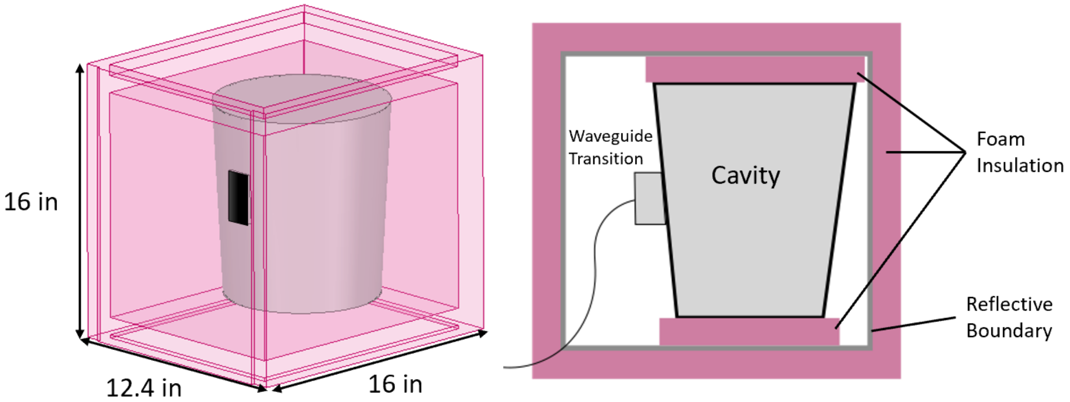

Figure 2.8: Image of thermal simulation set up and a side cut of the insulation used in the simulation. The cavity filling is coupled to the field simulation as a thermal source. The cavity walls are 1 mm thick tin-plated steel, the reflective surround has a reflectivity of 94% and the foam insulation is 1 in thick XPS rigid polystyrene.

for the heating rate is complicated since the temperature and electric field are functions of position. Therefore, multi-physics simulations (Ansys Workbench) are used to determine the temperature increase due to Joule losses and account for the anticipated thermal energy leakage through the cavity walls with thermal insulation as shown in Fig. 2.8.

Using Ansys Workbench to connect the electromagnetic field data from Ansys HFSS as a thermal excitation in Ansys Mechanical, the heating rates for the different loading materials are determined for several input power levels and two internal cavity operating temperatures, the results are shown in Table 2.2. These are used to make an estimation of the RF power needed to obtain the specified heating rate required for pyrolysis processes.

Table 2.2: Simulated heating rates for given material input power and temperature

Material	Input RF Power (W)	Heating Rate at 25°C/min	Heating Rate at 400°C/min
LDPE and Polystyrene	500 3000	0.8 5	0.01 1
Textiles	500 3000	16 75	14 65
Food	500 3000	100 650	90 600
Paper	500 3000	44 320	40 310

2.3.4 Pyrolysis Process

The approximation for input materials, output materials, and process requirements for the system are obtained from four reference papers [34–37] which describe pyrolysis for various materials. The cited experiments, with input parameters detailed in Table 2.3, deal with slow pyrolysis systems that are sealed and operated without catalysts over one hour or longer time periods.

Table 2.3: Input parameters for several pyrolysis examples with single materials

Material	Input Caloric Value (MJ/kg)	Heating Rate (°C/min)	Duration of Heating (min)	Max Temperature (°C)	Time as Max Temp. (min)
LDPE and Polystyrene	44	10	40	425	60
Textiles	28	5	105	550	60
Food	15.7	10	52	500	240
Paper	13.6	10	85	873	60

The compounds, composition, and corresponding caloric values of the chemical outputs for the various pyrolysis processes were determined in the references using spectroscopic methods. A summary of the chemical outputs for each process are summarized in Table 2.4.

Table 2.4: Output Parameters for Pyrolysis

Material	Gas Caloric Value (MJ/kg)	Percent Weight Gas (%)	Oil Caloric Value (MJ/kg)	Percent Weight Oil (%)	Biochar Caloric Value (MJ/kg)	Percent Weight Biochar (%)
LDPE and Polystyrene	50.8	10	40.4	89.5	N/A	0.05
Textiles	N/A	45.44	11.49	24.7	31.73	13.28
Food	0.22	7.41	8.01	32.29	7.55	60.3
Paper	N/A	15.0	21.8	19.0	11.7	43.0

From this table, some interesting conclusions can be made.

- The type of material changes which output is prefered, e.g. plastics convert efficiently to oil and food to biochar.
- The temperature and and duration of heating are dependent on the input waste material. This is not necessarily fixed at the values presented here and there is ongoing research on optimizing these

chemical reactions.

- The experiments were using small batches to reduce the effects of non uniform heating: food waste 150-270g, textiles 100g, plastic 10g, paper 100g. For scaling to larger volumes the heating parameters and output materials may change.
- Mixing different materials together will change the outputs and the heating parameters with more research investigating these effects being needed for efficient energy conversion.

2.3.5 Total Efficiency

Four different waste materials and mixtures are analyzed and the conversion efficiencies are calculated for filled cavities with dimensions as in Fig.2. The input and output parameters from Tables 2.3 and 2.4 are used for the material inside the cavity. The CW RF power required for each waste material to attain the heating rates from Table 2.3 are estimated by extrapolating the applied power and heating rate simulations from Table 2.2. Assuming a 70% dc to RF efficiency the dc power is calculated for each material. The calculated RF input powers range from 8 kW for food, 15 kW for the textile, 20 kW for paper, and 60 kW for the LDPE and polystyrene fillings. The dc energy is computed by multiplying the dc power by the operating times in Table 2.3. The conversion efficiency is defined as

$$\eta = \frac{\mathrm{W_{Ch,OUT}}}{\mathrm{W_{Ch,IN}} + \mathrm{W_{DC}}}, \tag{2.4}$$

where $\mathrm{W_{Ch,OUT}}$ and $\mathrm{W_{Ch,IN}}$ are the output and input chemical energies, and $\mathrm{W_{DC}}$ is the input dc electrical energy. Fig. 2.7 shows the simulated electric field magnitude for the 4 cases at 2.45GHz, and Table 2.5 summarizes the calculated efficiency using equations 2.1, 2.3, and 2.4.

From these calculations, the following conclusions can be made:

- For all cases the estimated dc energy is lower than the output chemical caloric values, making it worth while to convert the waste material instead of throwing it away.
- The plastics have the highest conversion efficiency due to the high caloric value of the output product that could be increased with an improved microwave heating system.

Table 2.5: Summary of Full System Efficiencies

Material	Input Caloric Value (MJ/kg)	Output Caloric Value (MJ/kg)	DC Energy Value (MJ)	Conversion Efficiency (%)	Output Energy Compared to DC Energy (%)
LDPE and Polystyrene	545	548	96.8	85.4	566
Textiles	480	121	26.1	23.9	464
Food	202	92	12.2	43.0	754
Paper	136	92	16.0	60.5	575

- The textiles had the worst conversion efficiency though the gas byproducts which made up 45% of the output material were not captured and used for the energy calculation.
- The food mixture conversion efficiency can be greatly improved given that over half of the RF power was reflected off of the feed port and never delivered into the material.

In summary, this chapter provides motivation for investigating solid-state microwave pyrolisis of mixed waste. These results are preliminary and did not take into account the temperature material properties and non-uniform heating effects, though they show promise for an efficient system and motivate continued work in this area. The next chapter continues with detailed electromagnetic and thermal simulations for three waste materials which completely fill a smaller volume personal trash-can. These simulations are then compared with experiment, and mixed waste is also investigated both in simulations and measurements using different solid-state source configurations.

The material from this chapter is reported partially in [48] which details the efficiency estimate.

CHAPTER 3

MICROWAVE CAVITY ANALYSIS

3.1 INTRODUCTION

To better understand and improve upon the initial one-port simulations used in the previous chapter, an analysis of heating rates is presented. Additionally, various simulations of a 1.4 L cavity using eigenmode and driven analysis, as well as a multiphysics approach are performed. Some modifications of the cavity feeding are also performed in order to improve heating uniformity throughout the waste volume.

3.2 MICROWAVE HEATING THEORY

Heating materials with electromagnetic waves at microwave frequencies is a result of absorption in the material due to its high-frequency conductivity, σ. As an example to understand the heating steps the approximate heating of a cup of salt water in a household microwave is described. For a 100 mL volume of uniform material with $\sigma = 5\,\mathrm{S/m}$ and specific heat of $c = 3.899\,\mathrm{J/g}$ (salt water), exposed uniformly, 163 W of microwave power is required to raise the temperature by 75 K in 3 minutes. Heating is usually performed in a shielded metal cavity which is larger than a free-space wavelength in each dimension at ISM frequencies of 2.45 GHz or 915 MHz. Such a loaded electrically-large cavity is over-moded, implying that the electromagnetic field distribution is complicated and not uniform. The heating rate and temperature distribution depend on modes that are excited in the cavity, which in turn depend on frequency and both the real and imaginary parts of the complex permittivity of the material being heated, the notation used here is $\epsilon = \epsilon_0\epsilon_r - j\sigma/\omega$ where the dielectric loss is denoted using a frequency dependent σ instead of other notations using ϵ''. The standard skin depth for a plane wave can be used as a guideline for penetration depth of the field into a given material, but in an over-moded cavity filled with a lossy material, full-wave simulations are needed to determine the field strength within the volume, and should be coupled with thermal simulations which include temperature-dependent material properties.

3.2.1 Expanded heating theory with temperature dependent material properties

Heat conservation within the cavity can be written as:

$$\frac{\mathrm{d}\mathcal{E}_{\mathrm{TH}}}{\mathrm{d}t} = -\nabla \cdot \vec{\Phi}_{\mathrm{H}} + Q, \tag{3.1}$$

where Q is the energy of heat, $\vec{\Phi}_{\mathrm{H}}$ is the heat flux and the thermal energy, $\mathcal{E}_{\mathrm{TH}}$, given by

$$\mathcal{E}_{\mathrm{TH}} = c(r, \phi, z, T)\rho(r, \phi, z, T)T(t) + C, \tag{3.2}$$

where other energy stored in the material is absorbed into the constant C. Cylindrical coordinates, (r, ϕ, z), are used to match the experimental cavity geometry. Here we assume that the materials do not undergo phase or chemical changes over the temperature range considered ($C = 0$), and that the heat flux is caused by conduction only and is described by Fourier's law for an isotropic medium:

$$\vec{\Phi}_{\mathrm{H}} = -\kappa(r, \phi, z, T)\nabla T. \tag{3.3}$$

The heat generation, Q, comes from Joule losses, with a power density at any point in the waste volume given by:

$$Q = p_{\mathrm{J}}(r, \phi, z) = |\vec{E}(r, \phi, z)|^2\sigma(r, \phi, z, T), \tag{3.4}$$

where $\vec{E}(r, \phi, z)$ is the electric field, and $\sigma(r, \phi, z)$ is the spatially-varying conductivity. From (1), solving for the temperature increase gives:

$$\frac{\partial}{\partial t}T(r,\phi,z) = \frac{p_\text{J}(r,\phi,z,T) + \nabla\cdot(\kappa(r,\phi,z,T)\nabla T(r,\phi,z))}{\rho(r,\phi,z,T)c(r,\phi,z,T)}. \tag{3.5}$$

To solve these equations numerically, the composition and spatial variation of the mixed waste needs to be known. Even for a single material, the moisture content and density will vary. To compare measurements to theory, single-material cavity loading is investigated, with cardboard/paper, bread and meat (hotdog), which represent a wide range of dielectric properties and do not produce toxic gases when heated.

3.3 Microwave Cavity Simulations

A 1.4 L shorted metal cylinder with a base diameter of 12.5 cm and height of 11.2 cm is used as the heating cavity, and completely filled with representative waste material. Multiple setups are investigated one with a single waveguide probe and the others with two probes to couple RF energy into the cylindrical cavity. Two rectangular waveguide probes are placed symmetrically on the two cavity flat walls. This arrangement gives the option of relative feed rotation, with multiple feeding options depicted in Fig. 3.1.

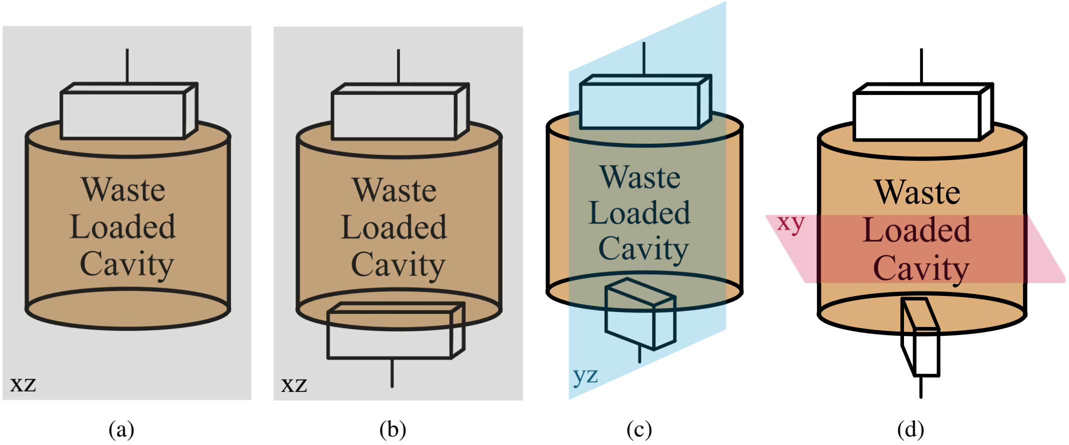

Figure 3.1: (a) Cylindrical cavity with single feed on top, showing the xz cut. (b) Cylindrical cavity with feeds on top and bottom oriented in the same polarization, showing the xz cut. (c) Cylindrical cavity with feeds on top and bottom oriented with 45° relative polarization, showing the yz cut. (d) Cylindrical cavity with feeds on top and bottom oriented with 90° relative polarization, showing the xy cut.

At 2.45 GHz, the cavity is single-moded when air-filled, but supports 3, 5 and more than 20 modes with uniform paper, bread and meat loading, respectively. The field amplitudes from eigenmode (unfed) analysis using Ansys HFSS are given in Fig. 3.2a for paper and in Fig. 3.3a for bread, showing the mode that is closest (within 250 MHz) to 2.45 GHz. The plots show the vertical, xz in Fig. 3.1(a), cross-section of the cylindrical cavity ($r = -6.25$ to 6.25 cm, $z = 0$ to 11.2 cm). As expected, the field profiles are quite different for the two loadings.

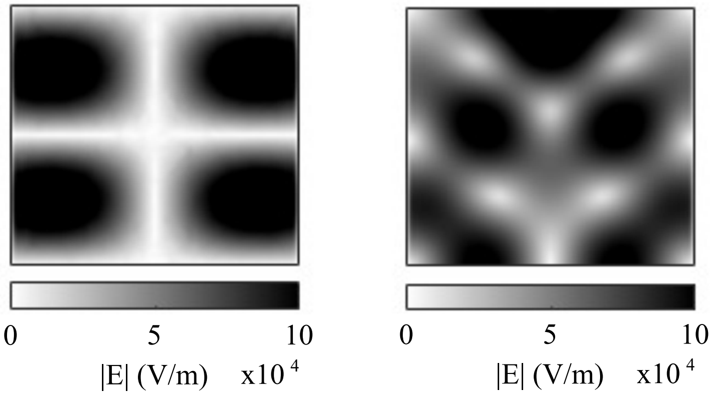

(a) (b)

Figure 3.2: (a) Eigenmode simulations for the electric field magnitude in a cylindrical cavity with a diameter of 12.5 cm and height of 11.2 cm, loaded with paper, showing the single mode closest to 2.45 GHz normalized to 1 J of stored energy. (b) Driven simulation for the electric field magnitude in the cavity for a single WR340 rectangular waveguide probe excited with 70 W delivered power. Results for the central xz cross-section of the cylindrical cavity are shown.

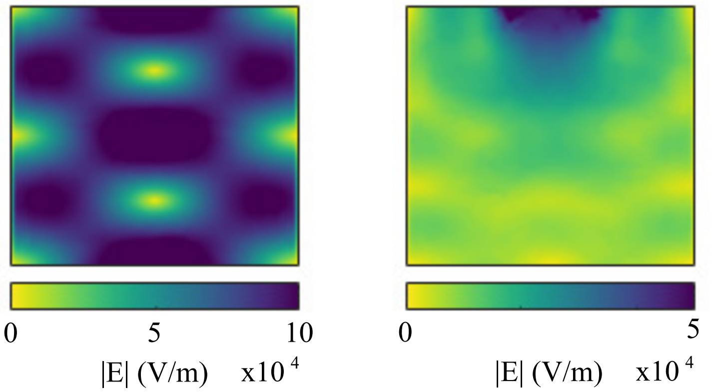

(a) (b)

Figure 3.3: (a) Eigenmode simulations for the electric field magnitude in a cylindrical cavity with a diameter of 12.5 cm and height of 11.2 cm, loaded with bread, showing the single mode closest to 2.45 GHz normalized to 1 J of stored energy. (b) Driven simulation for the electric field magnitude in the cavity for a single rectangular waveguide probe with 70 W delivered power. Results for the central xz cross-section of the cylindrical cavity are shown.

A driven analysis with a single S-band (WR340) waveguide-to-coaxial adaptor feed is performed for

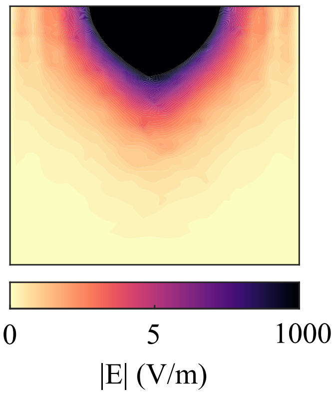

Figure 3.4: Driven simulation for the electric field magnitude in the cavity loaded with meat for a single waveguide probe excited with 70 W delivered power. Results for the central xz cross-section of the loaded cylindrical cavity are shown with the single waveguide excitation at the top of the cavity.

all three uniform loadings, showing that multiple modes are present. The results for paper are shown in Fig. 3.2b, for bread in Fig. 3.3b, and for meat loading in Fig. 3.4. In all three cases, the highest field values are near the feed, but in the case of the lower-conductivity paper the field is more uniformly distributed throughout the volume. As expected, increased loss occurs near the feed for the most conductive loading (meat), with several orders of magnitude lower field at the opposite side of the cavity. From these plots, the motivation for including multiple feeds becomes obvious.

From equation 3.4, the Joule loss density in the materials is proportional to the square of the field magnitude and the conductivity. It is interesting and practically relevant to note that the loss density is more uniform across different materials than the electric field magnitude. Fig. 3.5 shows simulation results using a driven analysis in HFSS for three excitations: two circuit-combined PAs feeding a single waveguide probe; two probes fed by two PAs in phase; and two probes fed by two PAs out of phase. The loss power density distribution is affected dramatically for the paper and bread loadings, but not for the highly conductive meat loading.

It is interesting to visualize the electric fields in the middle horizontal cut of the cavity ($z = 5.6$ cm, $r = 0$ to 6.25 cm, $\theta = 0$ to 2π). The two feeds can be oriented parallel to each other, or at some angle. Fig.3.6 shows the Joule loss density for paper and bread loading, for the parallel and 45° feed orientation. Although the 45° orientation results in a higher nonuniformity, the produced heat is significantly higher for both loadings.

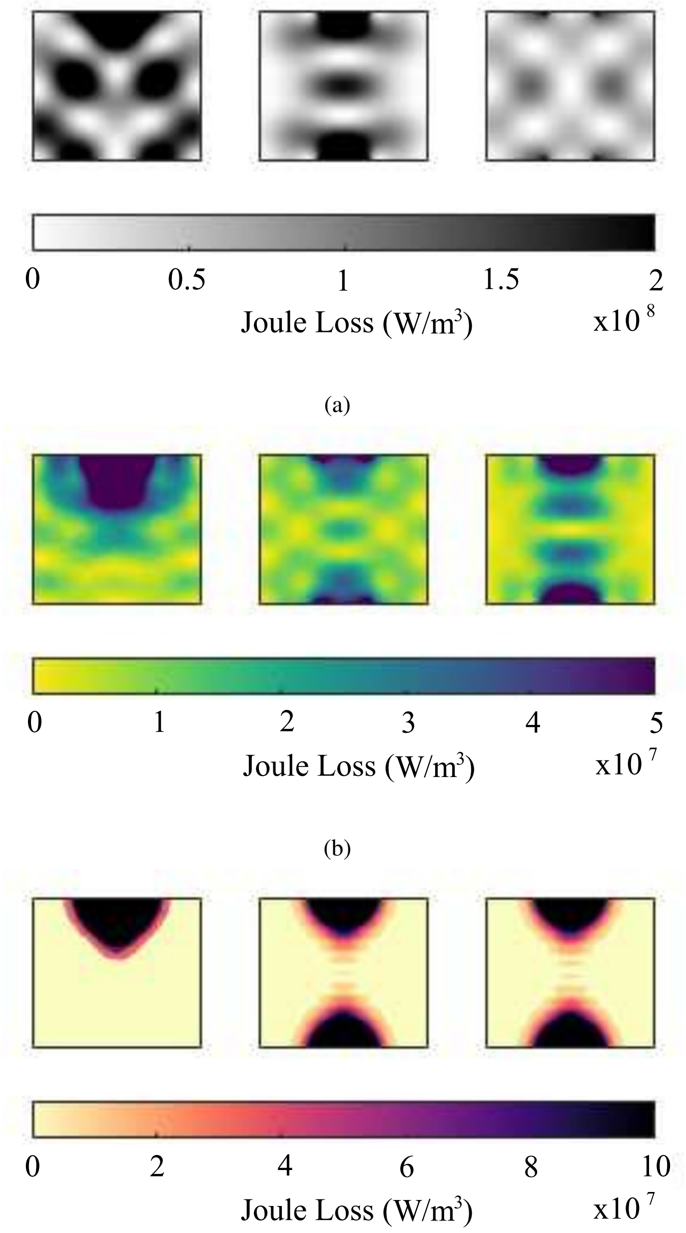

(a)

(b)

(c)

Figure 3.5: Driven simulation for the Joule loss in the cavity for uniform bread loading and different excitations. Left: Single waveguide probe excited with 70 W delivered power. Center: Two waveguide probes driven in phase with half of the applied power per probe. Right: Two waveguide probes driven 180° out of phase with half of the applied power per probe, for (a) paper, (b) bread, and (c) meat loadings. In all plots, results for the central xz cross-section of the loaded cylindrical cavity are shown.

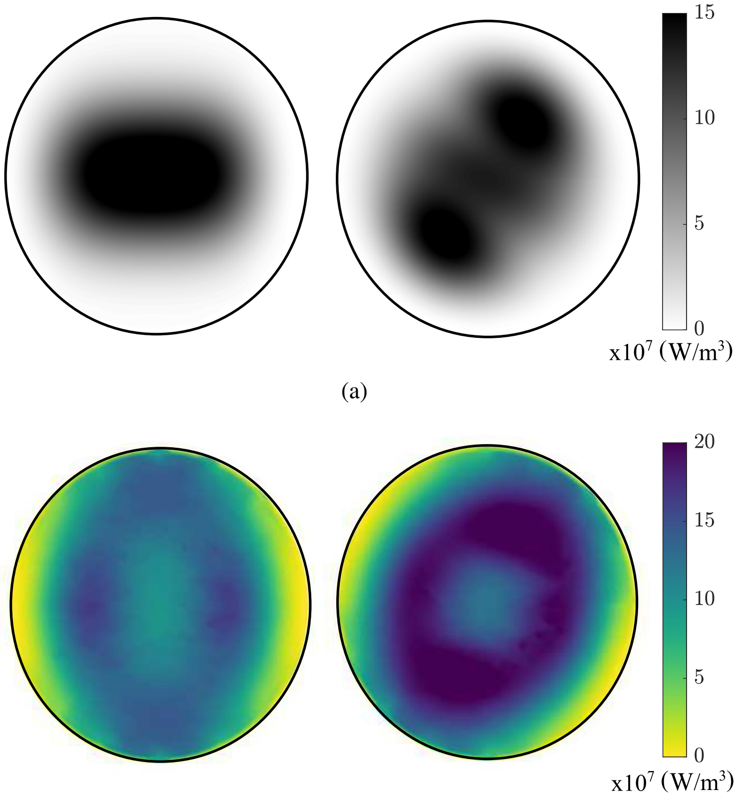

(a)

(b)

Figure 3.6: Joule loss volume energy density in the horizontal middle xy cross-section for (a) paper and (b) bread uniform loading with two feeds oriented parallel (left) and 45°(right) to each other for 70 W of total delivered power.

3.3.1 Multiphysics Simulations for Microwave Heating

The electric field distribution, and therefore Joule loss density, can be determined through full-wave electromagnetic simulations, and used in above equations to solve for the thermal evolution. However, this approach does not take temperature dependent material properties into account [49]. Measurements at 2.45 GHz of both inorganic [50] and organic materials often show changes in relative permittivity and conductivity with increasing temperature. The relative permittivity of various meats, chicken, beef, and salmon, has been characterized over temperaturemeat [10]. With measured relative permittivity of beef dropping from 55 to 51 when temperature increases from 15 to 55°C. The conductivity increases (less than 5%) above about 25°C.

A multiphysics approach which couples electromagnetic and thermal simulations is required to gain insight into the efficiency of heating and for improved cavity and probe design. This can be addressed using the 3D Finite-Difference Time-Domain (FDTD) technique for substances with temperature-dependent electromagnetic and thermal material parameters following the approach outlined in [11, 13, 14]. The EM and thermal solvers operate as parts of an iterative procedure in which a steady state solution of the EM problem becomes an input for the thermal simulator, which then computes the temperature field induced after a pre-set heating time step. After each iteration, material parameters are upgraded in every cell of the FDTD mesh in accordance with the output temperature field from the thermal solver. This algorithm implemented in the 3D FDTD simulator QuickWave [51] allows for determining the time evolution of the 3D temperature distribution. Examples of simulations of the heating processes are reported in [52–55].

Table 3.1: Table of temperature dependent material properties used for mulitphysics simulations [11–14]

Temp. [$^\circ C$]	ϵ_r	σ [$\frac{\text{mS}}{\text{m}}$]	c [$\frac{\text{kJ}}{\text{Kkg}}$]	ρ [$\frac{\text{kg}}{\text{m}^3}$]	κ [$\frac{\text{W}}{\text{Km}}$]
Paper Loading					
25	2.2	24.0	1.336	100	0.049
45	2.3	25.1	1.336	100	0.051
70	2.4	32.6	1.336	100	0.053
90	2.6	31.8	1.336	100	0.055
Bread Loading					
25	3.1	50	2.6	200	0.1
40	3.2	55	2.6	200	0.15
55	3.3	70	2.6	200	0.2
70	3.5	80	2.6	200	0.25
85	4.1	105	2.6	200	0.3
Meat Loading					
15	55	2315	3.5	1060	0.41
25	54.5	2246	3.5	1060	0.43
35	54	2466	3.5	1060	0.488
45	53	2287	3.5	1060	0.5
55	51	2328	3.5	1060	0.6
65	51	2519	3.5	1060	0.7

It is difficult to measure the dielectric changes of the waste materials over temperature. Methods to characterize low loss dielectrics such as transmission line based noninvasive methods, and resonant cavity measurements are inaccurate due to the high loss of materials of interest [56, 57]. Partially loaded resonator methods typically have difficulty with determining the temperature of the material during test, however work in this area is being done with systems that can measure a variety of materials over a wide range of temperatures [50,58].

3.3.2 Multiphysics Simulation Results

Including the time evolution of the temperature profile the multi-physics simulations are performed for all three loadings, and are here shown for the case of bread in Fig. 3.8. Note that although the distribution looks similar to that of the volume power density, the thermal conductivity makes the distribution more uniform, which is most easily seen in the center of the cavity.

To quantify the spatial temperature increase, we define heating efficacy, e_{H}, as the mean change in temperature over the volume and over the heating time Δt, normalized to the delivered power:

$$e_{\mathrm{H}} = \frac{\mu_{\mathrm{T}}}{\Delta t \cdot P_{\mathrm{DEL}}}, \tag{3.6}$$

where μ_{T} is the mean of the temperature distribution and P_{DEL} is the power delivered to the cavity which takes into account any reflections as the loading changes. Another relevant metric is the one for uniformity of microwave heating throughout the volume. Here we adopt a definition for uniformity, λ_p, of dissipated power from [59]:

$$\lambda_p = \frac{\sigma_{\mathrm{T}}}{\mu_{\mathrm{T}}}, \tag{3.7}$$

where σ_{T} is the standard deviation of the temperature distribution in the entire volume.

To quantify the uniformity of heating, the heating efficacy (e_{H}) and power uniformity metric (λ_{P}) are calculated from coupled EM and thermal simulations for the three uniform loadings and are presented in Table 3.2. The efficacy does not change significantly for different excitations for the meat and bread loadings, but improves for the paper, while the uniformity improves for the meat and is phase-controlable for the bread loading.

Table 3.2: Summary of single and two probe results

Test	Time(s)	e_{H}	λ_p
Paper Loading			
Circuit Combined	3	.124	.0475
Spatial Combined 0° phase	3	.1465	.2013
Spatial Combined 90° phase	3	.1419	.1555
Spatial Combined 180° phase	3	.138	.1256
Bread Loading			
Circuit Combined	78	.0056	.1717
Spatial Combined 0° phase	80	.0053	.1042
Spatial Combined 90° phase	80	.0053	.1484
Spatial Combined 180° phase	78	.0056	.2040
Meat Loading			
Circuit Combined	80	.0067	.0811
Spatial Combined 0° phase	100	.0001	.0176
Spatial Combined 90° phase	100	.0001	.0177
Spatial Combined 180° phase	100	.0001	.0179

3.3.3 Conclusions

In summary, some conclusions can be made as a result of the analysis presented in this chapter.

- Eigenmode simulations are important for designing the cavity dimensions with the goal of understanding the modes that will combine to determine the uniformity.
- Driven FEM simulations are suited for the initial design of the probes, probe location, and relative phasing.
- Multiphysics simulations give results of the temperature and the dielectric properties over time and should be used at the later steps of a design for evaluating the system performance and comparing with measurements.
- The driven and multiphysics results for the two-port system show the field control and improved uniformity achieved by controlling relative phase. This shows that for systems with unknown/variable loadings the ability to change the relative phase available through the use of SSPAs is more beneficial than increasing the power at a single port (like with a magnetron).

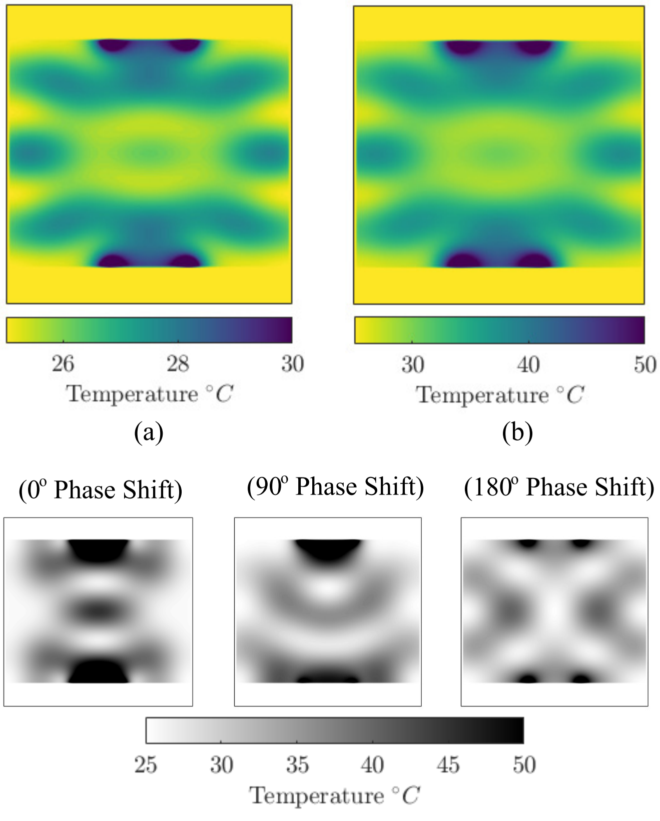

(a)

(b)

(c)

Figure 3.7: Simulated temperature distribution throughout the uniform bread loading at (a) the beginning of the heating process (after 25 s) with a maximum temperature of 25.2° C, and (b) at after 100 s with a maximum temperature of 44.7° C. (c) Simulated temperature distribution in paper loading at the beginning of the heating process (3 s) for 0°, 90° and 180° relative phasing between the probes. The delivered power for both cases is 35 W at each feed.

- The final simulation results show that the efficacy, η_H, does not change significantly between the single-port and two-port cases. However, the uniformity (quantified by the metric λ_p) changes with phase control between two excitation ports.

- The simulation results also hint at the trade-off between uniformity and heating rate. The better uniformity, lowest λ_p, occurs with the slowest heating, lowest η_H, for all three loadings. This comes from the inherent uneven heating.

To validate the conclusions from these simulations three test setups are used, and in each the loading is varied between the three loadings from the simulations, as follows:

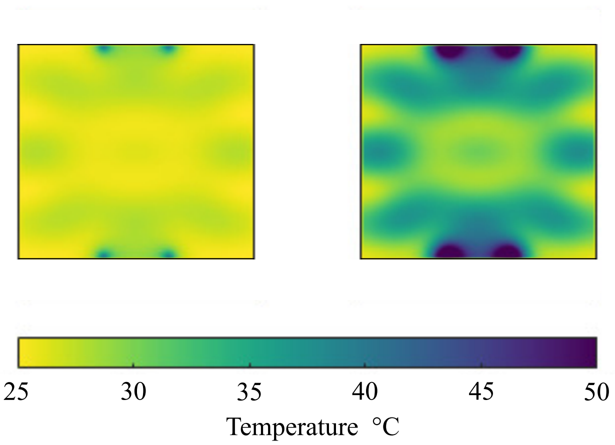

Figure 3.8: Simulated temperature distribution throughout the uniform bread loading at (a) the beginning of the heating process (after 20 s) with a maximum temperature of 25.2° C, and (b) at after 100 s with a maximum temperature of 44.7° C.

(1) a single port driven with a 70 W amplifier;

(2) a single port driven with two circuit combined 70 W amplifiers; and

(3) two ports each driven with a 70 W amplifier with relative phase control.

Test setup 2 can be directly compared to the single-port simulations from this chapter. Tests 1 & 2 can be compared to evaluate the impact of power scaling on heating rate and get an idea of the trade off between heating rate and uniformity. Tests 2 & 3 are compared to see if two ports improve uniformity over a single port in measurements as we see in simulations. Test set up 2 also allows for the investigation of relative phase on spatial heating as compared to simulation.

The material from this chapter is reported partially in [60] describing the field and heating simulations along with corresponding measurements.

CHAPTER 4

MICROWAVE CAVITY HEATING EXPERIMENTS

4.1 INTRODUCTION

In the previous chapters, a discussion of the desired goals for heating efficacy and uniformity along with simulations of a personal trashcan, 1.4 L, cavity are presented. The next interesting question is to validate if using two probes with relative phase control improves the heating uniformity as predicted in simulation. Nine experiments are performed with uniform material loading in the cavity (with paper, bread, and meat) and three experimental setups (single-probe 35 W, single-probe 70 W, and two 35 W probes). These measurements are the expanded to more realistic use cases e.g. accounting for probe mismatch and extending to mixed material loadings.

4.2 HEATING EXPERIMENT SETUP

The simulations from the previous section show steady-state electric field and Joule losses for uniformly-filled cavities with a single or dual feed. When the power is turned on, heating will occur starting from these initial conditions. Due to thermal conduction and changes of material electrical and thermal properties with temperature, the electric field distribution will vary in time as heating continues. We next describe the experimental setup used to measure the temperature distribution over time. This enables a comparison of measured and simulated temperature evolution over time.

Figure 4.1 shows the geometry of a small solid-state driven cavity used to measure the temperature change over time for different loadings. The cavity is cylindrical with a diameter $d = 12.5\,\mathrm{cm}$ and $h = 11.2\,\mathrm{cm}$ in height, made of tin-plated steel. This 1.4 L "waste basket" models an appliance for personal use. The temperature is monitored with 7 type-K thermocouples placed at locations shown in Fig. 4.1 with thermocouple positions given in Table 4.2. The thermocouple positions are chosen to cover the volume somewhat symmetrically and detect the predicted hot and cold spots of the heating under different electrical feeding conditions. The temperature is recorded using a Picolog6 module [61]. The cavity is surrounded by thermal insulation consisting of 2.75 cm thick R5 foam, measuring 40 cm × 32 cm × 40 cm, with a reflective sheet on the internal surface. Solid-state GaN power amplifiers (PAs) are connected with coaxial-to-waveguide adaptors to the WR-340 (2.2–3.3 GHz) waveguide feeds.

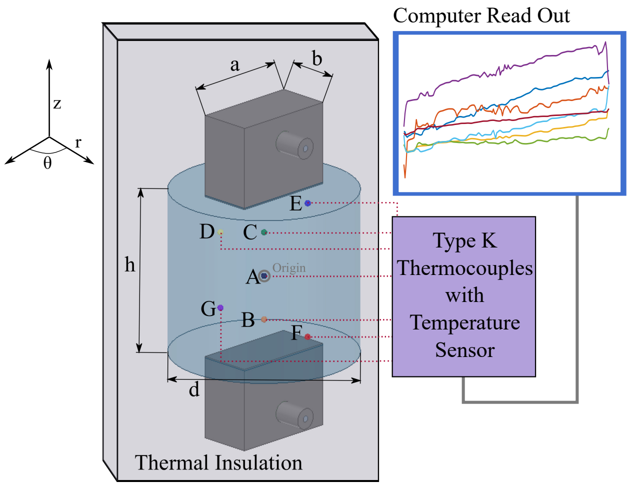

Figure 4.1: Geometry of the S-band waveguide probes and loaded cavity, with $d = 12.5\,\mathrm{cm}$, $h = 11.2\,\mathrm{cm}$, $a = 7.2\,\mathrm{cm}$ and $b = 3.6\,\mathrm{cm}$. Two probes and placed on the bases of the cylinder. If only one probe is used (top probe in Fig. 4.2), the other is shorted with a metal sheet. In the experiments, seven small temperature sensors (not to scale here) are placed throughout the cavity at 7 fixed positions for all experiments.

Two setups are used to investigate heating, shows in Fig.4.2. The first is a single-feed set of experiments with either one PA or two PAs connected to the top waveguide feed (Fig. 4.2a). The two PAs can be combined with a 0.67-dB loss coupler to approximately double the input power. For different cavity loadings, the impedance at the feed will be different, and the reflected power is dissipated in a set of attenuators with 50 dB loss before input to a power meter used to measure the reflected power. A tuner is added in some of

Table 4.1: Table of thermocouple locations referenced to the center of the cavity.

Thermocouple	r (cm)	$\phi(^\circ)$	z (cm)
A	0	N/A	0
B	0	N/A	-3.5
C	0	N/A	3.5
D	4	0	4
E	4	180	4
F	4	90	-4
G	4	270	-4

the measurement to show a path for improving overall efficiency over time. Additional couplers and power meter are used to monitor the output of the PAs. A power divider at the PA inputs is followed by a phase shifter in one of the branches to provide relative phase shift between the PA outputs. The phase shift is set to $\Phi = 0^\circ$ when a single waveguide feed is used as the cavity excitation.

Fig. 4.2b shows the setup for a dual cavity excitation where the relative phase shift Φ can vary. In this case, the output power of the two PAs is spatially combined in the waste loading. Otherwise, the setup is similar to the single-feed case. This setup allows an investigation of spatial power combining and a comparison to cases described in Fig. 4.2a. The power delivered to the cavity is controlled through driver amplifiers in each path (not shown in the figures). A photograph of the bench setup corresponding to the single and two probe set ups is shown in Fig. 4.3.

4.2.1 Probe Mismatch Discussion

The VSWR at the waveguide feed is measured for the three uniform loadings and is well matched for bread (VSWR<2), but is poorly matched to the paper and meat (hotdog) loading (VSWR>5). For appropriate comparison, we keep the power delivered to the cavity constant, with input power equal to $P_{\text{IN}} = P_{\text{DEL}}/(1 - |S_{11}|^2)$. Taking this into account for the measurements the delivered power is kept the same between the materials and single and multiple probe experiments. Additionally there are two methods to reduce the probe mismatch that are looked at here. The first is through a tuner placed between the amplifier and the probe, the second method utilizes the coupling between the two probes to vary the reflection at the probes by varying the relative phase.

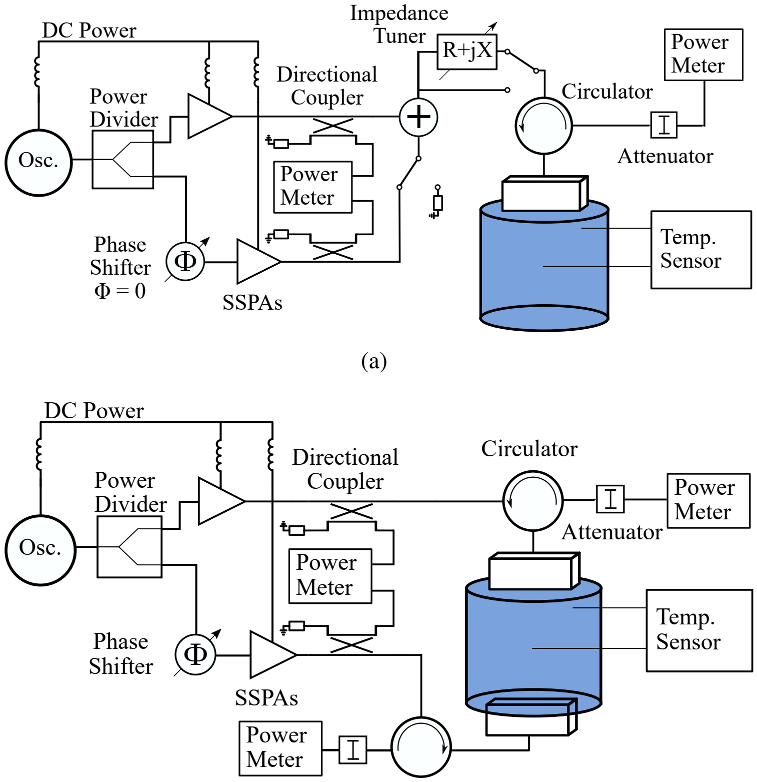

(a)

(b)

Figure 4.2: Two schematics of microwave reactors fed by solid-state power amplifiers (SSPAs) showing the different configurations compared in this investigation. Input power is measured through directional couplers positioned after the SSPAs. (a) One or two SSPAs power combine in phase and the combined power is fed through a single waveguide probe to the cavity. There is an option to feed the waveguide through a circulator to measure reflected power or through a load tuner to form a better match. (b) Two SSPAs are spatially combined in the cavity loaded with waste. The phase shift Φ is adjusted for improved heating uniformity.

The tuner is a mechanical single-slug tuner, consisting of an air coax with an adjustable parallel capacitance to ground. Table 4.2 shows the measured VSWR at the tuner input after adjusting the slug for best match for the three uniform loadings, compared to the impedance match without the tuner.

Table 4.2: Table of single port measured VSWR

Material	Without Tuner	With Tuner
Paper	16	1.012
Bread	2.4	1.29
Meat	5.1	1.32

When the probes couple through the cavity (case ***C***), the probe impedance changes, affecting power delivered to the load. Fig. 4.4 shows the impedance variation for three spatial relative orientations of the two

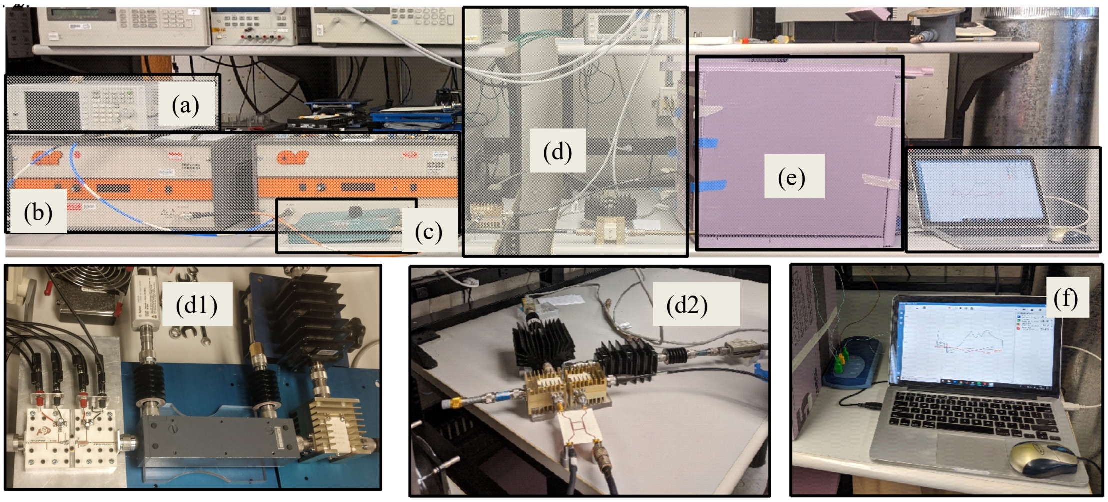

Figure 4.3: Photograph of the test bench set up for single and two feed heating experiments with: (a) signal generator with power splitter; (b) two commercial driver amplifiers; (c) mechanical analog phase shifter; (d1) one amplifier with coupler and circulator for input and reflected power measurements; (d2) circuit power combiner (50 dB attenuators on isolated and reflected ports); (e) insulation surrounding the cavity, and (f) thermocouple temperature sensor and data recording.

probes, while the relative phase is swept from 0° to 360°. This affects the PA efficiency and output power. For example, for the paper loading at 45° orientation, the PAE can improve from 10 to 45% while the output power can increase from 38 to 43 dBm depending on the relative phase. This can be explained with load modulation of power-combined PAs, and the mismatch can be adjusted with tuners or combiner and probe design.

For the case of bread loading, the VSWR remains between 2.4 and 3 for all values of relative phase angle $\Phi = (0°, 360°)$ and for spatial rotations between the probes of $\theta = 0°, 45°$ and 90°. The mismatch for the meat loading is high, with a VSWR=5, independent of phase shift or orientation, due the high absorption of meat that prevents coupling. For the case of paper loading, the coupling between the probes is high and changing the relative phase and/or orientation has a dramatic effect on the impedance match, with a minimum VSWR=2.5 at ($\Phi = 260°, \theta = 45°$) while the maximum VSWR exceeds 10.

When the two feeds are rotated with respect to each other, thus changing the mode content in the cavity, the heating efficacy remains practically constant for 0° and 45° relative spatial orientation ($e_{\mathrm{H}} = 0.0017$ and $e_{\mathrm{H}} = 0.0016$ for 1 s heating of paper). However, the uniformity improves with rotation from $\lambda_p = 2.38$ to $\lambda_p = 1.93$. For the bread loading, a similar trend is observed, while in the case of meat loading, the coupling

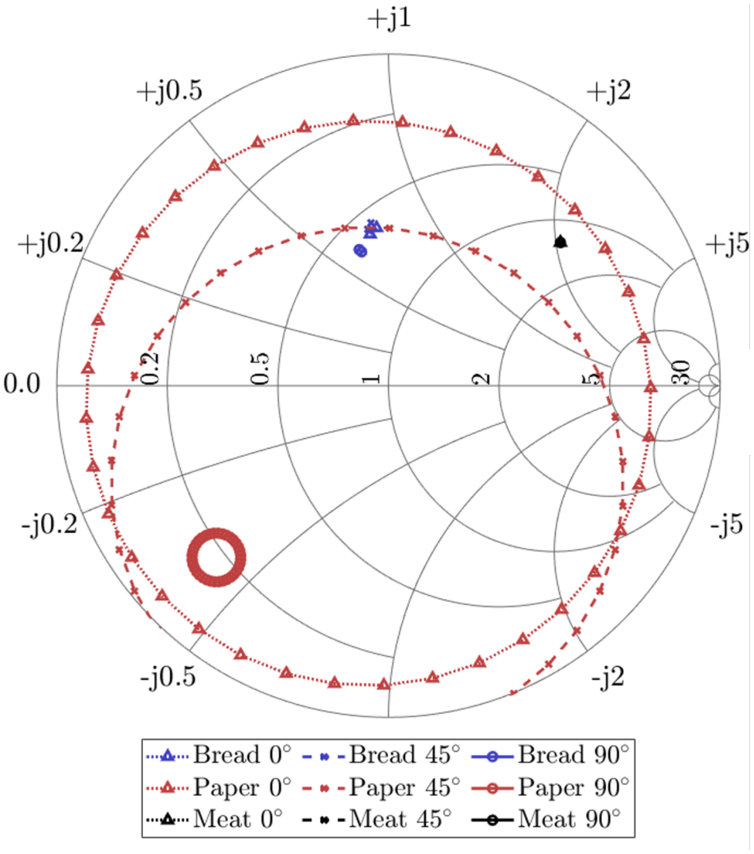

Figure 4.4: Measured input impedance with the relative phase of the second port swept for the empty/air, paper, bread and meat (hotdog) filled cavity at 2.45 GHz, with a phase varying from 0° to 360°.

is negligible due to high absorption.

Another complication of the cross coupling effects on the system is that the optimal relative phasing for one port doesn't align with the best match for the other port. This is visualized by Fig. 4.5 the relative phasing between the ports is based on measured s-parameters of the cavity and is not calibrated to the some plane as the heating measurements and simulations.

It was also found that with the meat loading the thermal properties change as the materials heat up and the return loss improves drastically, from 5 to 25 dB (in this case, for 120 W applied power) and 5 to 10 dB (for 60 W applied power) over a 40 minute test. This supports the previously made claim that modeling the electrical parameters as a function of temperature is needed to improve performance over time with impedance tuning.

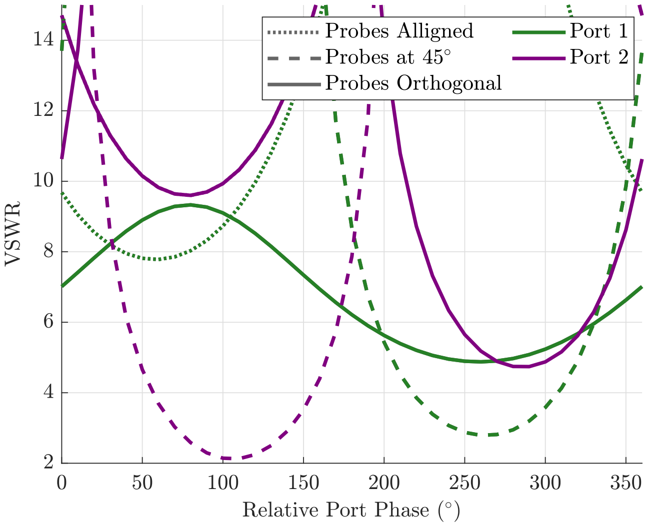

Figure 4.5: VSWR from measured s-parameters with the relative phase of the second port swept for the paper filled cavity at 2.45 GHz, with a phase varying from 0° to 360°.

4.2.2 Power Amplifier Design

Two single-stage GaN hybrid PAs with Qorvo 70-W QPD1015L packaged devices are designed, starting from load and source-pull simulations at the fundamental and second harmonic. The package capacitance presents a short at the third harmonic, limiting the waveshaping capability. The bias is chosen to be in the AB region as this gives higher output power [62]. The input is matched to a simulated large-signal reflection coefficient at 2.45 GHz, and the output match is designed to maximize output power while maintaining high PAE. The challenge is that for the high power devices at these frequencies the impedance the device wants to see at the output is close to a short, Fig. 4.6.

The bias circuits present opens at the fundamental, and the second harmonic is shorted at the output of the device. The circuit is implemented on a Rogers 4360G 32-mil thick substrate with the device mounted directly on the grounded heat sink, as shown in Fig. 4.7. The measured output power, PAE and gain vs. input power at 2.4 and 2.45 GHz are shown in Fig. 4.8. The output power and efficiency remain above 60 W and 52 % for the 2.3–2.6 GHz (12%) bandwidth, allowing for broadband frequency modulation. The input match of the measured device remains below 15 dB over the 2.3–2.6 GHz bandwidth. Two power amplifiers are fabricated and have repeatable performance.

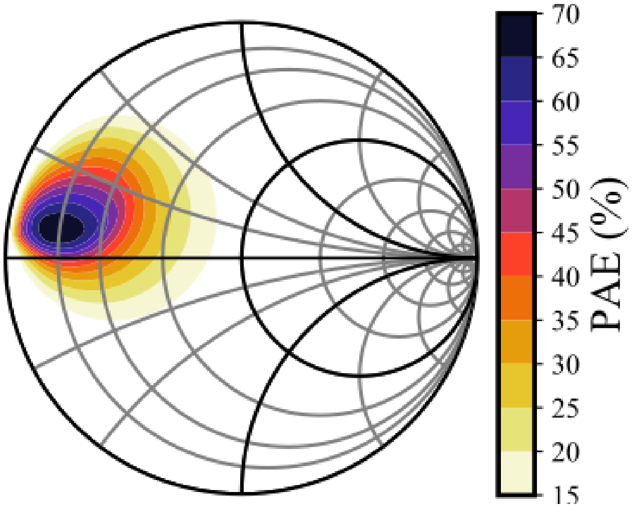

Figure 4.6: Simulated loadpull for the Qorvo 70-W QPD1015L packaged transistor showing the peak PAE occurs for presented impedances close to 5Ω.

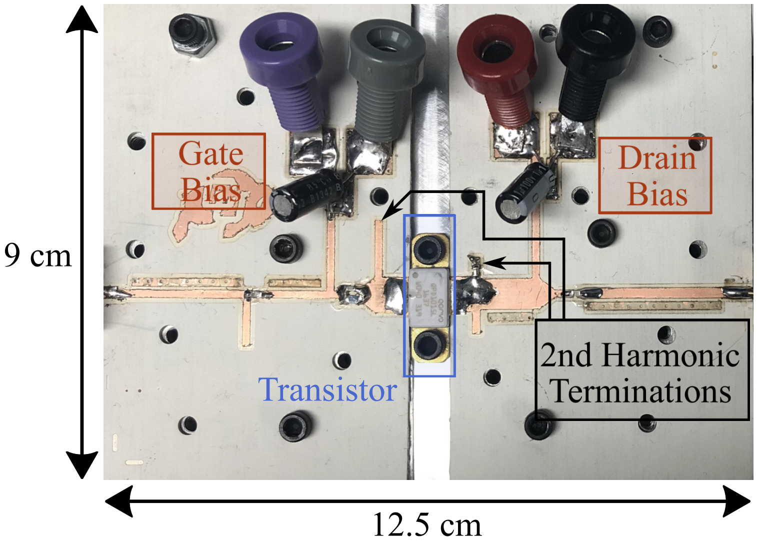

Figure 4.7: Photograph of 70-W peak power GaN hybrid power amplifier showing the second harmonic termination.

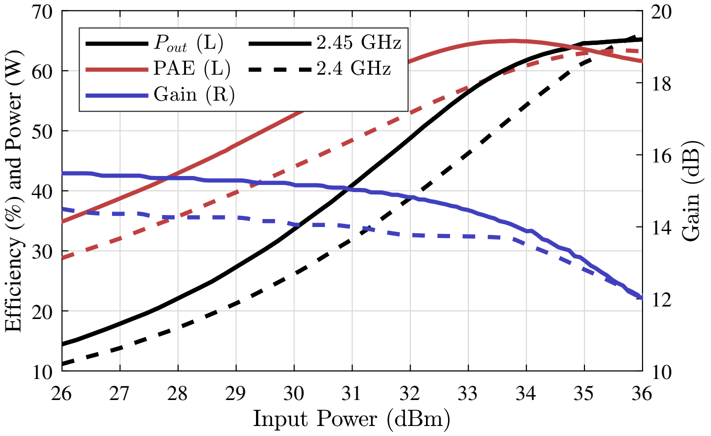

Figure 4.8: Measured PA performance at 2.40 and 2.45 GHz with photograph of one of the two hybrid SSPAs based on a 70-W packaged GaN transistor.

4.2.3 Measurement Overview

The following cases of loading and amplifier configurations are compared experimentally:

A. Single power amplifier (PA) with P_{OUT}=70 W. Since the reflection coefficient varies for different cavity loadings, we correct for this by keeping the delivered power constant at P_{DEL} = 35 W. The delivered power is tuned for the initial temperature and not continuously adjusted during operation. Note that the paper and meat (hotdog) cavity fillings result in a mismatch at the probe with $|\Gamma| \approx 0.5$.

B. Two equal 70 W PAs, externally combined with a power combining efficiency of 85.6%, delivering power to the cavity through a single probe. The changes in the reflection coefficient are compensated and the delivered power is kept constant at P_{DEL} = 70 W.

C. Single probe with two PAs, same as case ***B***, but with an added impedance tuner, Fig. 4.2a. The power is adjusted to a level that allows fair comparison to other cases.

D. Two equal 70 W PAs, each feeding a probe, spatially combined inside the waste volume, where P_{DEL} varies. The applied power is kept the same as in case B, for a fair comparison.

4.3 EXPERIMENTAL RESULTS WITH HOMOGENEOUS WASTE MATERIALS

In this section, measurements with a single and two feeds for uniform paper, bread and meat loading are presented with the setups from Figs.4.1 and 4.2 and compared with multiphysics simulations. Next we describe results from measurements for cases ***A*** and ***B*** with a single probe for all three uniform loadings. The goal is to gain a better understanding of how the loss mechanisms change with increasing power level. Doubling the power should double the heating rate, however the loss mechanisms will differ between the two power levels because the material properties change with temperature.

4.3.1 SINGLE FEED WITH SINGLE PA

Figures 4.9, 4.10, 4.11 show measured temperature time evolutions at the 7 thermocouple positions for the case of a single PA feed with a delivered power of 35 W (case ***A***) on the left. For the paper loading, in 1 minute, the temperature increases up to 10°C, while it takes more than 5 minutes for a comparable increase in temperature for the bread, and around 10 minutes for the meat loading. Although the delivered power is the same in all three cases, the meat takes a considerably longer time to heat up due to its relatively high specific heat and low thermal conductivity. For longer heating times, the slope changes due to material electrical property variations, as can be seen for the bread and meat loading.

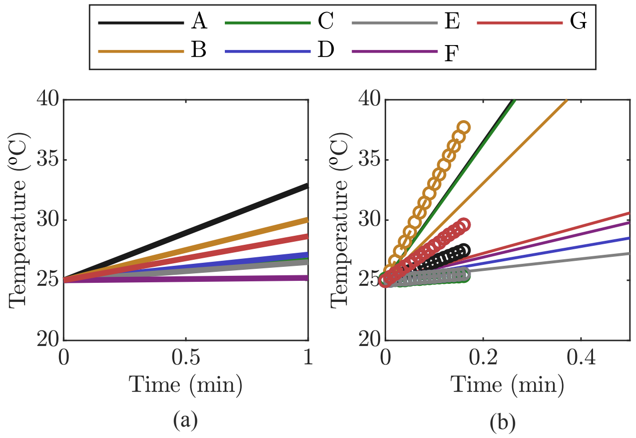

(a) (b)

Figure 4.9: Measured temperature increase at 7 temperature sensor locations (A to G) for paper loading of the cavity with a single feed for 35 W (a) and 70 W (b) of delivered power. The circular symbols show results from multi-physics simulations of heating rates at the thermocouple locations for the 70 W applied power.

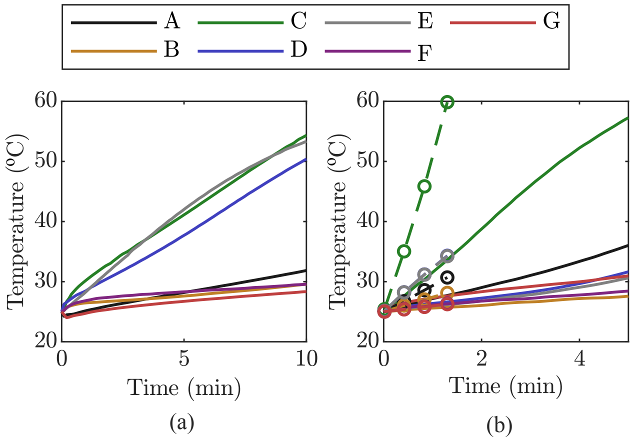

(a) (b)

Figure 4.10: Measured temperature increase at 7 temperature sensor locations (A to G) for bread loading of the cavity with a single feed for 35 W (a) and 70 W (b) of delivered power. The circular symbols show results from multi-physics simulations of heating rates at the thermocouple locations for the 70 W applied power.

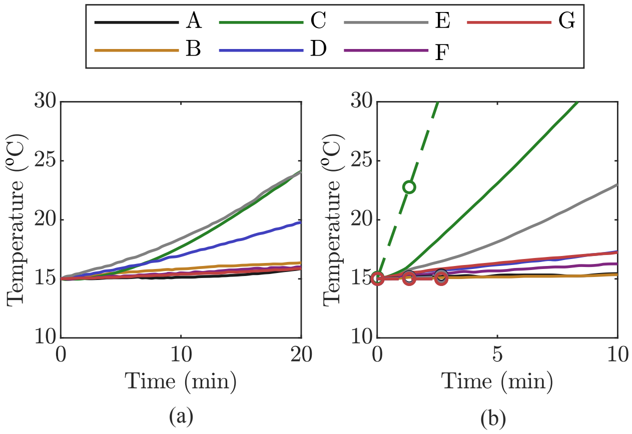

(a) (b)

Figure 4.11: Measured temperature increase at 7 temperature sensor locations (A to G) for meat loading of the cavity with a single feed for 35 W (a) and 70 W (b) of delivered power. The circular symbols show results from multi-physics simulations of heating rates at the thermocouple locations for the 70 W applied power.

4.3.2 Power Scaling with Single Feed

Next, the measurements are repeated with a two-fold increase in delivered power (case ***B***), and the results are shown in Figures 4.9(b), 4.10(b), and 4.11(b). The circuit-combined measurements use a branch-line coupler to combine the 70 W amplifier outputs. The theory (shown with circles) predicts the trends and is most accurate for the bread loading Above 100°C, limited information on food material electrical parameters exists, and therefore multiphysics simulations are performed in the lower temperature range to validate the trends. In all cases, the predicted temperatures are somewhat higher. The discrepancies are expected due to the following practical reasons: i) the material properties from the literature are validated with a simple and approximate loaded waveguide measurement [63]; ii) the multiphysics theory does not take into account the thermal losses (e.g. waveguide probe heating) that exist in the measurement.

The temperature measurements for the paper loading are sensitive to thermocouple placement around hot spots since the heating distribution is much more uneven due to the high electric fields and low thermal conductivity. This sensitivity is reflected in the disagreement with simulations. In the case of meat loading, the measurements indicate that the thermal and electrical conductivities are different from the simulated ones. There is a tradeoff between the heating rate and uniformity described by the spread of temperatures across different thermocouples. When the power doubles, the heating rate does not double at every location. Instead, the temperature rates diverge and the hotter spots heat faster than the cold ones. The paper measurements appear linear because the thermocouples are inaccurate during the microwave heating experiments due to the high electric fields incident on the sensors. Therefore, the temperature measurements immediately before and after the electric field is applied are used to show the heating rate. This is not completely representative of the heating during operation, but shows the trends at different locations in the cavity.

Past 100°C, limited information on food material electrical parameters exists, and therefore multiphysics simulations are performed in the lower temperature range to validate the trends, shown with symbols in Figures 7 through 9. The trends are predicted, as well as the order of magnitude. The discrepancies are expected due to the following practical reasons: a) the material properties from the literature are validated with a simple and approximate loaded waveguide measurement [63]; b) the simulations are done for uniform materials, which is difficult to achieve in measurements; and c) the temperature probes measure an average over a small volume, while the simulations are performed at discrete points.

4.3.3 Single Feed with Impedance Tuner

Configuration **C** with a tuner to improve the delivered power is compared to the initial setup in Configuration **A**. The tuner improvement in the match is discussed in section 4.2.1. Fig. 4.12 plots the measured temperature increase over time for thermocouple C, near the excitation probe at the top of the cavity, for heating with and without the tuner. The tuner is set manually to minimize the reflection at the probe for the three uniform loadings, showing increased heating for the matched case compared to case without the tuner. It is interesting to note that the relative increase in heating differs between materials, since their electrical properties change differently with temperature.

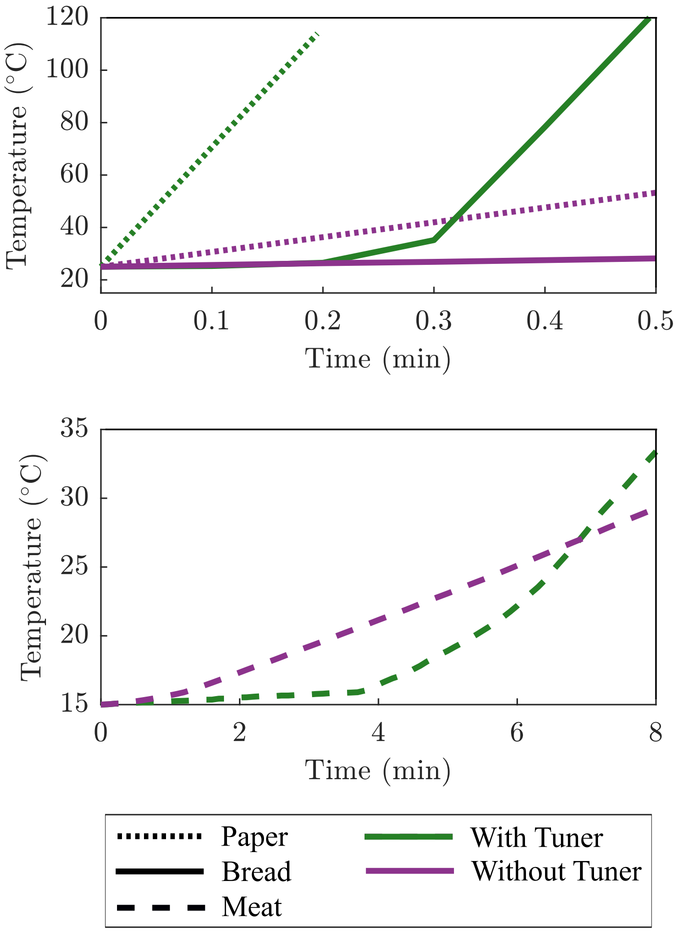

Figure 4.12: Measured temperature increase by temperature sensor **C** from Fig. 4.1, with and without a single tuner-matched feed for paper (dotted), bread (solid), and meat (dashed) loadings.

4.3.4 SPATIAL POWER COMBINING IN WASTE VOLUME

For the spatially combined method (case ***D***), two 70 W amplifiers supply power to the two feed probes with circulators, depicted in Fig. 4.2b. A phase shifter varies the relative phase between the two PAs between

Φ = 0° and Φ = 180° in 45° steps. The thermocouple temperature sensor placement, data recording, and thermal insulation is the same as in the circuit-combined measurements.

Experimental validation for the trends shown in Table 3.2 was performed for bread loading. Fig. 4.13 shows heating results for 0° (left) and 180° (right) relative phase difference between the two feeds. Measurements of heating rates at different points in the waste loading shows that the heating uniformity depends on relative phase between the two feeds. Additionally, controlling relative phase affects the electric field and therefore the heating distribution, shown at thermocouple A for several relative phase, Φ, settings in Fig. 4.15. The most important conclusions from this data are: (1) the heating uniformity can be improved by phasing between the two feeds; (2) for the high-conductivity meat loading the uniformity improves greatly with spatial power combining but not with relative phasing; and (3) the saturation in the temperature increases for the bread loading near 100°C indicating that the temperature dependence of the material properties affects heating for longer microwave powers or higher temperatures.

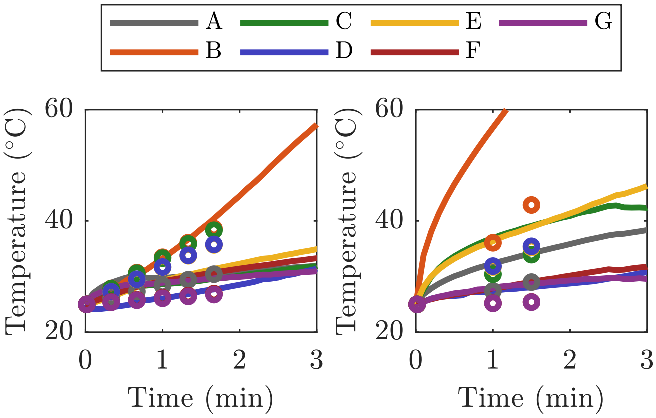

Figure 4.13: Measured temperature increase at 7 temperature sensor locations (A to G) for bread loading of the cavity with two feeds for 0° (left) and 180° (right) relative phase shift between the two probes. The symbols, *′o′*, show results from multi-physics simulations of heating rates at the thermocouple locations for the 70 W applied power.

Another important result obtained from the multiphysics simulations is shown in Fig.3.8, where the temperature distribution after 3 seconds is found for three relative phases (0°, 90° and 180°) and 35 W delivered power to each waveguide probe. (Note that in this case, the delivered power is difficult to measure.) These simulated results also show, in agreement with measurements, that phase shift can be used to control the heating patterns inside a loaded cavity.

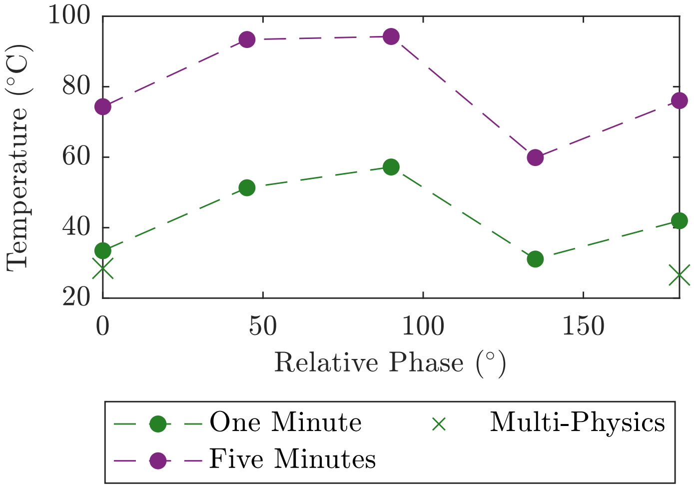

Figure 4.14: Readings at temperature sensor A after one minute and after five minutes of heating in two-port configuration. Measured temperature is plotted versus relative phase between ports. Multi-physics simulations done up to one minute are marked by X's.

Experimental validation for the trends shown in Table 3.2 was performed at points A and B of Fig. 4.1 and the results are shown in Fig. 4.15. The most important conclusions from this data are: (1) for paper and bread, the uniformity can be improved with phasing between the two feeds; and (2) for the high-conductivity meat, although the uniformity does not improve with phasing, it improves greatly with spatial power combining. Additionally, the saturation in the temperature increases for the bread loading near 100°C indicating that the temperature dependence of the material properties affects heating for longer microwave powers or higher temperatures.

When two feeds are used, the probe impedance changes due to near-field coupling. In the experiments above, the two waveguide feeds are aligned. In the next subsection the effect of probe orientation on cross coupling and how it effects the large signal are in investigated.

4.4 Experiments with Mixed Waste Materials

The previous section describes simulated and measured heating of a uniformly-loaded cylindrical cavity, with power delivered from one or two SSPAs which can be driven with a variable relative phase. When mixed waste is introduced in the cavity, the mode distribution changes. To investigate the effects of nonuniform waste materials on heating, measurements are performed for three mixed food waste scenarios:

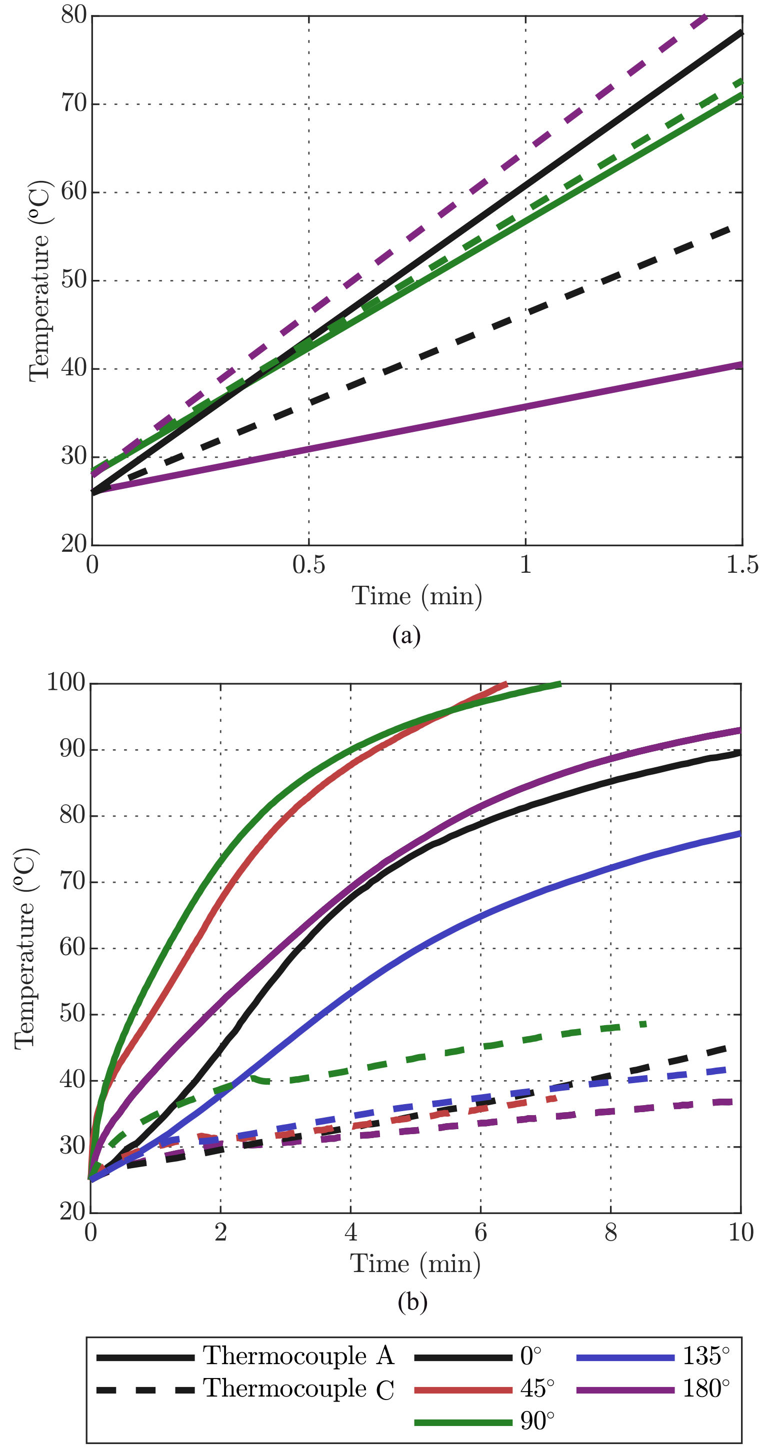

(a)

(b)

Figure 4.15: Measured temperature increase at the center (Thermocouple A) and near the bottom probe (Thermocouple B) for cavity loaded with (a) paper and (b) bread.

1. Three materials (meat, bread, and paper) are layered in the z dimension, Fig.4.16a;

2. Two materials (meat and bread) are layered radially Fig.4.16b; and

3. Various food waste mixtures, low ϵ_r (coffee grinds, paper, oats), medium ϵ_r (coffee grinds, paper, oats, bread), and high ϵ_r (paper, bread, meat), fully filling the cavity, Fig.4.16c.

The first two sets of measurements are performed with 120 W of total applied power (taking reflection into account), with a focus on comparing circuit-combined single-feed and spatially-combined dual-feed heating. Fig. 4.17a shows the results measured by thermocouples A (center) and D (top). These measurements show that the temperature at thermocouple D is heating faster with the circuit power combining and a single-probe feed than with dual-feed spatial combining. However, spatial combining heats the center portion of the waste volume significantly faster, as shown by the more uniform temperature in the center and top of the cavity (dashed lines in Fig. 4.17a. In the experiments, the order of layers is chosen to provide a gradient of dielectric constants from lowest to highest, relative to the probe plane, in order to improve the penetration depth and the return loss. For a different layer structure (e.g. meat near the probe), the penetration depth would be reduced, limiting the advantage of spatial combining in this case. In summary, the spatial combining improves the heating uniformity. This is quantified by an approximately 70°C difference between top and center of the cavity with a single feed, reduced to less than 10°C difference for spatial combining after 5 min of heating with a total power of 120 W.

In the radially-distributed layers from Fig.4.16b, a thin Styrofoam separator surrounds the meat to prevent heat transfer between the two layers. Fig.4.17b illustrates the importance of the temperature dependence of material properties. The center of the volume (thermocouple A) is heated with a delay for the circuit-combined compared to spatially-combined case, which indicates that the material properties are changing with temperature. The water content decreases with temperature, which increases penetration depth, resulting in a field distribution that changes faster for the circuit-combined measurement. It is also interesting that the temperature measured by thermocouple D flattens around 60° for the spatially-combined feeds. This saturation is likely caused by the power being concentrated away from the top of the cavity where thermocouple D is placed. For the radially non-uniform waste mixture, again the spatial combining results in better uniformity of about 10°C vs. 30°C difference between top and center of cavity after 15 min of heating with a total power of 120 W.

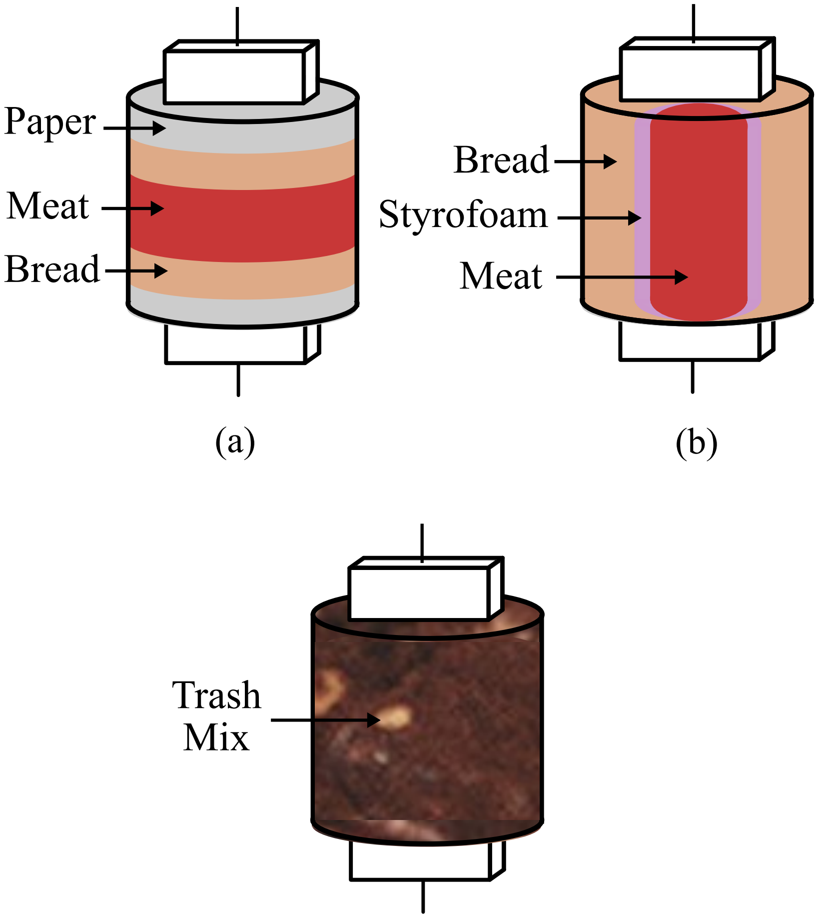

(a) (b)

(c)

Figure 4.16: Geometry of experiments with multiple waste loading of the 1.4 L cavity. (a) Vertical layering, with 19 mm of paper, 19 mm of bread, 36 mm of meat, 19 mm of bread, and 19 mm of paper, from top to bottom. (b) Radial layering with 3.2 mm of meat surrounded by 3 mm of bread loading. The meat and bread are separated with a thin Styrofoam ($\epsilon_r \approx 1$) wall. (c) Blended food waste mixture.

In the final case of mixed food waste, the cavity was filled with low, medium, and high permittivity mixtures. Two sets of measurements are presented: one with a single feed with an impedance tuner, and the other with two feeds and phase adjustment for best match. Due to the low permittivity and conductivity of the loading, the two feed probes couple and it is difficult to impedance match both simultaneously with a relative phase offset. The results of the measurements are shown in Fig. 4.18 for the two cases. Similar to the cases presented in Fig.4.17, spatial power combining demonstrates better heating uniformity compared with a single-port excitation. The exception is the low-permittivity mixture case, expected due to the stronger coupling between feed ports.

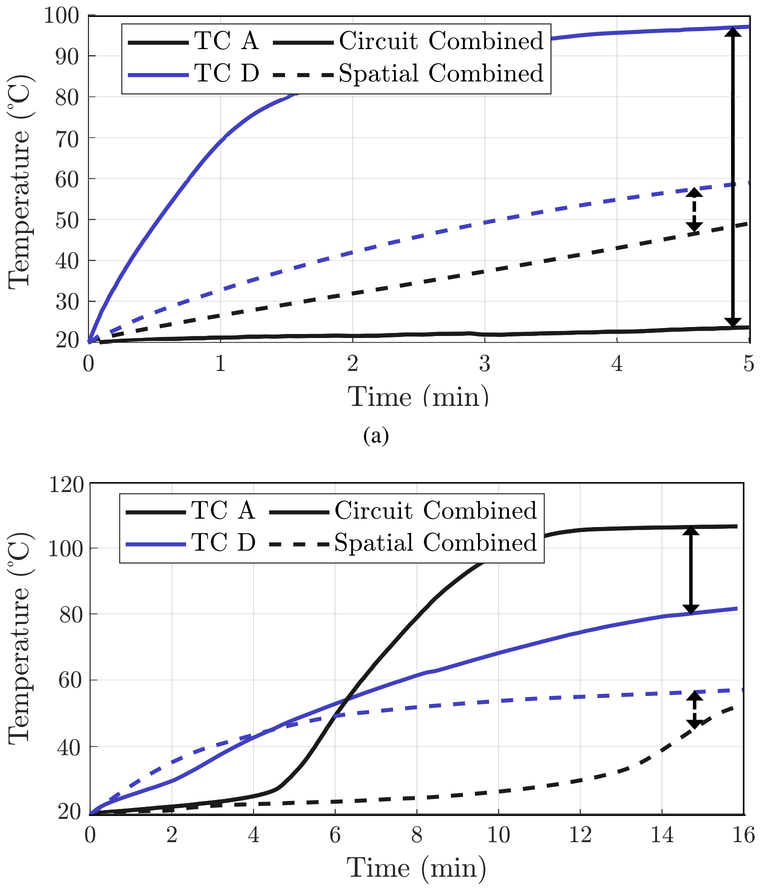

(a)

(b)

Figure 4.17: Measured temperature variation at thermocouples A and D of equal volumes of paper, bread, and meat loadings, layered vertically as described in Fig. 4.16a (a) and radially as described in Fig. 4.16b (b), with 120 W applied power to a single port by circuit-level combining of two PAs, and for the case when two probes are powered with 60 W applied power in each feed. The vertical arrows again show that the spatial combining provides significantly more uniform heating in this case.

4.5 Conclusions

In summary, this chapter presents an experimental investigation of a microwave heating cavity for waste pyrolitic breakdown, using circuit-level and spatial solid-state GaN power amplifier combining in the 2.45 GHz ISM band. The experiments are performed in a 1.4 L cavity by combining two 70 W PAs with PAE>60%, and the temperature is measured in 7 discrete locations throughout the volume using small thermocouples which minimally interact with the measurement. Some interesting conclusions are as follows.

- The experimental and theoretical results show that spatial combining within the waste volume has

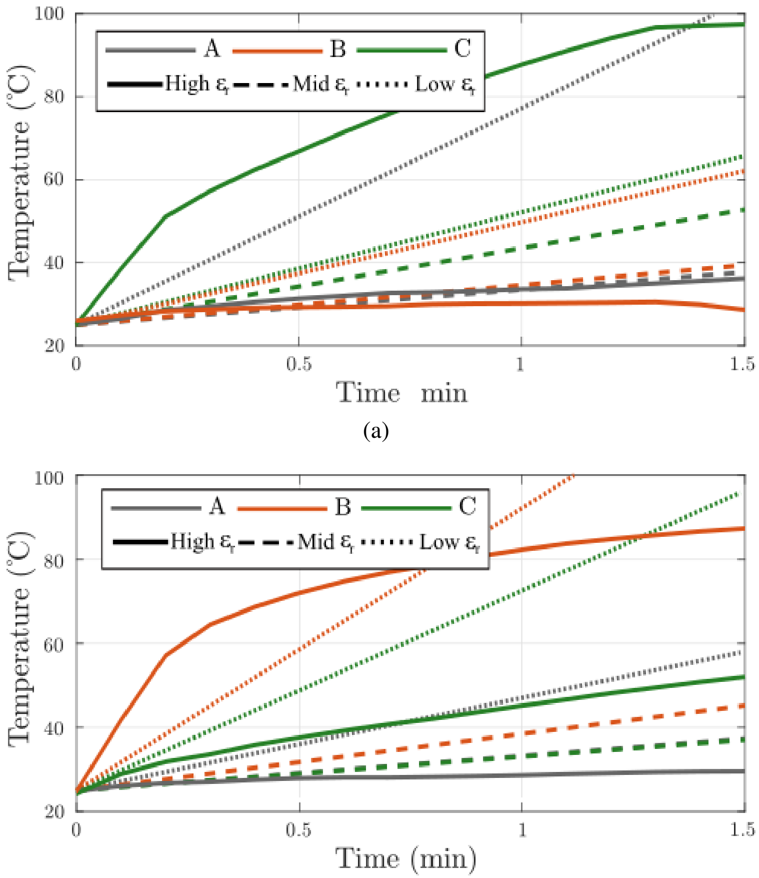

(a)

(b)

Figure 4.18: Measured temperature variation at thermocouples A, B, and C of equal volumes of a low, medium, and high dielectric constant mixed waste loadings. (a) Measurements with the impedance tuner at the single port for a delivered power of 129 W for each loading. (b) Measurement with two probes with relative phase adjusted to improve the match at the ports, with a delivered power of 90 W for the low and high permittivity mixed waste loadings and 100 W for the medium permittivity mixed waste. The total applied power is the same for (a) and (b).

advantages in terms of efficacy, especially when uniform waste heating is desired.

- Controlling the relative phase between two (or more) power sources allows improved heating, which can improve heating when material properties vary with temperature.
- Simulations using FEM modeling of the cavity predict the modal content and Joule volume losses, while multi-physics FDTD modeling with temperature-dependent material properties are able to predict the volumetric temperature distribution and its evolution in time. The limitations in material properties make the FDTD simulations good for showing trends, but ultimately unaligned with the

measurements.

- Varying material properties change the matching conditions and coupling between the SSPAs, indicating that some tuning mechanism would be beneficial.
- Wideband frequency modulation enabled by solid-state sources shows increased heating uniformity.
- Experiments with mixed waste materials show more uniform heating with volumetric power combining.

In the experiments presented throughout this chapter, after 40 minutes of heating with 120 W of applied microwave power, the reactor reduced mixed meat product to coke (coal). Since the reflection coefficient changes as the waste is heated, the energy efficiency calculation is not straightforward, and using the applied energy of 288 kJ gives the worst-case energy recovery ratio. Assuming coal has a calorific value of 30 MJ/kg, with 0.2 kg of resulting coal, 20 MJ is recovered for each MJ of microwave energy. The system efficiency is of course below unity, since the initial waste has energy content and the microwave generation is at most 70% efficient. The results shown in this chapter suggest that solid-state amplifier combining can be efficiently used for waste material pyrolysis. Although demonstrated on a small 1.4 L cavity with modest 70-W PAs, the approach is scalable to larger volumes, power levels, as well as number of feeds. For larger volumes, a lower frequency (915 MHz) would be desirable due to the available high-power transistors and increased penetration depth in most materials of interest. The material from this chapter is reported in [60, 64, 65].

CHAPTER 5

PART I SUMMARY AND FUTURE WORK

5.1 INTRODUCTION

The previous chapters show a demonstration of efficient uniform and mixed waste heating using solid-state power combining. Some topics for future work are described in this chapter, with initial results that show possible improvements or paths to system scaling. For improved field uniformity, two methods are investigate, one by modifying the excitation, and the other by modifying the cavity. For the former, frequency modulation of the power amplifiers is investigated experimentally, and for the latter some simulations are performed with altered cavity wall boundary conditions.

5.2 VOLUME SCALING

A small-volume personal size trashcan of 1.4 L is a viable demonstration, however larger volumes are required for other applications. The approach with multiple solid-stage amplifiers lends itself to scaling by not only scaling the power of an individual PA, but also the number of PAs. For example, by scaling the cavity volume to 5.2 L, Fig.5.1, the simulated field profile shows that the power needs to be increased. Fig.5.2 shows a comparison of Joule loss density in the two cavities for an applied power scaled by a factor of 3.7, which is the volume ratio. Notice that for uniform bread loading, and the same type of waveguide feed, the field profile is different since different modes are excited, pointing to the need for modal content control discussed in the next section. Without the power scaling of the input power the joule loss density seen in (b) is substantially lower than the smaller cavity with the same power (a) and the larger cavity with the scaled input power (c).

Scaling from 70 W to 260 W with a GaN solid-state device is realistic, for example commercial devices and amplifiers exist up to 500 W in CW operation the 2-GHz frequency range from different manufacturers, e.g. [66, 67]. For pulsed mode of operation, the powers are higher and reach 1.4 kW at 1 GHz, shown in e.g. [68–70]. These high power pulsed devices have PAEs ranging from 55–70%. Additionally, magnetrons exist at these high power levels, but are difficult to power combine or modulate [40].

Figure 5.1: Photograph of the 1.4 L (left) and a scaled 5.2 L (right) cavities made of the tin-plated steal.

5.3 Improving Field Uniformity

Field uniformity control enables better heating efficiency, and this will be more critical for larger volumes. For improving field uniformity, two methods are investigated: (1) relatively broadband frequency modulation of the excitation, which changes the mode distribution; and (2) modifying the boundary conditions of the cavity walls which also affect the available modes and additionally remove the electric field and therefore heating nulls close to the cavity walls.

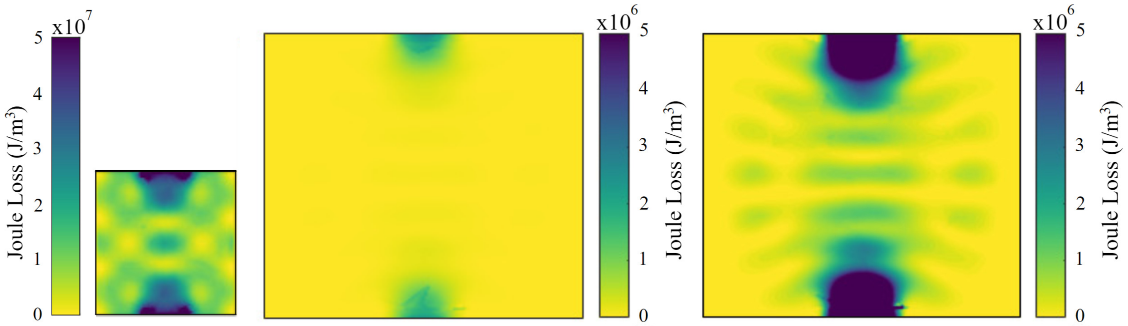

(a) (b) (c)

Figure 5.2: Simulated density of Joule losses through a central cross-section for 1.4 L (a) and 5.2 L (b) cavities with the same two waveguide feeds, with same applied power and (c) 5.2 L cavitie scaled with volume (a factor of 3.7).

5.3.1 Frequency Modulation

One benefit of using solid-state sources over magnetrons is the ability to modulate the frequency. Fig. 5.3 compares the jhoule losses when the paper loaded 1.4 L cavity is driven with a continuous signal compared to and FM modulated signal. The distribution doesn't change greatly since the relative frequency modulation is smal compared to the frequency of operation. However, the joule losses at center of the cavity and near the feed are higher for the FM case and indicate more uniform heating. Fig. 5.4 shows the improvement in uniformity when a frequency-modulated (FM) excitation is used for paper loading, compared to the CW measurements. With 60 W of applied power, and a frequency swept linearly from 2.25 to 2.65 GHz over a 100 msec time period (a 16% modulation bandwidth), the FM measurements show a variation of about 10° after 3 minutes of heating, while the CW measurements show over 15° of variation throughout the volume. The applied power is kept constant which does not take into account the frequency dependent reflection coefficient at the probe for the delivered power. The solid vertical line corresponding to the FM measurements shows the reduced spread of temperatures throughout the volume compared to the temperature variations for CW measurements, shown in dashed line.

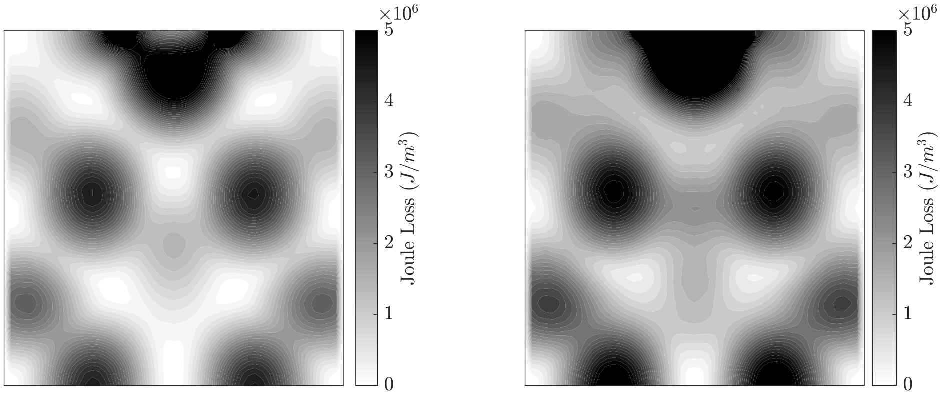

(a)

(b)

Figure 5.3: Simulated (driven modal) time average joule losses for the 1.4 L cavity with 60 W applied power at (a) 2.45 GHz fixed frequency and (b) FM signal swept from 2.25 GHz to 2.65 GHz.

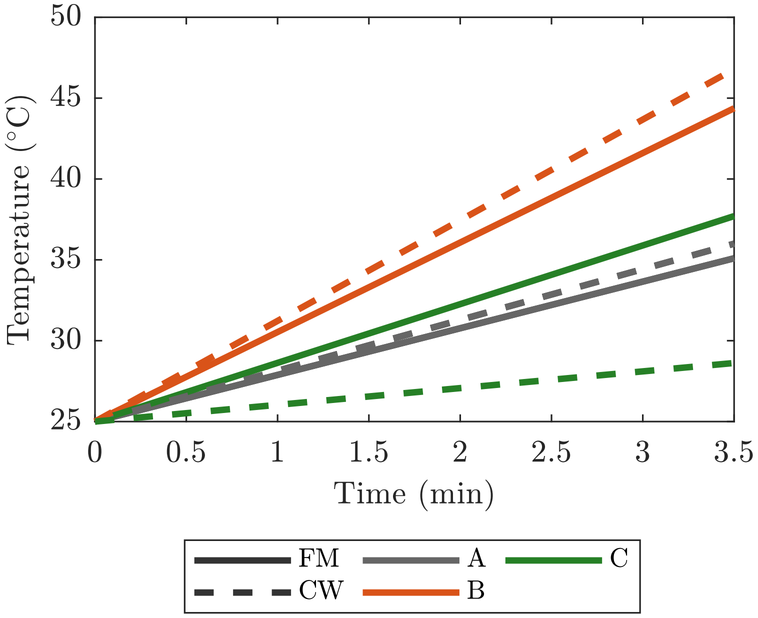

Figure 5.4: Measured temperature increase at the 3 thermocouple locations under a single probe with 60 W of applied power at 2.45 GHz (CW, dashed lines), and FM swept from 2.25 to 2.65 GHz (solid lines).

5.3.2 Modified Cavity Boundary Conditions

When boundary conditions on the walls of a cavity are changed, the solutions of Maxwell's equations also change. For example, in [71] a "metasurface" is is used to increase the number of modes and improve field uniformity in a reverberation chamber at 80–200 MHz. A metasurface here refers to a periodic metal structure printed on a dielectric, with a periodicity that is significantly smaller than the largest free-space wavelength, in contrast to frequency selective surfaces (FSSs) with half-wavelength periodicity. Increasing the number of modes can also be achieved with an electrically large cavity or with mode stirrers that mechanically change the boundary conditions of the cavity to alter the modes. Using a mechanical mode stirrer can add complexity to a cavity design and can be difficult to implement in cavities with large operational load filling.

For a heating application, the larger bandwidth is not needed, and the advantages of modified cavity walls are in narrowband uniformity through superposition of many excited modes, and in increased Joule losses close to the walls. Here the goal is to demonstrate with simulations that placing an unusual boundary condition at the cavity walls increases the modal content of a cavity. Using boundary conditions allows for the cavity to remain physically small with no additional mechanics and have increased field uniformity.

The design of the periodic structure shown in Fig.5.5 is scaled and modified from the 140-MHz design in [71]. A Rogers 3010, ϵ_r 10.2, 50 mil thick substrate is chosen. The angle θ in Fig.5.5 is used as a parameter, and the simulated reflection phase for an infinite flat periodic surface in air and for $\theta = 66°$ and $\theta = 79°$ was performed to determine the boundary conditions of the two structures.

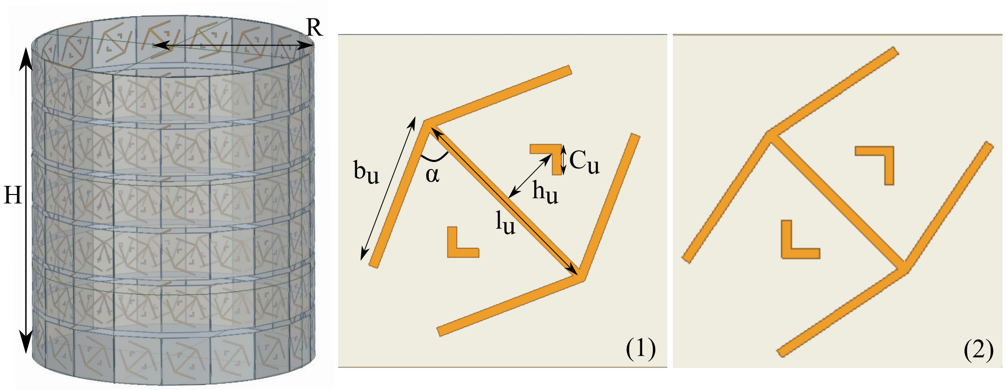

Figure 5.5: Geometry of the simulated cavity with height (H) of 28.3 cm and radius (R) of 12.7 cm. The layouts and geometrical parameters of the FSS unit cells proposed: au= 43 mm, b = 20 mm, cu = 4 mm, hu = 9.5 mm, lu = 28 mm, wu = 1.2 mm, $\alpha = 79°$ for cell 1 and $\alpha = 66°$ for cell 2. The thickness of metallic patterns is 0.035 mm. The Rogers 3010 dielectric substrate with thickness du = 50 mil, dielectric constant $\epsilon_r = 10.2$ and tan$\delta = 0.005$ has been considered.

Placing the periodic surface on the walls of a cavity creates boundary conditions that vary over frequency. The frequency spacing between modes will decrease with the varying electrical dimensions around the desired frequency of operation. To test whether the periodic structure placed on the boundaries increases the modal content of the cavity, HFSS eigenmode are used to find the modes between 2.4 and 2.5 GHz. The solver was run for three cases; namely for PEC boundaries and the two periodic structure designs placed on the curved boundary of the cyllindrical cavity. The dimensions of the cylindrical cavity correspond to the 5.2 L case (ρ= 12.7 cm, and z = 28.3 cm), Fig. 5.5. The improvement in the number of modes for the air filled cavity is shown in Fig. 5.6. The modes of the cavity around 2.45 GHz improves with the FSS boundary conditions compared to the PEC boundary. This improvement should be even greater when the cavity is loaded and the number of modes present in the PEC cavity is higher.

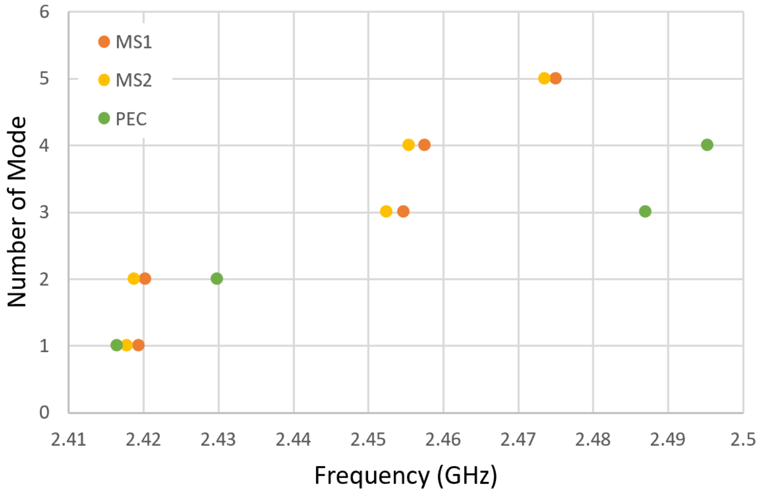

Figure 5.6: Graph of the number of modes in cylindrical cavity between 2.4 GHz and 2.5 GHz.

Using a frequency selective surface allows for a physically small cavity to have the overmoded properties of a larger cavity without having to drastically increase the operational power. Additionally, the use of modified boundary conditions allows for a larger electric field at the edge of the cavity improving the uniformity of heating at the edges. Going further the modified boundary cavity can be used with other mode enhancement methods and spatial combining techniques for improved heating uniformity. These two FSS only preliminary designs and more in depth design taking into account the substrate temperature performance, the cavity feeding methods, and interaction with the loading material should be investigated.

5.4 Other Directions for Future Work

5.4.1 Alternative Probe Designs

A key limitation of the measurement setup discussed in Chapter 4.2.1 is the waveguide probe impedance mismatch. In all of the demonstrations in this thesis, the probes used to couple solid-state generated power into the cavity are rectangular waveguide adaptors. While they are convenient for characterization and can handle high power, they are large and the performance is heavily dependent on the loading material. For the low-dielectric constant paper loading, it is shown that the VSWR can be improved by changing the relative phase between the probes. However, for the meat loading this is not an option due to the lack of coupling between the two probes. Several probes that couple power over a wide variety of dielectric constants were considered. One example is a probe based on a two arm logarithmic spiral with a dielectric-filled cavity. The cavity backing reduces the bandwidth, which is not of concern for this narrowband heating application. For a high-power handling, the dielectric used in this specific probe needs to be chosen for power and temperature handling, e.g. a ceramic such as Aluminum Oxide [72], Silicoaluminum Carbonite [73], or Zirconium Tin Titanate [74] which can all handle temperatures above 1000°C.

5.4.2 Thermal Considerations

With desired operating temperatures exceeding 400°C the the cavity will need to be able to maintain efficient electrical and thermal performance at these temperatures. Insulation surrounding the cavity helps reduce thermal losses, but will need to be designed for the high temperatures. The expansion of the metal for different components will effect the electrical performance and will need to be understood and compensated for in the system. Finally though the amplifiers will not be operating at these high temperatures the current set up has a metal connection from the outside of the cavity through the outside conductor of the coaxial cable to the ground of the amplifier microstrip circuit. This allows a path for heat to get from the cavity to the amplifier reducing it's performance or causing potential damage. Thermally isolating the cavity from the transistors would prevent this and a feeding system where the microwave energy can efficiently transfer to the heating cavity while having high thermal isolation would be a good direction for future work.

5.4.3 Frequency scaling/multiple frequencies

Using multiple frequencies allows for the combination of the benefits of both frequencies. Lower frequencies have better penetration depth and can heat the center of high loss materials more efficiently than higher frequencies. Higher frequencies allow for more modes within the cavity and provide more uniform heating around the edges of the cavity. 915 MHz and 2.45 GHz are the common bands used for heating and could be combined inside a single cavity. Going to higher frequencies the PA efficiency and output power decrease and at lower frequencies the cavity dimensions become a limiting factor in the modes that can be generated. However further investigation into the trade offs of combing different frequencies and their electrical interactions would be interesting to investigate.

5.5 Part I Summary and Conclusions

In summary, microwave heating of waste results in chemical breakdown that can lead to conversion of mixed waste materials to fuel. Heating waste mixtures with microwave energy rather than incineration results in faster breakdown and can therefore be more efficient. Here we address heating of small volumes of mixed food waste materials with widely differing and temperature-dependent electrical properties. Uniform heating is accomplished with mode mixing within a loaded cavity and by spatial power combining of solid-state power amplifiers (SSPAs). This thesis presents a heating comparison of two circuit-combined and spatially-combined 2.45 GHz 70-W 65% efficient GaN SSPAs with controlled relative phase. The heating efficacy is shown to improve by volumetric combining inside the waste loading. The temperature changes in several locations and for several common waste materials and mixtures are investigated and compared to FEM electromagnetic simulations, as well as FDTD multi-physics simulations that incorporate thermal dependence of material properties. The approach is scalable in volume and power, demonstrated by a simulation comparison of the 1.4 liter small cavity to a 5.2 liter volume.

Going forward with this research requires an interdisciplinary approach. Though the heating uniformity and efficacy metrics allow for some evaluation of system performance they are not complete without knowledge of the chemical conversion. For safety reasons this system was not operated above 120°C, which is bellow the desired temperatures of pyrolysis reactions. The effect of high temperature on the materials, probe, PAs, etc, has not been studied in detail. To understand the trade off between uniformity and heating rate better in a real system, chemical analysis of inputs and outputs must be done. Additionally, this is an ongoing area of chemical research and the optimization of a system requires cooperation and feedback between the different electrical and chemical design elements. The work done here has demonstrated the potential for solid-state based scalable microwave heating that with further interdisciplinary investigation has the potential to one day create a full microwave pyrolysis waste-to-fuel system.

5.6 CONTRIBUTIONS

- **Microwave pyrolysis is good for waste-to-fuel conversion.** Showed that the conversion efficiency can be as high as 77.8 % for plastic loadings and 63 % for paper loadings. For all examined loadings, except mixed food waste, the recovered material energy was higher than the calculated DC energy.
- **Solid-State PAs are beneficial for microwave heating systems.** Demonstrated that spatial power combining within the waste volume allows for control over the electric field distribution improving heating efficiency and uniformity. Also, demonstrated improvement in uniformity with FM signals compared to single tone excitation in a 1.4 L cavity.
- **GaN amplifiers are good for high power microwave heating applications.** Demonstrated GaN based solid-state personal microwave trashcan, 1.4L, up to 130 W delivered power from two 2.45 GHz amplifiers. Additionally, high efficient (above 70%) GaN kW amplifiers have been published in this frequency range to improve the heating rates through further power scaling.
- **Simulations allow for improved design of heating systems.** Compared multiphysics simulations with heating measurements. These predicted heating trends in general regions of the cavity.

The results and contributions of Part I of this thesis are published in [48, 60, 64, 65].

CHAPTER 6

PART II: ANALOG INTERFERENCE SUPPRESSION FOR BROADBAND RECEIVERS; INTRODUCTION AND BACKGROUND

Broadband receivers are susceptible to interference, and a large interfering signal can saturate the low noise amplifier (LNA), mixer, and/or analog to digital converter (ADC). Interference cancellation is often done digitally after down-conversion, but this becomes difficult in large bandwidth cases. Generally, interference is classified as self-interference and external interference, and can be in be in-band and out of band, illustrated in Fig. 6.1.

The goal of this work is to suppress high power out-of-band signals, which can be applied to both self and external interferers covering the 2–4 GHz octave and illistrated in Fig. 6.1. The approach presented here is for signals that do not overlap spectrally with the desired signal.

6.1 BACKGROUND

Broadband recievers are incredibly useful as the same hardware can be used to receive signals over a wide frequency range allowing for different regions of the spectrum to be either separately or simultaneously.

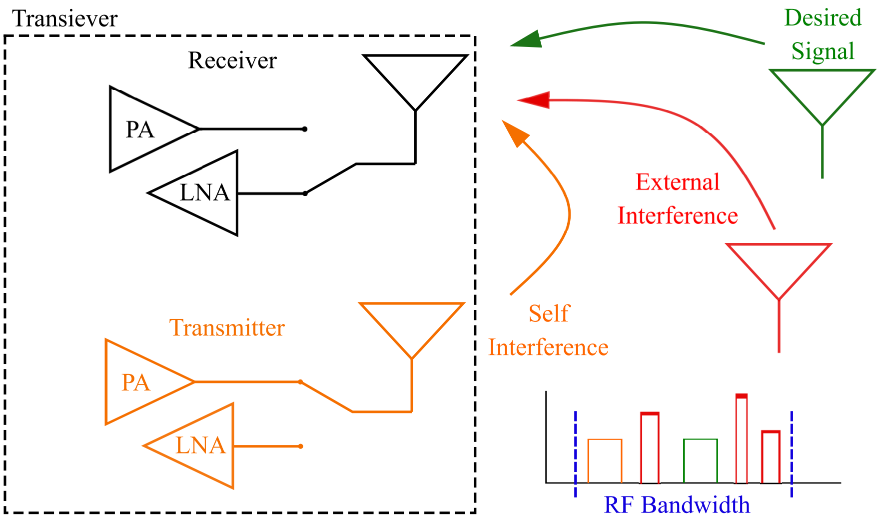

Figure 6.1: Sketch of various forms of interference in a broadband phased array. The operating RF bandwidth is shown in blue and is in this work assumed to be an octave.

However, the high RF bandwidth also allows many unwanted signals to fall within the RF band of operation. These unwanted signals cause problems for the receive side by saturating the receive chain components, i.e. LNA, mixer and ADC. To mitigate this, some method of interference suppression is needed. There are a variety of different methods that are currently in use with a summary of self-interference methods are detailed in [75]. These can be categorized by where in the system they are implemented as propagation, analog and digital domains. Propagation-domain suppression includes passive, active, and antenna interface methods. Passive methods include antenna separation, orientation and polarization, adding absorber or reflectors to reduce cross talk between the transmit and receive antennas. Active methods include beam forming in transmit mode, and tapped feedback coupling networks where transmit signals are coupled into receive part for cancellation. Circulators and duplexers are antenna interface methods to reduce the coupling from the propagation domain. Often more than 100 dB of suppression is needed, requiring multiple methods to be used in conjunction, with digital cancellation used in almost all systems upon downconversion. An interesting way to characterize total cancellation in this case is shown in Fig. 6.2 for narrowband self-interference demonstrations published over the past decade. However, for the relatively broadband signals a combination of all three is benefitial.

The work in this thesis focuses on analog-domain active cancellation, the most common example of

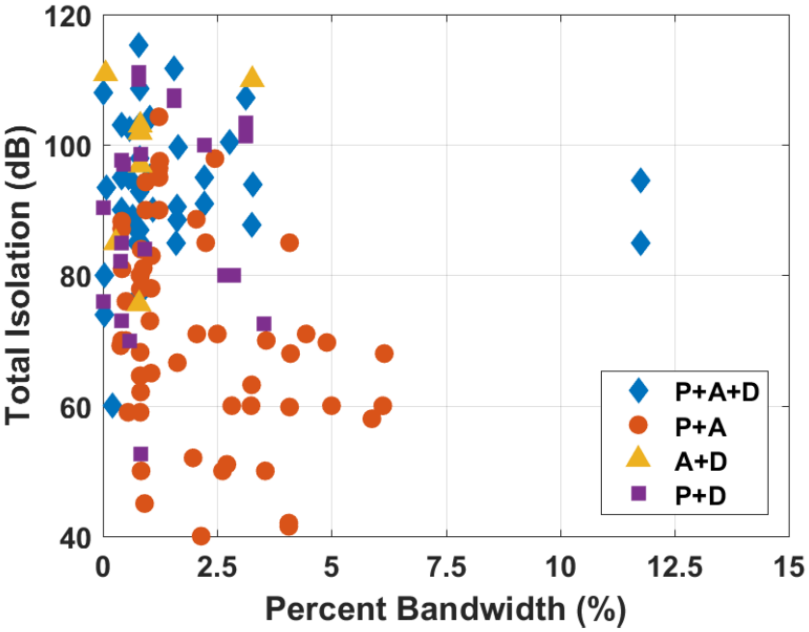

Figure 6.2: Survey of measured isolation versus percent bandwidth for in-band full duplex (IBFD) systems using a combination of propagation (P), analog (A), and digital (D) methods for self interference cancellation, reproduced from [[23], Figure 1.8]

which is tapped feedback, described in detail in [75]. For self interference this method often relies on pre-determined knowledge of the system transfer function which is used to determine the tapped feedback parameters as explained in [76]. For suppressing out-of-band interference, especially relevant for broadband receivers, a possible solution are electronically-tunable passive filters. These are extensively reported in the literature, e.g. [77–79], but can be lossy and/or bulky. A general overview of many types of interference suppression circuits for reconfigurable front ends is given in [80], including analog finite impulse response (FIR) filters, which have been implemented in CMOS [81, 82] and GaAs [83], designed for use as equalizers in optical communication systems. The CMOS implementations usually have switched delay lines or switched capacitor banks, often referred to as N-path filters, which can be used in both in-band self [84] and out-of-band interference [85, 86], and are limited in input power handling, e.g. 80 mW in [82]. A similar idea has been used in RFID for broadband leaking carrier suppression, where an analog FIR filter is used to approximate the leakage channel in amplitude and phase across a wide band to effectively suppress the leaking carrier signal and its noise components [87]. Direct-conversion mixer-first receivers have been used for selecting a subsection of the system RF bandwidth in a passive homodyne SDR system [88], carrier aggregated LTE system [89], and a 10 MHz LTE system [90]. However, these require more complex and power-hungry digital backends, and noise is higher since there is no LNA before the mixer. On the other hand, feed-forward designs leverage benefits of narrow filtering at IF frequencies with better sensitivity than mixer-first topologies by splitting the signal after, or in parallel with, an LNA [91–93].

6.2 Analog Interference Suppression Circuit (AISC)

redThe AISC presented here for out-of-band interference suppression in wideband receivers. The circuit is a two-branch hybrid interferometer with a variable delay line implemented as a GaN MMIC, shown in Fig. 6.3. This circuit performs the function of a tunable, absorptive bandstop filter and can be inserted between the antenna port and LNA of a receiver. The aim of the circuit is to provide interference suppression of high power unwanted signals covering the 2–4 GHz bandwidth. It is important that the system maintains performance under high power conditions so that the desired signal can still be received in the presence of a high power interferer.

When two simultaneous signals at different frequencies in the 2-4 GHz octave band are incident at the input, a notch can be placed at one of the frequencies by controlling the voltage on the variable delay line. The attenuator and extra delay in Path 2 ensure destructive interference at the output. The true time delay is key for broadband operation, while implementation in a wide bandgap semiconductor (GaN) results in improved linearity and power handling. The implementation of varactors as pinched-off high electron mobility transistors (HEMTs) in a wide bandgap semiconductor (GaN) and the omission of active transistors results in improved linearity and power handling. In this case, the power handling is limited by the output power combiner and the large-signal performance of the variable capacitors in the delay line. This means that this design using GaN MMICs can operate at higher powers than other continuously tunable filters. Additionally, the AISC topology does not rely on resonators and can be miniaturized through full integration. This approach can be expanded to multiple simultaneous notches by having two interferometer based AISCs in series or combining in parallel, and a design using the latter method is presented in Chapters

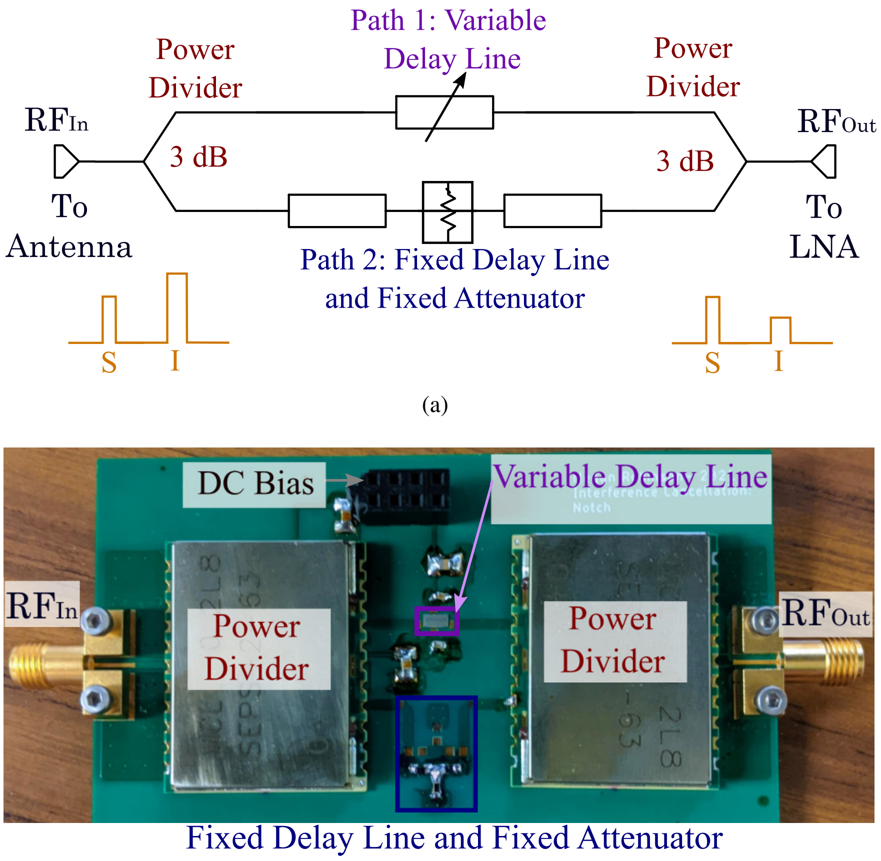

(a)

(b)

Figure 6.3: (a) Labeled block diagram of an analog interference cancellation circuit (AISC). (b) Photograph of the printed circuit boards showing surface mount reflectionless 3-dB couplers, the delay line GaN MMIC in Path 1, and fixed delay lines and attenuator in Path 2.

7 and 11.

The AISCs presented here are designed to be used with digital and propagation methods for improved interference suppression. As shown in Fig. 6.2, using a combination of propagation, analog, and digital methods is needed for high isolation. Especially in broadband systems, analog together with digital cancellation provides better system performance over using either one alone. Digital cancellation can provide a large degree of suppression, but still requires linear operation of receiver frontends and ADCs [94]. Therefore, analog linear suppression circuits can provide the necessary coarse suppression to make digital cancellation feasible by reducing the strain on ADCs and mixers before the signal gets converted into the digital domain.

6.3 OVERVIEW OF PART II OF THE THESIS

In the remainder of the thesis, first a simplified circuit theory of the interferometer is presented (Chapter 7). Second, the design of a 2–4 GHz AISC using GaN MMIC delay lines is presented and detail on the design and characterization of two types of delay lines is given (Chapter 8). Chapter 9 then describes the design and performance of the AISC topology for suppressing one interferer and using GaN MMIC delay lines from Chapter 8. Chapter 10 presents delay line circuits at higher frequencies, as well as a comparison of GaN and GaAs delay line based phase shifters. Finally, Chapter 11 concludes Part II of the thesis with avenues for future research, including an extension to a circuit that can create two independently tunable notches.

CHAPTER 7

THEORY OF AISC APPROACH

7.1 INTRODUCTION

To design and understand the interferometer for interference suppression the circuit was analysed starting from a simplified circuit model. Fig. 7.1 defines the parameters used in the simplified analysis. The input signal to the interferometer $\underline{S}_{\text{in}}$ passes through a power divider where it is split into components $\underline{S}_1(f) = S_1(f)e^{j\theta_1(f)}$ and $\underline{S}_2(f) = S_2(f)e^{j\theta_2(f)}$.

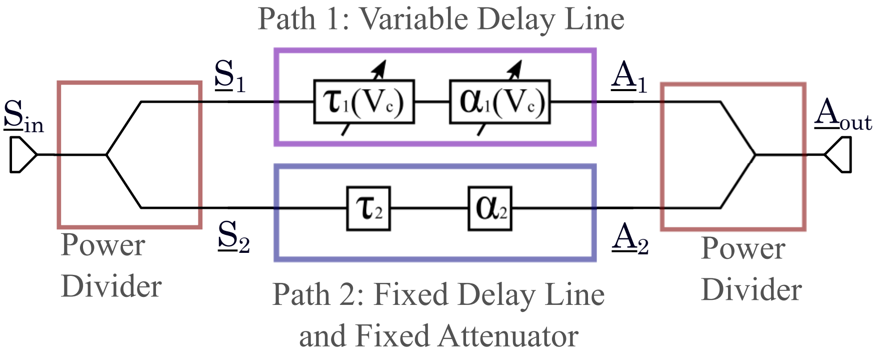

Figure 7.1: Circuit diagram of the inteferometer, showing the input signals, delays, attenuation and output signals.

The signals are then delayed in the two paths. The signal in Path 1 attenuates and is delayed as a function of the control voltage V_c, resulting in signal $\underline{A}_1$ at the input of the combiner:

$$\underline{A}_1 = A_1(f)e^{\phi_1(f)} = \alpha_1(f, V_c)S_1(f)e^{j\theta_1(f)-j2\pi f\tau_1(V_c)}, \tag{7.1}$$

where α_1 and τ_1 are the amplitude and delay of Path 1, respectively. Similarly, the signal $\underline{A}_2$ at the input of the combiner in Path 2 is

$$\underline{A}_2 = A_2(f)e^{\phi_2(f)} = \alpha_2(f)S_2(f)e^{j\theta_2(f)-j2\pi f\tau_2}, \tag{7.2}$$

where the amplitude α_2 and delay τ_2 and fixed. At the output of the combiner, the total signal becomes:

$$\underline{A}_{\text{out}} = A_1(f)e^{\phi_1(f)} + A_2(f)e^{\phi_2(f)}, \tag{7.3}$$

where we assume a perfect lossless in-phase combiner. Any amplitude or phase unbalance can be included in the frequency response of the input power divider without loss of generality. Assuming a frequency dependence in $A_i(f) = A_i$ and $\phi_i(f) = \phi_i$, the output signal can be written as

$$\underline{A}_{\text{out}} = A_1 e^{\phi_1}\left(1 + \frac{A_2}{A_1}e^{\phi_2-\phi_1}\right), \tag{7.4}$$

and its amplitude can be written as

$$|\underline{A}_{\text{out}}| = A_1 \cdot \sqrt{1 + \left(\frac{A_2}{A_1}\right)^2 + 2\frac{A_2}{A_1}\cos(\phi_2 - \phi_1)}, \tag{7.5}$$

where the phases can be expressed as $\phi_i(f) = \theta_i - 2\pi f\tau_i$, and their difference is

$$\phi_2(f) - \phi_1(f) = \Delta\theta - 2\pi f\Delta\tau, \tag{7.6}$$

where $\Delta\theta = \theta_2 - \theta_1$ and $\Delta\tau = \tau_2 - \tau_1$. Fig. 7.2 shows a plot of equation (7.5) as a function of normalized frequency f/f_N, where f_N is the center frequency of the notch, for different ratios (A_1/A_2). We observe that perfect cancellation occurs at $f = f_N$ corresponding to $\phi_2 - \phi_1 = \pi$ and for an amplitude ratio of $A_2/A_1 = 1$. Deviating from this amplitude ratio results in a wider and shallower notch, but does not change the frequency of maximum cancellation. Therefore, the effects of amplitude imbalance can be separated from the frequency response.

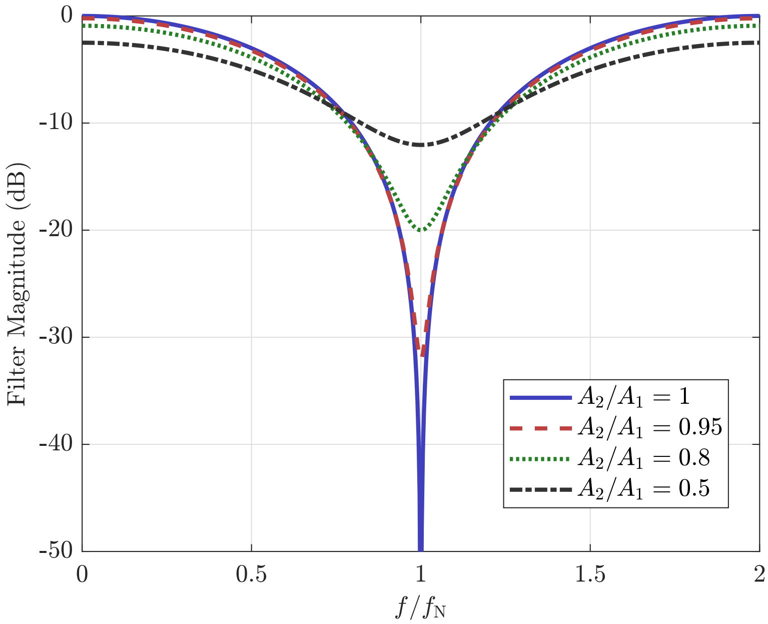

Figure 7.2: Magnitude $|\underline{A}_{\text{out}}|$ compared to f/f_{N} and output of the notch circuit when $A_1 = 1/\sqrt{2}$ for different amplitude ratios A_2/A_1.

For $A_1 = A_2 = \frac{1}{2}$, the output magnitude is

$$|\underline{A}_{\text{out}}| = \frac{1}{2}\sqrt{2 + 2\cos(\phi_2 - \phi_1)}, \tag{7.7}$$

with a notch occuring periodically according to

$$\phi_2(f) - \phi_1(f) = 2n\pi - \pi, \quad \forall n \in \mathbf{Z}. \tag{7.8}$$

Replacing ϕ_i from Eq. (7.6) the frequency of maximum cancellation can be expressed as:

$$f_{\text{N}} = \frac{\pi + \Delta\theta}{2\pi\Delta\tau} + \frac{n}{\Delta\tau}, \quad \forall n \in \mathbf{Z}. \tag{7.9}$$

We note that notches occur periodically with a spacing of $1/\Delta\tau$, and the the phase difference between paths $\Delta\theta$ shifts them in frequency, while the delay difference between paths $\Delta\tau$ scales the frequency separation between notches.

To find the bandwidth of the notch we assume a suppression ratio in dB as illustrated in Fig. 7.3 for 20 and 30 dB suppression ratios. The bandwidths for the two cases (depicted with the symbols 'x' and '$\Diamond$' in

Fig. 7.3) are related to the delay difference $\Delta\tau$, the suppression ratio (SR) and the center frequency of the notch. In general, it is straightforward to solve for the bandwidth given a specific suppression ratio:

$$B = 2\left(f_{\mathrm{N}} - \frac{\Theta_{SR} + \Delta\theta}{2\pi\Delta\tau}\right), \tag{7.10}$$

and

$$\Theta_{SR} = \cos^{-1}\left(\left(\frac{2}{SR^2}\right) - 1\right), \tag{7.11}$$

where SR is in linear units. Using Eq. (7.9) we compute the normalized notch bandwidth as

$$\frac{B}{f_{\mathrm{N}}} = \frac{2\pi - 2\Theta_{SR}}{2n\pi + \pi + \Delta\theta} \qquad \forall n \in \mathbf{Z}. \tag{7.12}$$

The normalized notch bandwidth for a given suppression ratio depends on the phase shift $\Delta\theta$ and the notch index n, but not on $\Delta\tau$, as illustrated in Fig. 7.4. For the same suppression ratio a larger n leads to a narrower notch, a feature that is generally desireable in notch filters. Additionally, a fixed positive phase shift, $\Delta\theta$, can reduce the notch bandwidth, as shown for the $n = 0$ case in dashed lines in Fig. 7.4. However, there is a tradeoff between the notch bandwidth and the tuning range of the filter, as investigated next.

An important understanding of the notch bandwidth is the achievable suppression for a given tone spacing between the desired and interfering signals. Ideally a smaller bandwidth meaning more suppression for tones closer together is desired, Fig. 7.5. However, there is a trade off between the settings that provide the best separation between tones and the tuning range. This can be seen with the $n = 3$ case for Fig. 7.5(a) having

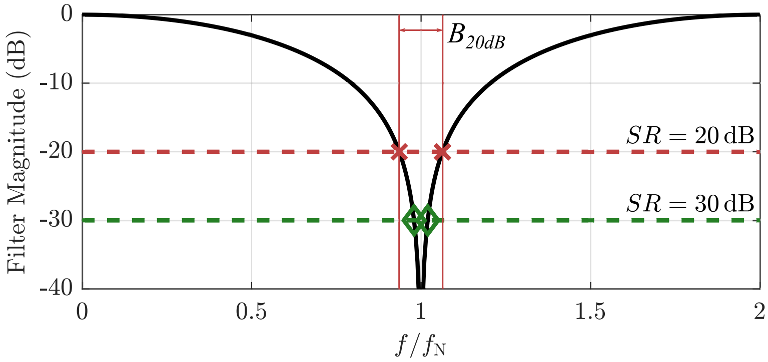

Figure 7.3: Magnitude $|\underline{A}_{\mathrm{out}}|$ compared to f/f_{N} and output of the notch notch circuit when $A_1 = 1/\sqrt{2}$ when $A_2/A_1 = 1$. The supression ratio is shown with the dashed lines for both 20 and 30 dB cases. The notch bandwidth is shown with the symbols 'x' and '◊' for the 20 and 30 dB cases respectively.

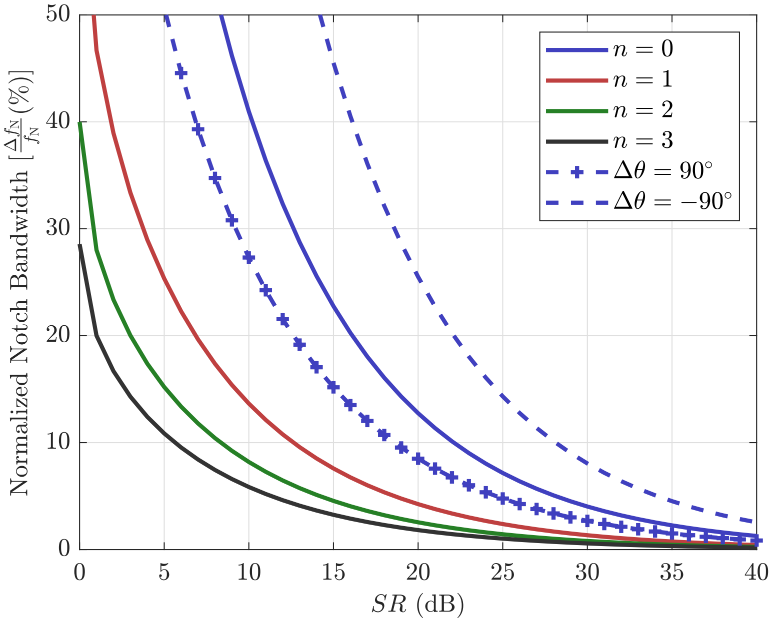

Figure 7.4: Normalized notch bandwidth compared to the minimum suppression ratio when $\Delta\theta(f) = 0$ for the first notch ($n = 0$), second notch ($n = 1$), third notch ($n = 2$), and forth notch ($n = 3$). The dashed lines show the effects of a +/-90° phase shift to the $n = 0$ notch.

the largest suppression for close tones, but the next notch starts to reduce the suppression around 500 MHz above the desired notch.

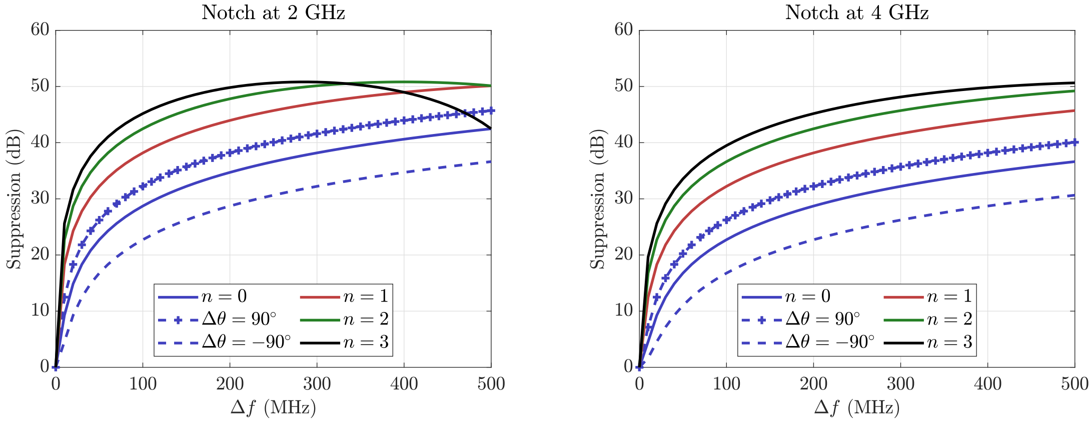

(a) (b)

Figure 7.5: Suppression level compared to tone separation, frequency between the interference and desired signal, with 0.05 dB of amplitude mismatch between the two paths with a notch, f_N, set at (a) 2 GHz and (b) 4 GHz.

As previously stated the normalized notch bandwidth is the same for notch frequency settings and depends on the notch order, n, and the phase shift between the lines, $\Delta\theta$. The amplitude imbalance has an important impact on the separation where the larger the mismatch the less suppression that can be achieved, depicted in Fig. 7.6

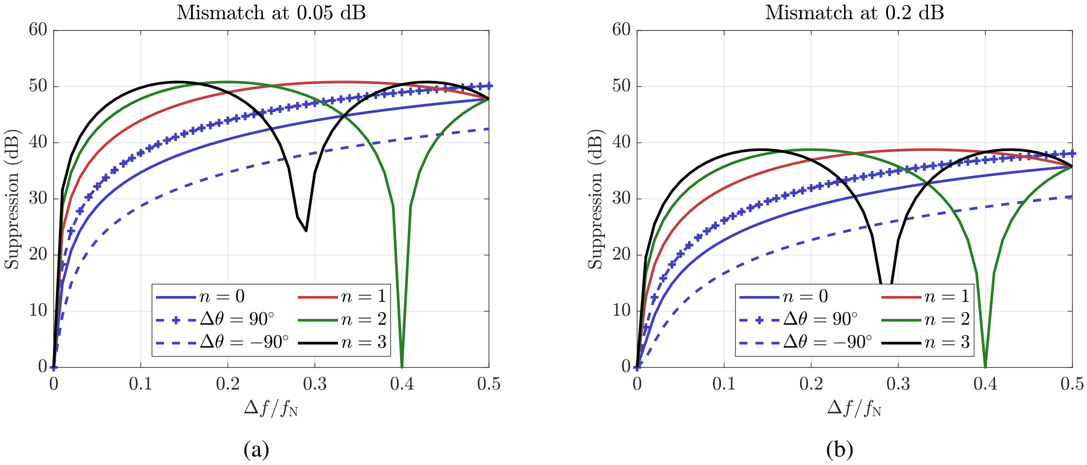

(a) (b)

Figure 7.6: Suppression level compared to normalized tone separation, frequency between the interference and desired signal divided by the notch frequency, with (a) 0.05 dB and (b) 0.2 dB of amplitude mismatch between the two paths.

7.1.1 Tuning bandwidth

The useful tuning range of the notch center frequency f_N is limited by the frequency of the next higher-order notch, illustrated in Fig. 7.7, since it doesn't make sense to have multiple notches within a band. The possible notch frequencies for 4 notch orders are shown in Fig. 7.7(a), illustrating that for $n = 0$ (blue) and for $\Delta\tau = 167$ ps, there is notch at 3 GHz. When tuning the delay to 0.5 ns, the second-order notch appears. Fig. 7.7(b) shows that the first notch tunes lower in frequency as the delay is increased, and the second notch appears at the initial first notch frequency for a delay of 0.5 ns. The plots assume that there is no considerable dispersion of $\Delta\theta(f)$. If the dispersion is linear, it can be mathematically included in the time delay of one of the paths.

To quantify the tuning, Eq. (7.9) can be rewritten as:

$$f_{\mathrm{N}n} = \frac{2\pi n + \pi + \Delta\theta}{2\pi(\Delta\tau)}, \quad \forall n \in \mathbf{Z} \tag{7.13}$$

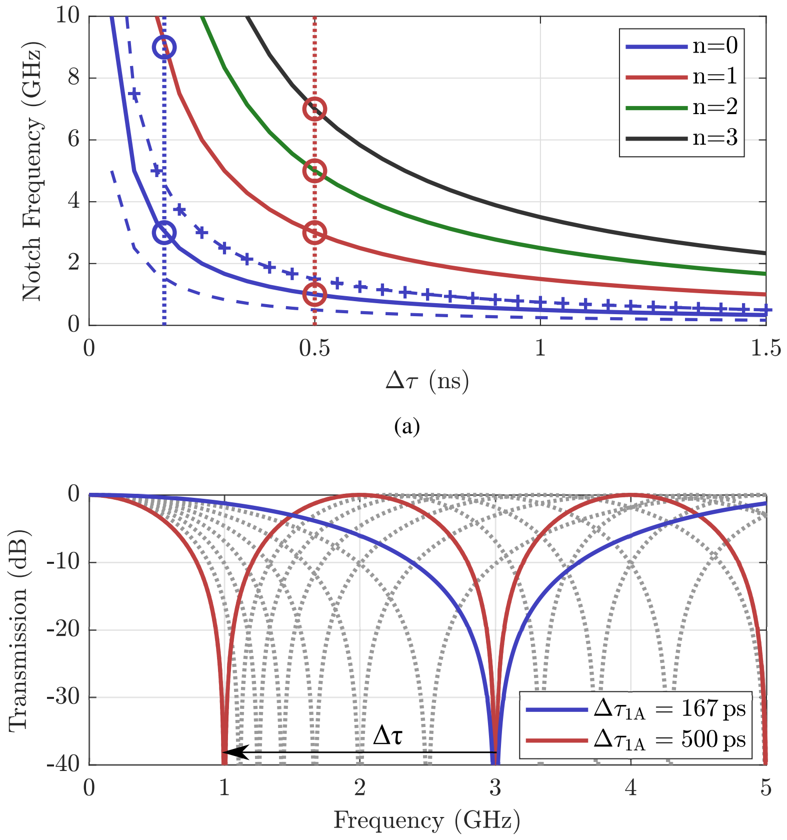

(a)

(b)

Figure 7.7: (a) Notch frequency f_{N} compared to $\Delta\tau$. It is shown in terms of GHz and ns however the entire graph scales even to Hz and s. (b) The magnitude vs frequency for $\Delta\tau = .167\,\mathrm{ns}$, and $\Delta\tau = .5\,\mathrm{ns}$, the cross section indicated by the dashed blue line and the dashed red line in (a).

The ratio between neighboring notch frequencies becomes

$$\frac{f_{\mathrm{N}(n+1)}}{f_{\mathrm{N}n}} = \frac{(2n+3)\pi - \Delta\theta}{(2n+1)\pi - \Delta\theta}. \tag{7.14}$$

When $\Delta\theta(f) = 0$, the first notch ($n = 0$) has a tuning ratio of

$$\frac{f_{\mathrm{N1}}}{f_{\mathrm{N0}}} = \frac{3}{1}. \tag{7.15}$$

In Fig. 7.8 the effect of adding a fixed phase shift between the lines is shown. In contrast to the notch bandwidth, the tuning ratio increases when a negative $\Delta\theta$ is added. Note that any tuning ratio can be chosen if a fixed phase shift is added to the design and the delay can be chosen accordingly.

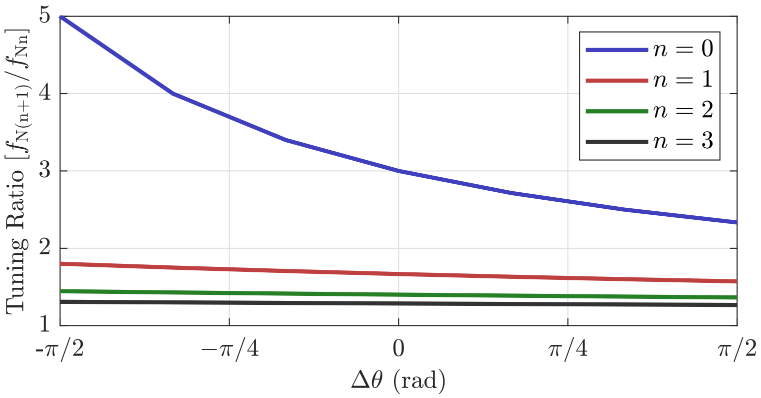

Figure 7.8: Fractional tuning bandwidth compared to $\Delta\theta(f)$ for different notch settings ($n = 0, 1, 2, \&3$).

7.1.2 Extension to Two Notches

The four-branch interferometer can be viewed as two parallel dual-branch circuits with a relative delay. Referring to Fig. 7.10, each subcircuit consists of two branches with gain G, fixed delay lines D_1 and variable delay lines $\Delta\tau_1$. In the four-branch final circuit, there is an additional delay $\Delta\tau_2$ between the two subcircuits. The variable lines create delays T_i in each of the four branches given by:

$$T_2 = \Delta\tau_1 + T_1, \quad T_3 = \Delta\tau_2 + T_1, \quad \Delta\tau_1 + T_3$$

where $T_1 = D_1$ is the fixed delay. The key principle is that the difference in delay between the lines inside both interferometer subsections $\Delta\tau_1$ creates a notch at frequency f_1, while $\Delta\tau_2$ creates a notch at a second frequency f_2. These frequencies correspond to relative delays that result in destructive interference, i.e. when the phases in the two paths at a given frequency are $(2n + 1)\pi$ apart, resulting in $f = 1/2\Delta\tau$. In order to have comparable loss in all four branches, the delay D_1 is modified to C_1 which is chosen to make the shortest and longest delays equal to:

$$T_{1,4} = C_1 \mp \frac{1}{4f_1} \mp \frac{1}{4f_2}, \tag{7.16}$$

making the other two delays equal to

$$T_{2,3} = C_1 \pm \frac{1}{4f_1} \mp \frac{1}{4f_2}. \tag{7.17}$$

For the edges of the frequency band chosen to be the 2 – 4 GHz octave, the final delays become:

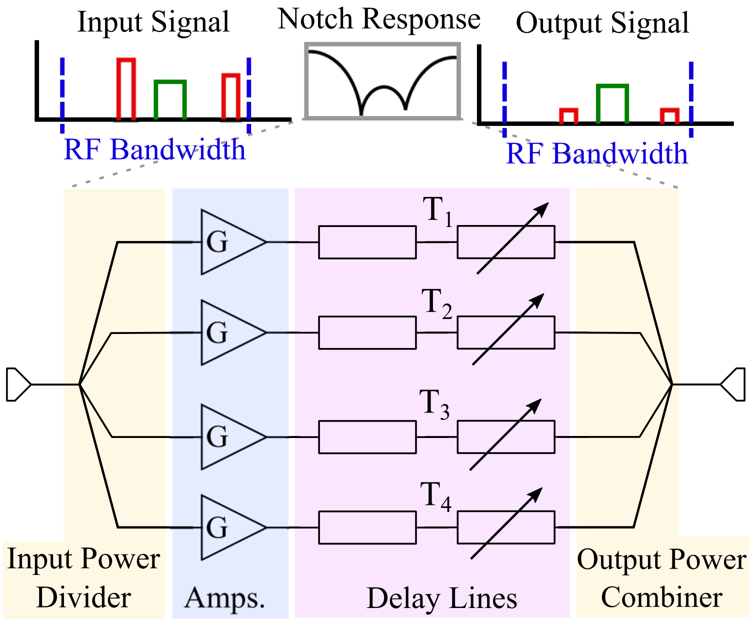

Figure 7.9: Diagram of the tunable dual notch circuit with gain depicting the interference suppression of two unwated signals either side of the desired signal within the RF bandwidth.

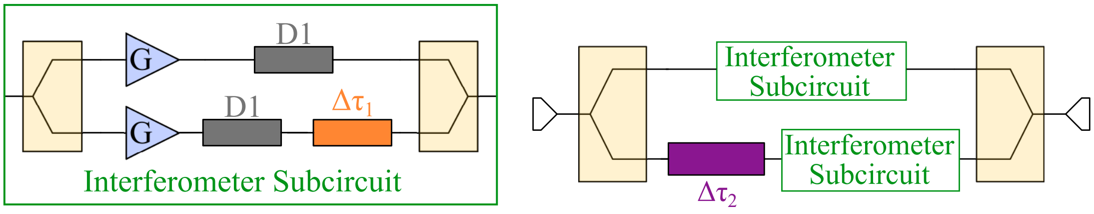

(a)

(b)

Figure 7.10: Ideal notch circuit topology used to analyse the topology and determine parameters for the board design. (a) Block diagram of a two-branch interferometer that creates the first notch. (b) Block diagram of combined interferometer subcircuits with additional delay to create the second notch.

$$\begin{aligned}
T_1 &= C_1 - 187.5 \pm 62.5\,\text{ps} \\
T_2 &= C_1 \pm 62.5\,\text{ps} \\
T_3 &= C_1 \pm 62.5\,\text{ps} \\
T_4 &= C_1 + 187.5 \pm 62.5\,\text{ps}
\end{aligned} \tag{7.18}$$

For an actual physical implementation, the shortest line is obtained for $C_1 > 187.5\,\text{ps}$.

7.2 CHAPTER SUMMARY

The analysis of the simplified interferometer circuit demonstrates that an octave tuning bandwidth can be achieved. Although idealized, the theory reveals useful trends and is a good starting point for design. Additionally, the tradeoff between notch bandwidth and tuning range is discussed, one conclusion is that for a reduced tuning bandtwidth a higher order notch would be desirable. These delay lines are next used in an expansion to multiple paths allows for the same variable delay lines to be used to create multiple simultaneous notches. The next chapter covers the design and small signal circuit performance of two broadband delay lines operating over the desired 2–4 GHz. These delay lines will then be used for PCB implementations of the AISC.

CHAPTER 8

VARIABLE DELAY LINES FOR AISCS

8.1 INTRODUCTION

In the previous chapter, a simple theory of the AISC is presented, with a tunable true-time delay as one of the main parameters. In this chapter, the tunable delay design is described in detail. It is implemented with a lumped-element transmission line loaded with variable capacitors, and an ideal lossless line is shown in Fig. 8.1. The general block diagram shows a non-uniform transmission line where the inductor and capacitor values vary along the length of the line. In this chapter, both a uniform and non-uniform line are designed and implemented as GaN MMICs, using depletion-mode high-electron mobility transistors (HEMTs) connected as varactors. For a uniform line with equal inductances L and capacitors C, the phase velocity is given by $\beta = \omega\sqrt{LC(V_C)}$ and the delay is $\tau = N\sqrt{LC(V_C)}$, where N is the number of sections and V_C is the dc control voltage across the varactor. The characteristic impedance of such a line is $Z_0 = \sqrt{L/C(V_C)}$ and should be matched to the generator and load for all values of the control voltage. In a realistic delay line, the inductors and capacitors have losses, which are considered in the next section.

In this chapter, the implementation in a GaN-on-SiC MMIC process by WIN Semiconductors is described. This process has two metal layers for passive circuits, backside vias through a 100-μm SiC substrate, with metal-insulator-metal silicon nitride (SiN) capacitors, thin-film resistors and mesa resistors. The active

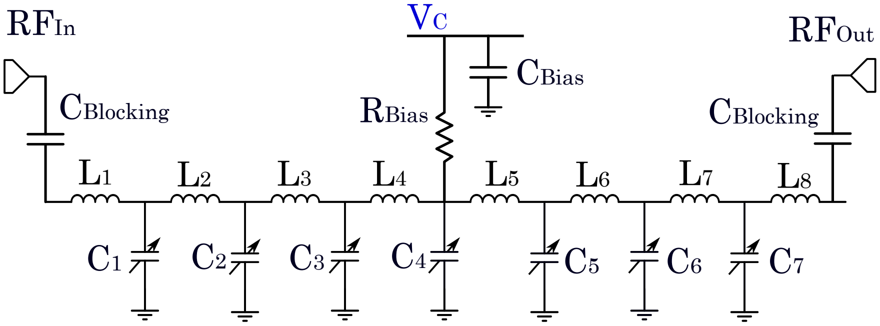

Figure 8.1: Circuit schematic of an ideal lossless tunable true-time artificial transmission line delay, consisting of inductors and variable capacitors.

devices are depletion mode HEMTs with $4 \times 50\,\mu$m devices validated scalable models. The thin film resistors are blank and have a sheet resistance of $50\,\Omega/\square$. The mesa resistors have a sheet resistance of $515\,\Omega/\square$. The SiN capacitors have a thickness of 2700 Å and a capacitance density of 215 pF/mm^2.

8.2 Lumped MMIC Inductors and Variable GaN HEMT Capacitors

In a MMIC implementation, spiral inductors are used for the L_i elements of Fig. 8.1. These are implemented using two connected metal layers for reduced ohmic loss, with a bridge in the top metal layer, as shown in Fig. 8.2. The inductors are not measured separately, and full-wave simulations of the impedance using the realistic process-design kit (pdk) materials are shown in Fig. 8.2. From here, it is seen that a 1 nH inductor has a series resistance of approximately 1.9 Ω quoted at 3 GHz from a fitted circuit model. The inductors perform well up to 5 GHz, as the frequency increases the loss makes it impractical to use inductors without adding in gain to compensate. For the frequency range of interest, $R \ll \omega L$.

Most varactors in GaN are implemented based on the gate-to-channel capacitance of a HEMT structure, where separate drain and source contacts are either omitted in the layout [95, 96], or shorted together [97]. Since the capacitance variation occurs for a relatively small voltage swing the linearity is low, but can be improved by using an anti-serial connection [98].

The variable capacitance in this work is implemented as a cold-FET topology using a standard HEMT device, as shown in Fig. 8.3. The gate is biased at -20 V for pinch off, such that the varactor is formed by the output capacitance of the cold HEMT. To adjust the capacitance, the drain bias voltage is varied between

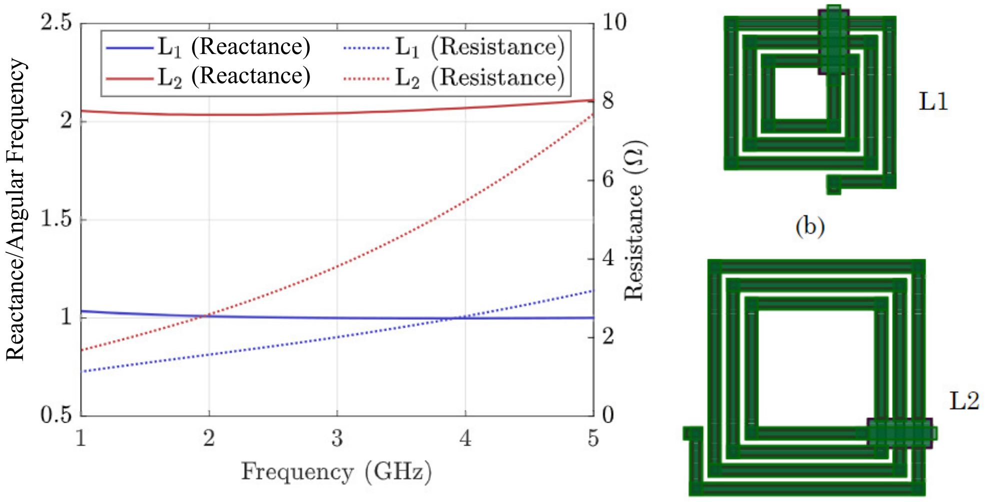

(a) (b) (c)

Figure 8.2: (a) Full-wave simulated impedance of the two inductor sizes used in the delay-line designs from 1 to 5 GHz. (b) Layout of the 1 nH 128 μm square inductor. (c) Layout of the 2.1 nH 180 μm square inductor.

-20 and +40 V. This topology has a larger relative capacitance range of 2.4 to 1 for the measured fabricated capacitors compared to 1.7 to 1 for the diode-connected transistor in simulation. While this topology adds complexity through the requirement of a secondary bias voltage and the bypass capacitor, it expands the tuning bias voltage range from -3 to -1 V to -20 to +40 V. The wider tuning voltage provides improved linearity and high power performance, investigated in the next Chapter.

The nonlinear HEMT model in the WIN process design kit (PDK) is extracted for amplifier design, so we expect the model to only predict trends when the transistors are in a varactor configuration. Therefore, a separate variable capacitor with a 12×100-μm HEMT is fabricated for characterization and comparison with the nonlinear model. The capacitor is measured using an on-wafer SOLT calibration kit, and the measured capacitance extracted from a S_{11} measurement. The comparison with nonlinear simulations is shown in Fig. 8.4. The red curves are extracted capacitance values from a 1-5 GHz one-port simulation for a 12-finger device, while the measured capacitance is shown in black line and has a smaller value and range, indicating that the nonlinear foundry model over-estimates the drain-to-source capacitance in heavy pinch-off conditions. Additionally, the measured device starts drawing current at V_C = -18 V due to reverse conduction in the channel, which does not occur in simulation.

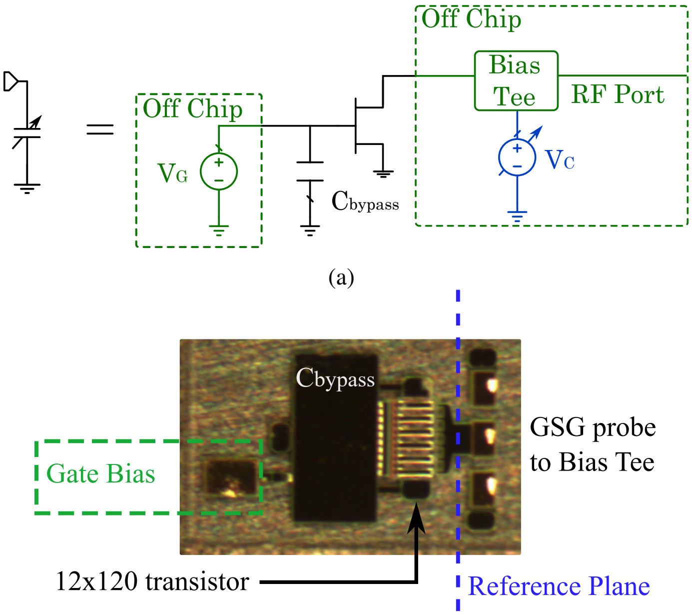

(a)

(b)

Figure 8.3: (a) Circuit schematic of the variable capacitor showing the gate bias and drain control bias circuits. (b) Photograph of a single 12×120-μm device used to extract the capacitance from a one-port measurement calibrated to the reference plane shown in dashed line.

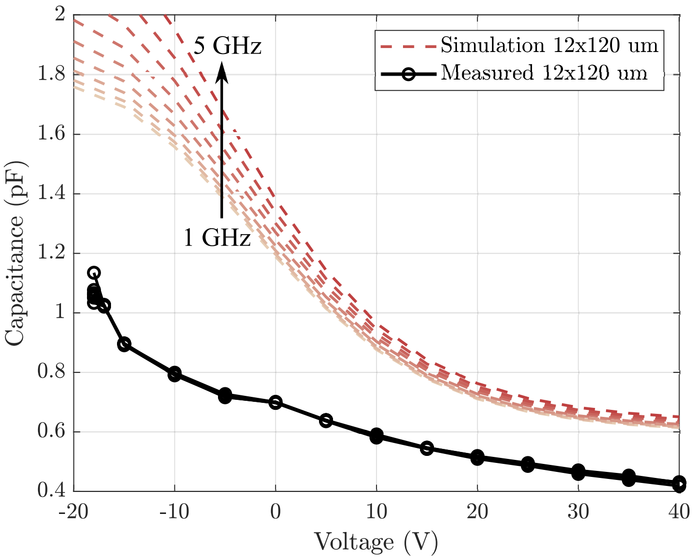

Figure 8.4: A comparison of measured (black line with symbols) and simulated (red dashed lines) tunable capacitor extracted from one-port measured and simulated data. Both are performed from 1 to 5 GHz, showing little variation in the measured data.

8.3 VARIABLE DELAY LINE MMICs

Using the HEMT variable capacitors as in Fig. 8.3, two artificial transmission-line delays are designed and photographs of the fabricated MMICs are shown in Fig. 8.5. The uniform line has 7 equal capacitors $8\times122\,\mu$m designed to range from 0.4 pF to 1.3 pF with control voltage variation from -20 to +40 V. The inductor values for a 50 Ω line are 2.1 nH, and a Tee unit cell is implemented, so that the edge inductors (L_1 and L_8) are 1 nH.

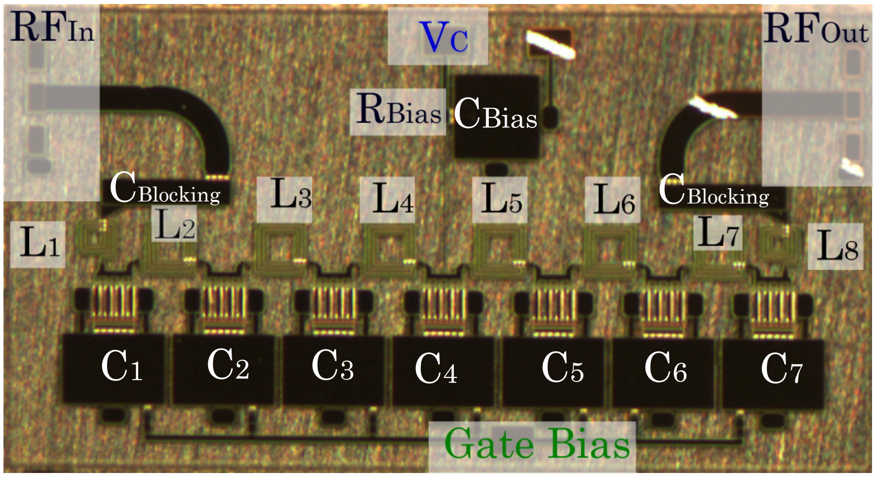

(a)

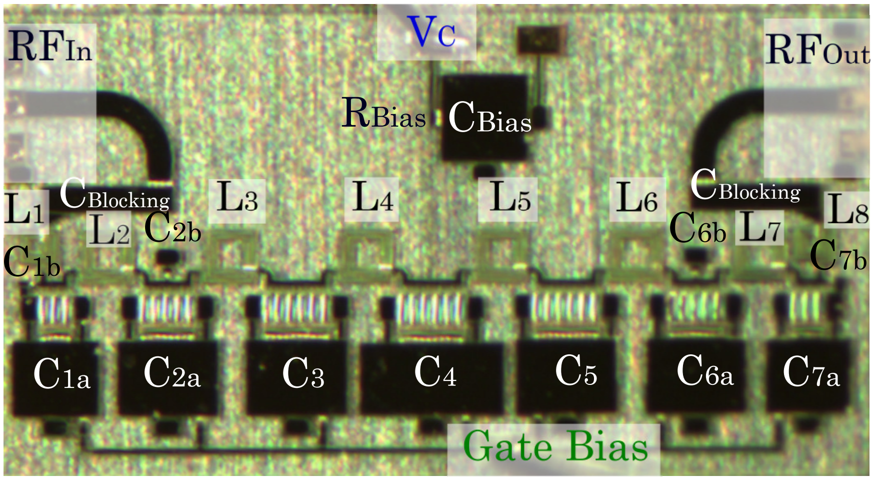

(b)

Figure 8.5: (a) and (b) Photographs of the uniform and tapered delay line die, respectively. Note the different sizes of transistors in the different MMICs. Both MMIC chips are 1.6 mm by 3.0 mm.

The tapered impedance line is designed to have a larger group delay variation for the same minimum

Table 8.1: Capacitance Values of Tapered Delay Line

Capacitor	**Device Size**	**Simulated Capacitance (pF)**	**Measured Capacitance (pF)**
C_1 & C_7	6x108 μm	0.46 – 0.93	0.31– 0.57
C_2 & C_6	10x110 μm	0.51 – 1.4	0.51 – 0.95
C_3 & C_5	12x106 μm	0.6 – 1.4	0.38 – 0.91
C_4	12x120 μm	0.63 – 1.5	0.43 – 1.02

return loss. When tuning only a single reactance element of an artificial transmission line it is impossible to vary the delay without affecting the characteristic impedance and hence the return loss of the line. For the tapered line we employ a larger capacitance variation in the center (capacitors C_3, C_4, and C_5) than at the edge elements, such that the impedance variation at the edge elements is smaller than in the center, as is summarized in Table 8.1. Similar to a tapered transmission line the gradual change in the impedance of the artificial transmission line results in a lower return loss at the edges for the same overall impedance variation.

To implement a lower capacitance variation with the same total capacitance, at the edge elements the smaller varactor cells for C_{1a}, C_{2a}, C_{6a}, and C_{7a} are placed in parallel with fixed capacitors C_{Xb}, as shown in Fig. 8.5(b). The inductors used for the tapered line are identical to those in the uniform line. The resulting characteristic impedance is plotted for each cell of the simulated artificial transmission line of both types in Fig. 8.6 for seven different control voltages. Note that we compute the impedance based on the average of the inductance values adjacent to the capacitors, which leads to the lower impedances for the first and last elements of the uniform line. Note that the impedance of the tapered line varies less for the end elements, only ranging from 40 Ω to 58 Ω, when compared to 35 Ω to 63 Ω for the uniform line, corresponding to a better return loss.

The fabricated delay lines were measured on-wafer with an external SOLT calibration substrate. Fig. 8.7 shows simulated S-parameters for both lines compared to the measured results from 1 to 5 GHz. The match remains below -8.2 dB and -12 dB for the uniform and tapered lines, respectively, in both simulations and measurements. As expected the tapered line has less variation in the impedance match over the voltage tuning range. The transmission coefficient remains approximately constant with tuning voltage in measurement, although simulations show significant variation. This simulation has a wider range of conductance loss

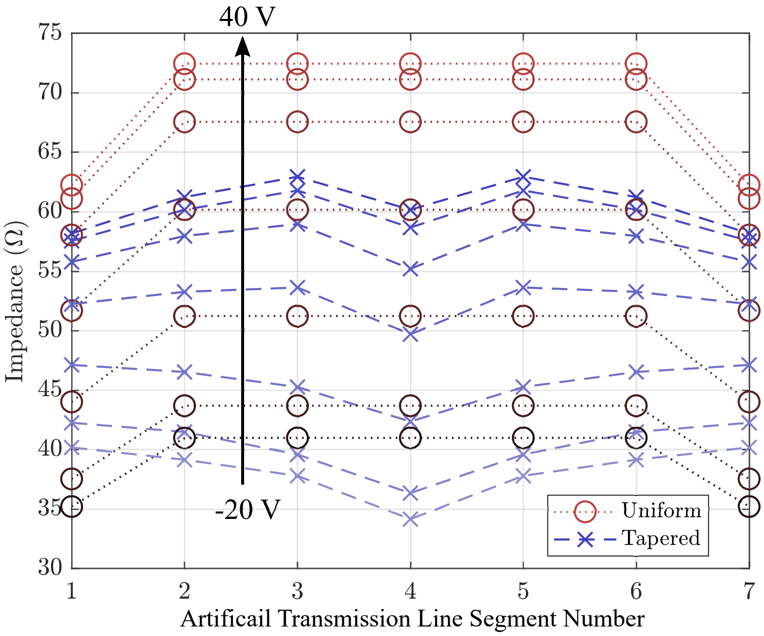

Figure 8.6: Characteristic impedance of each line segment of the simulated regular and tapered artificial transmission lines potted for control voltages of -20 to +40 V with steps of 10 V.

over voltage than the measured results which causes the greater variation in |S21| performance compared to teh measured delay line. The change in capacitance between the simulated and measured lines changes the characteristic impedance of the tapered delay line from 50Ω to closer to 70 Ω. Which increases the mismatch loss of the tared line compared to the simulation. The uniform line which had larger variation in the impedance over voltage is not as sensitive to the change in capacitance.

Fig. 8.8 shows the simulated and measured group delay, showing a variation of 230-350 ps and 260-385 ps at 3 GHz for the uniform and tapered delay lines, respectively. The group delay variation is less than 35 ps across the 2-4 GHz range for the tapered line, and is $<$ 25 ps for the uniform delay line. The total group delay through the measured lines (black) is lower than the simulated group delay (red) for the same voltage settings. This is due to the change in capacitance between the simulated and fabricated circuits and using an scaled model from the measured capacitor by itself (blue) the group delay matches much better to the measured results (black). The slight increase in group delay at the lowest voltage setting is most likely due to the conductance of the capacitors not scaling linearly with size as assumed for the capacitor models in the simulation (blue). Though the change in capactiance value and tuning ratio werre different between

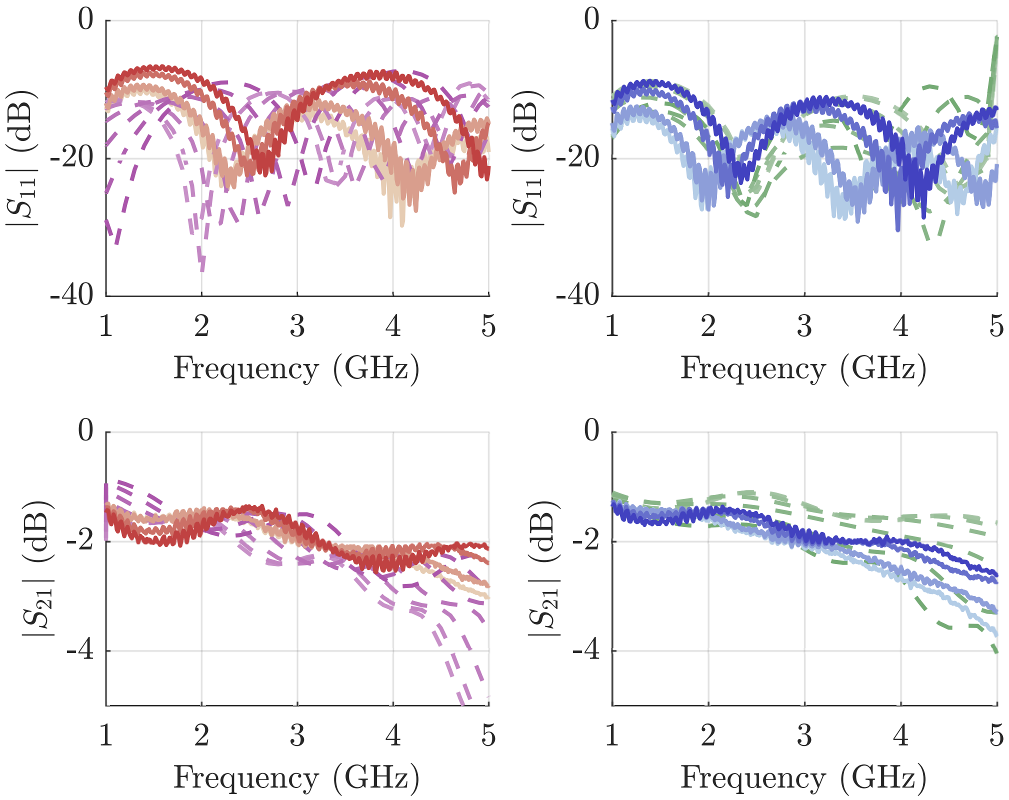

Figure 8.7: Measured (solid) and simulated (dashed) $|S_{11}|$ (top) and $|S_{21}|$ (bottom) for the uniform (left) and tapered (right) tunable delay line MMICs.

the simulation and measurement the delay tuning of the measured lines is above 120 ps which will cover the 2–4 GHz tunable notch using AISC design.

8.4 CHAPTER SUMMARY

Two types of periodically-loaded GaN MMIC delay lines using HEMT varactors are presented: a uniform and a tapered design. The variation between simulated and measured performance of the capacitance for the cold-FET shows that the pdk nonlinear models do not predict transistor behavior in this configuration. This is not surprising since transistor nonlinear models are typically extracted for the most commonly used operation of amplifiers biased in class-AB. Nevertheless, the trends of the measured capacitance variation show that they can be used to implement useful delay lines. The material from this chapter is reported partially in [99] where the delay line is used as a reactive load in a reflection-type broadband phase shifter,

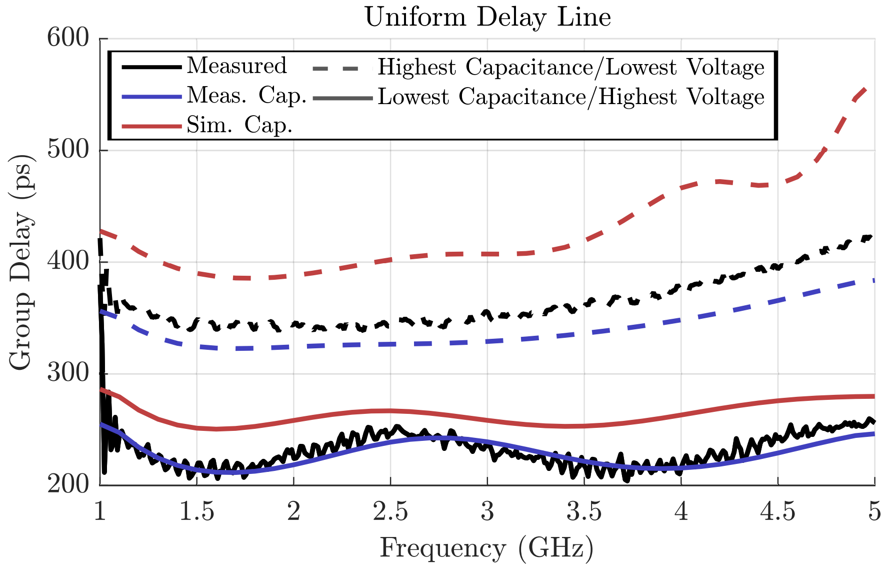

(a)

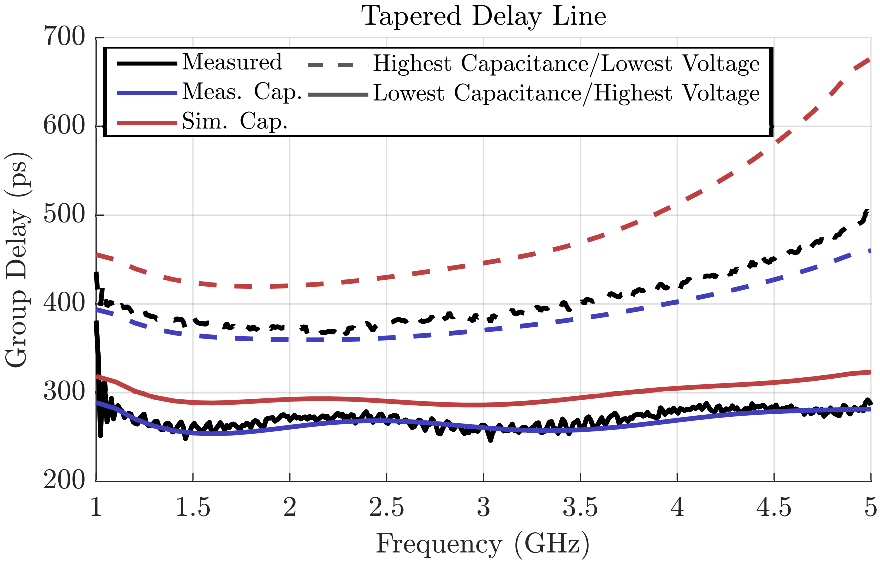

(b)

Figure 8.8: Measured (black), simulated with the measured capacitance, and simulated with the simulated capacitance (red) group delay for the uniform (a) and tapered (b) tunable delay-line MMICs, for a control voltage variation of -20 V (dashed) and +40 V (solid).

as well as in [100] which details the AISCs using these MMIC delay lines. In the next chapter these delay lines are used for two AISCs with an architecture described in Chapter 6.

CHAPTER 9

SINGLE-NOTCH AISC

9.1 INTRODUCTION

In this chapter, the two delay line MMICs from Chapter 7 are integrated in a hybrid 2–4 GHz analog interference suppression circuits (AISCs). Simulations using measured delay-line characteristics are compared with measurements of the full single-notch suppression circuit across the tuning range. The circuit is designed to have high power handling and high power performance as to operate under large interference signal conditions. Measurements are performed for two AISC circuits using the two different MMIC delay lines. In addition to small-signal characterization, two-tone signal measurements are also done to evaluate linearity, as well as measurements with two simultaneous signals.

9.2 INTERFERENCE SUPPRESSION CIRCUIT DESIGN

The analog interference suppression circuit (AISC) from Fig. 6.3(a) is designed using the circuit theory and the 2 to 4 GHz characterized in the previous section. The results of the simple theory are used to guide two designs using nolinear circuit simulations. One of the fabricated prototypes is shown in Fig. 9.1. The 2-4 GHz tunable notch designs have a 2:1 tuning ratio, which means that the n=0 null has to be chosen so that only one notch is present in the tuning band , where $\Delta\tau_1$ and $\Delta\tau_2$ are delays at the two edges of the frequency band and $\Delta\theta = 0$. For n=0 in Eq. (9.1), we obtain:

$$\Delta\tau_1 = 250\,\text{ps} \quad \text{and} \quad \Delta\tau_2 = 125\,\text{ps}. \tag{9.1}$$

To achieve this with the GaN MMIC uniform and tapered lines, having measured delays of 230-350 ps and 265-385 ps, the fixed delays of 478 ps and 518 ps are desired based on eqn. 9.1. However, taking into account the variable delay lines dispersion, the tuning range decreased from 2-4 GHz to 2-3.6 GHz. To account for this the fixed delay was reduced to 453 and 480 ps, for the uniform and tapered lines respectively. The amplitude imbalance between the lines degrades the notch performance, as predicted in Fig. 7.2 from Chapter 6. Since the attenuation of the variable lines varies over bias and frequency, a fixed average attenuation is applied. Finally, the dispersive attenuation of the variable delay lines is included into the model. The progression of the responses with the measured S-parameters of the delay lines and ideal other components are shown in Figs. 9.2 and 9.3.

The fixed delay lines are implemented with microstrip 50-Ω transmission lines. The fixed attenuation is 1.28 dB and 1.34 dB for the uniform and tapered delay-line circuits, respectively, and is determined from the loss in Paths 1 and 2 in Fig. 9.1. Surface-mount three-port dividers/combiners (MiniCircuits SEPS-2-63+) that operate from 0.68-6 GHz are chosen because of their high power handling capability of 5 W. The MMICs are epoxied directly on the 2-layer 20-mil 4350B Rogers' substrate, and bonded to the 50-Ω microstrip traces.

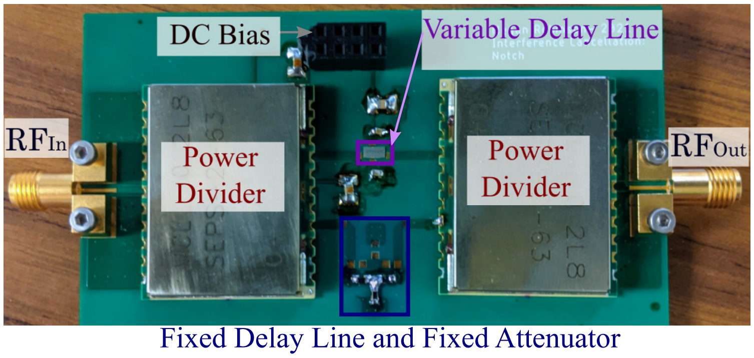

Figure 9.1: Photograph of the printed circuit boards showing surface mount reflectionless 3-dB couplers, the uniform delay line GaN MMIC in Path 1, and fixed delay lines (total delay of 433 ps) and attenuator (1.28 dB) in Path 2. A similar board is fabricated for the tapered delay line MMIC, with a different delay (463 ps) and attenuation (1.35 dB) in Path 2.

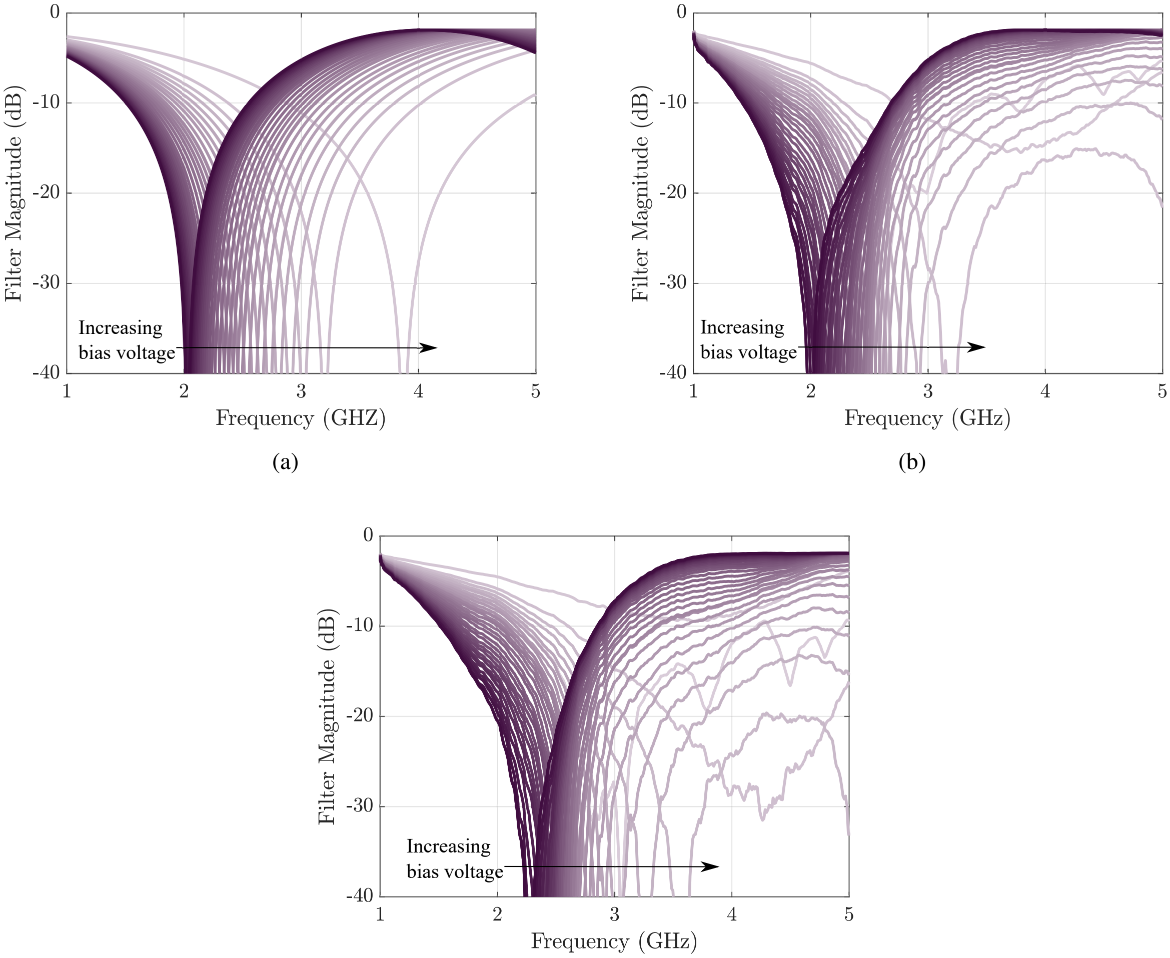

(a)

(b)

(c)

Figure 9.2: Performance of model with ideal lines with the fixed delay path has a time delay of 478 ps and attunation of 1.28 dB. The variable delay line is non dispersive plotted with a fixed amplitidue and delay equal to the average delay over frequency at each voltage. (b) Same fixed delay lines with frequency dependent delay of the measured uniform delay MMIC (c) The notch performance with the fixed delay changed to 453 ps with the full measured S-parameters including frequency dependent delay and attenuation included.

The fixed attenuator is achieved by a Tee network of surface-mount 0603 resistors, with series resistors of 3.6 Ω and 4.3 Ω, and parallel resistors of 330 Ω and 360 Ω, for the uniform and the tapered delay-line circuits, respectively. The bias and control lines contain blocking capacitors.

When fabricating the hybrid circuits, it is important to plate the traces with ENEPIG (Electroless Nickel Electroless Palladium Immersion Gold) for ease of bonding from the mounted MMICs directly to the printed circuit boards (PCBs). Since the active elements do not draw a lot of current or generate a significant amount

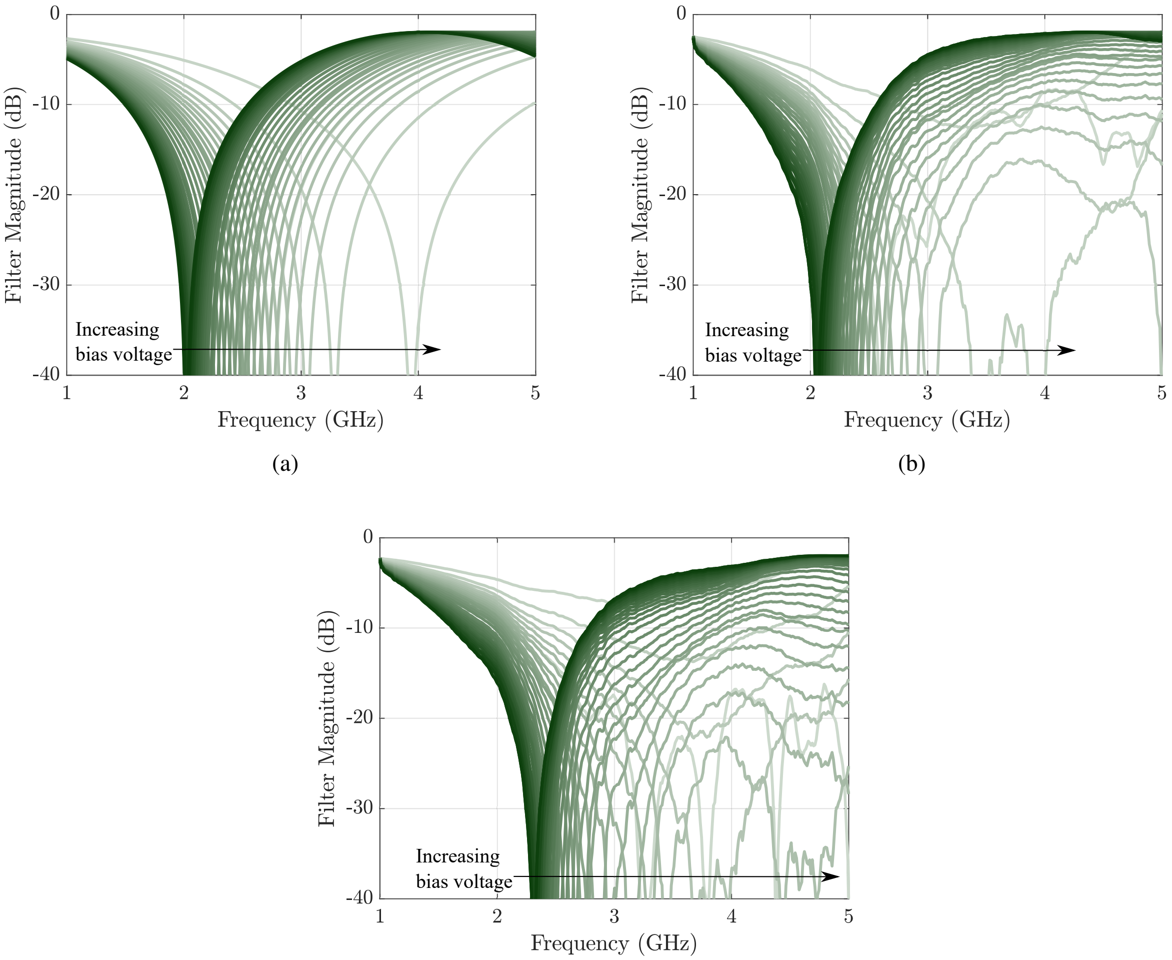

(a)

(b)

(c)

Figure 9.3: Performance of model with ideal lines with the fixed delay path has a time delay of 518 ps and attunation of 1.28 dB. The variable delay line is non dispersive plotted with a fixed amplitidue and delay equal to the average delay over frequency at each voltage. (b) Same fixed delay lines with frequency dependent delay of the measured tapered delay MMIC (c) The notch performance with the fixed delay changed to 480 ps with the full measured S-parameters for the tapered delay including frequency dependent delay and attenuation included.

of heat, the MMICs are mounted using two-component silver epoxy directly onto a via grounded metal pad on the PCB. Additionally, the MMIC is mounted first and then wire bonded before the surface mounted components are soldered on by hand. The reason is that the additional components can get in the way of the bonding tip while the wire bonds are formed. Finally, a plastic shield is placed over the MMICs to prevent dust from damaging the bonds during testing and storage.

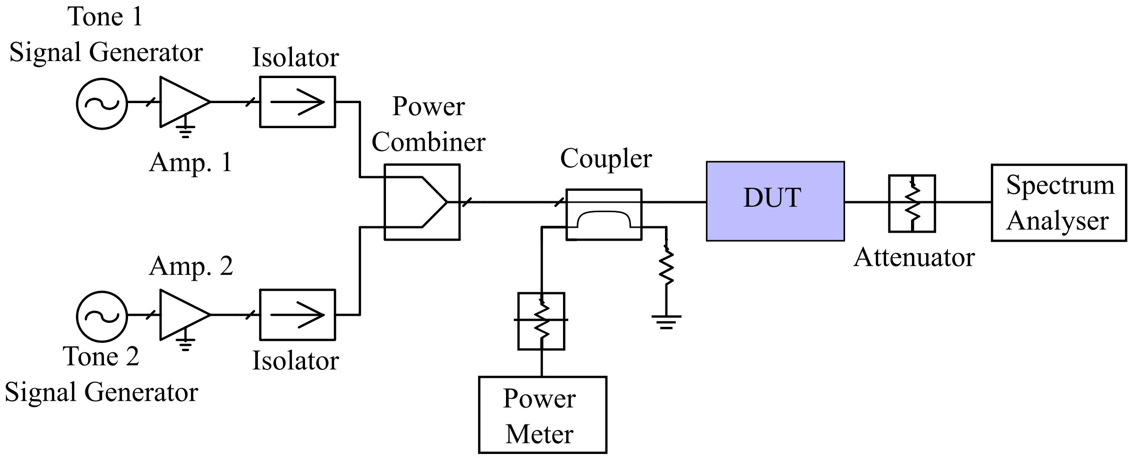

Figure 9.4: Block diagram of the two tone set up used for large signal and non-linear characterization of the AISCs.

9.3 Measured Circuit Performance

Next, the hybrid circuit from Fig. 9.1 is characterized experimentally. Following small-signal measurements, the linearity of the circuits is characterized using 2-tone measurements. The small signal performance, the Agilent E8364C PNA with a 3.5 SOLT calibration from 1 to 5 GHz is used. The large signal measurements are done using a two-tone bench set up as described in Fig. 9.4. It is important to have the isolators after the amplifiers in both tone paths in order to reduce the mixing of the two tones in the driver amplifiers. This in turn means that the spectrum analyser video bandwidth and resolution bandwidth are reduced to lower the noise floor in order to detect the low power intermodulation products of the AISCs.

9.3.1 Small-Signal Simulations and Measurements

Small-signal simulations are performed with measured MMIC delay line S-parameters, and including 0.1 nH bond-wire inductances at input and output. Manufacturer-provided S-parameters for the resistors and dividers are used in the simulations. Fig. 9.5 shows $|S_{11}|$ with a comparison to measurements of the full circuits. A similar comparison is shown for $|S_{21}|$ in Fig. 9.6. The notches tune over 2.24-4 GHz for the uniform line AISC and 2.32-4.13 GHz for the tapered line AISC. The attenuation at the desired notch frequencies is greater than -30 dB. The uniform-line circuit shows deeper notches with variable depth across frequency,

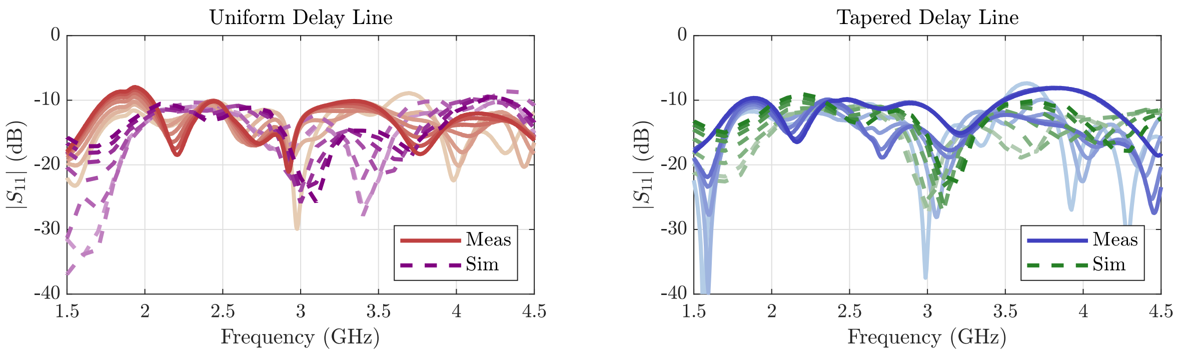

(a) (b)

Figure 9.5: Measured (solid) and simulated (dashed) $|S_{11}|$ for the interferometer circuits with uniform (a) and tapered (b) MMIC delay lines over the -20 V to $+40$ V control voltage range in 10 V steps.

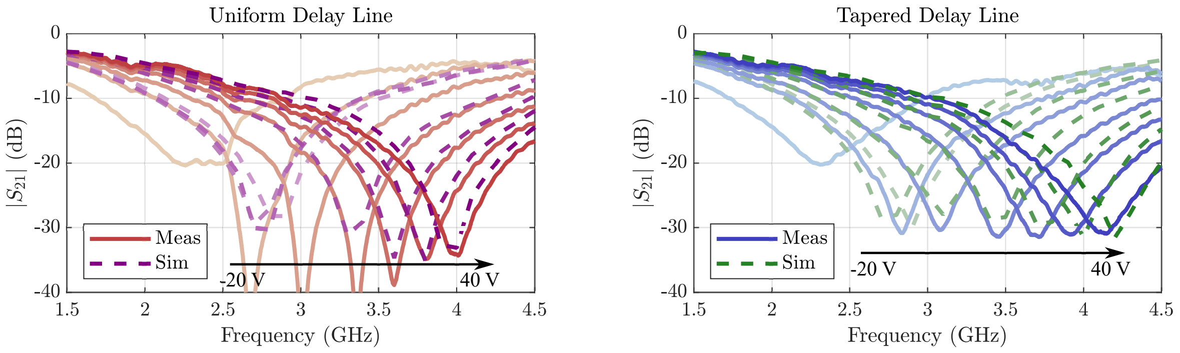

(a) (b)

Figure 9.6: Measured (solid) and simulated (dashed) $|S_{21}|$ for the interferometer circuit with uniform (a) and tapered (b) MMIC delay lines over the -20 V to +40 V control voltage range in 10 V steps.

while the tapered-line circuit exhibits a consistent notch depth over the tuning range. We define the insertion loss of the circuit, IL_{LOW}, as the loss at the lowest notch frequency, when the notch is set to the highest frequency . A similar insertion loss IL_{HIGH} can be defined for the complementary case. For the uniform-line AISC, $IL_{\text{LOW}} = 5.01$ dB and $IL_{\text{HIGH}} = 4.48$ dB, while the tapered-line AISC measures $IL_{\text{LOW}} = 6.16$ dB and $IL_{\text{HIGH}} = 5.31$ dB. Note that the notch depth degrades for control voltages below -18 V, due to the HEMT varactors starting to conduct, increasing the loss.

The uniform-line circuit shows deeper notches with variable depth across frequency, while the tapered-line circuit exhibits a consistent notch depth across a wider tuning range. A deep notch depths requires a perfect match in terms of the losses of the two paths of the interferometer, so an improved notch depth can be expected with fine tuning of the fixed path attenuator, which was not attempted here.

9.3.2 Nonlinear Characterization

Since the GaN interference suppression circuit is the first component in the receive chain after the LNA, it is important to characterize its linearity. The first step is to verify that the circuit operates under large signal input. Fig. 9.7 shows a comparison of the small and large-signal transmission coefficient for two simultaneous 25 dBm tones spaced 500 MHz apart. Very similar results are obtained for other tone frequencies across the band at the same spacing. For a larger tone spacing of 1 GHz, Fig. 9.8 shows the same comparison. The notch performance remains very similar between the small signal and large signal measurements.

A two-tone measurement is next performed with P_{in} = 22-26 dBm in each tone with a 10 MHz tone spacing. Fig. 9.9 shows the measured results and calculated 3rd order intercept point (IP3) at 3 GHz for -20, 10, and 40 V control voltages along with the control voltage associated with the 3 GHz notch, -2 and -4 V for the tapered and uniform delay lines respectively. Note that for the control voltage corresponding to the notch, the fundamental output signal amplitude is reduced due to the notch effect. However, the nonlinear components created by the varactors in the variable delay line branch of the interferometer do not cancel and hence the IMD3 products are unaltered, resulting in a lower IIP3 for that control setting.

Fig. 9.10 shows the IIP3 as a function of control voltage for tones centered at 2.5, 3, and 3.5 GHz, with the notch control voltages labeled for the three frequencies. Similar results are obtained at other frequencies within the octave. Note the degradation in linearity for low control voltages between -20 and -10 V due to the low negative reverse bias of the FET making the varactor susceptible to reverse conduction in this bias region. The total IIP3 observed in Fig. 9.10 is therefore the superposition of the increased nonlinearity for low control voltages, and the linear effect of the notch attenuation as discussed before.

9.4 Chapter Summary

In this chapter, two hybrid AISCs are demonstrated using GaN MMIC delay lines. The notches are tunable across 2.24-4 GHz range for the uniform delay line and 2.32-4.13 GHz for the tapered design with depth

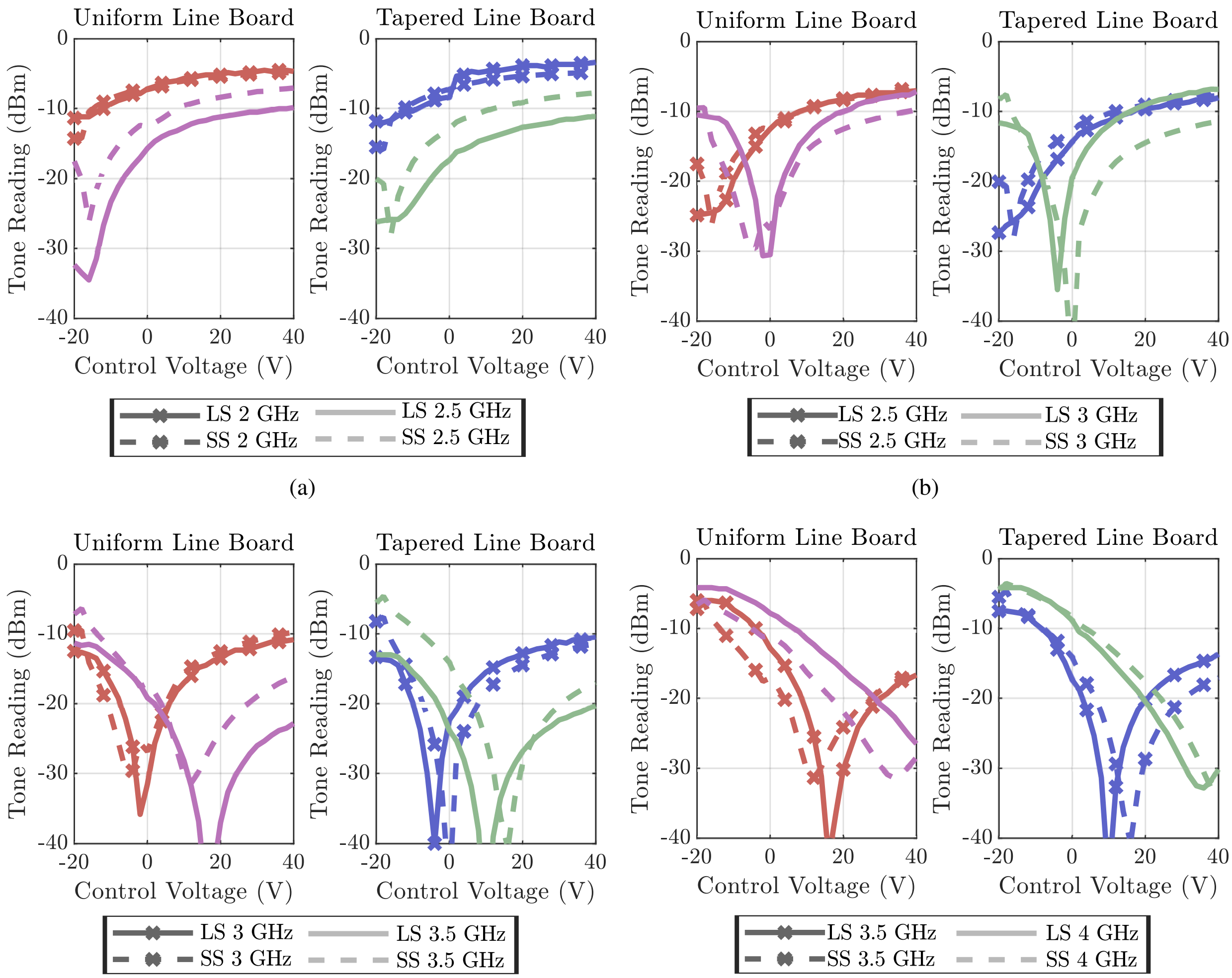

(a) (b)

(c) (d)

Figure 9.7: Large signal measurements (solid line) for 25 dBm input power per tone, compared to small-signal S-parameters (dashed line). The $|S_{21}|$ is shown for the uniform (left) and tapered (right) tunable delay line MMIC circuits with simultaneous large signal tones spaced 500 MHz apart; (a) at 2 and 2.5 GHz, (b) at 2.5 and 3, (c) at 3 and 3.5 GHz, and (d) at 3.5 and 4 GHz.

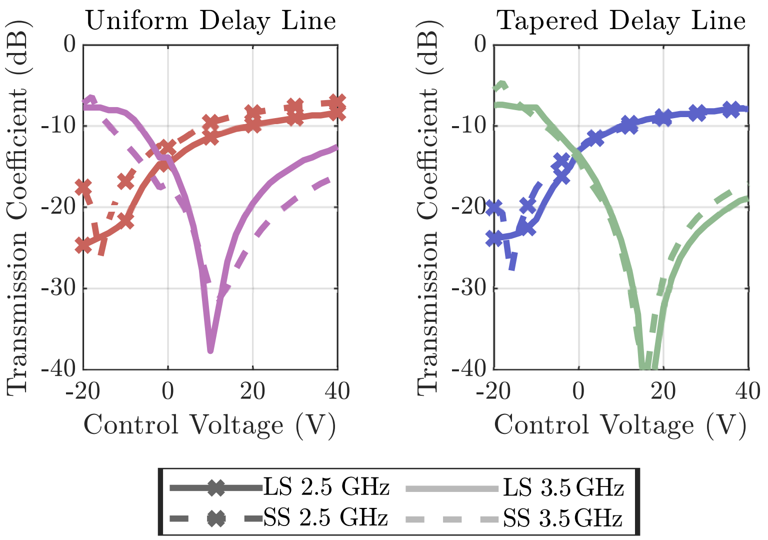

Figure 9.8: Large signal measurements (solid line) for 25 dBm input power per tone, compared to small-signal S-parameters (dashed line). The $|S_{21}|$ is shown for the uniform (left) and tapered (right) tunable delay line MMIC circuits with simultaneous large signal tones at 2.5 and 3.5 GHz.

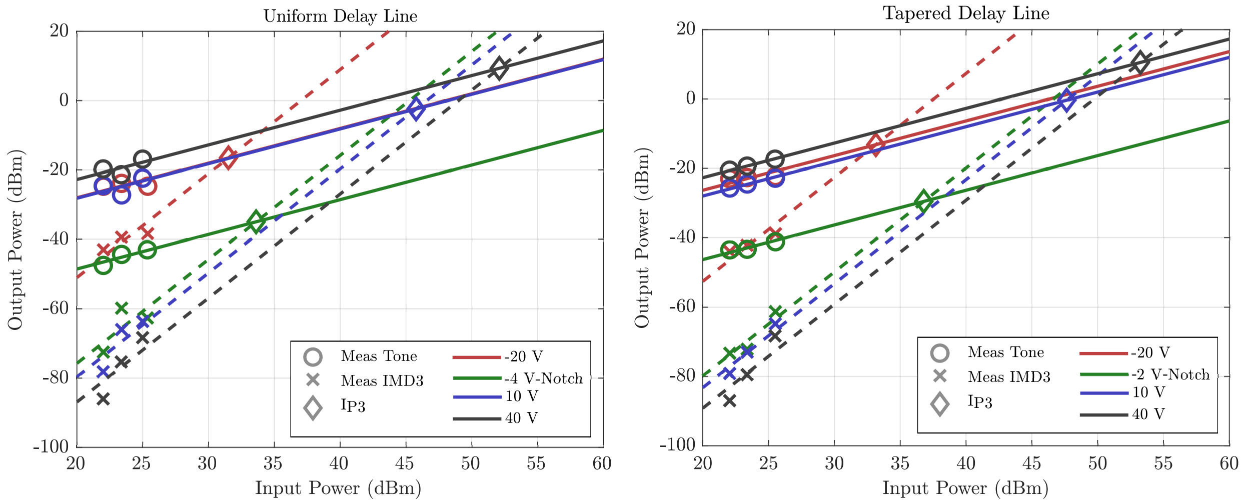

(a)

(b)

Figure 9.9: The measured signal and 3rd order mixing product results and calculated 3rd order intercept point at 3 GHz for -20, 10, and 40 V control voltages along with the control voltage associated with the 3 GHz notch, -4 and -2 V for the for the uniform delay line (a) and tapered delay line (b) respectively.

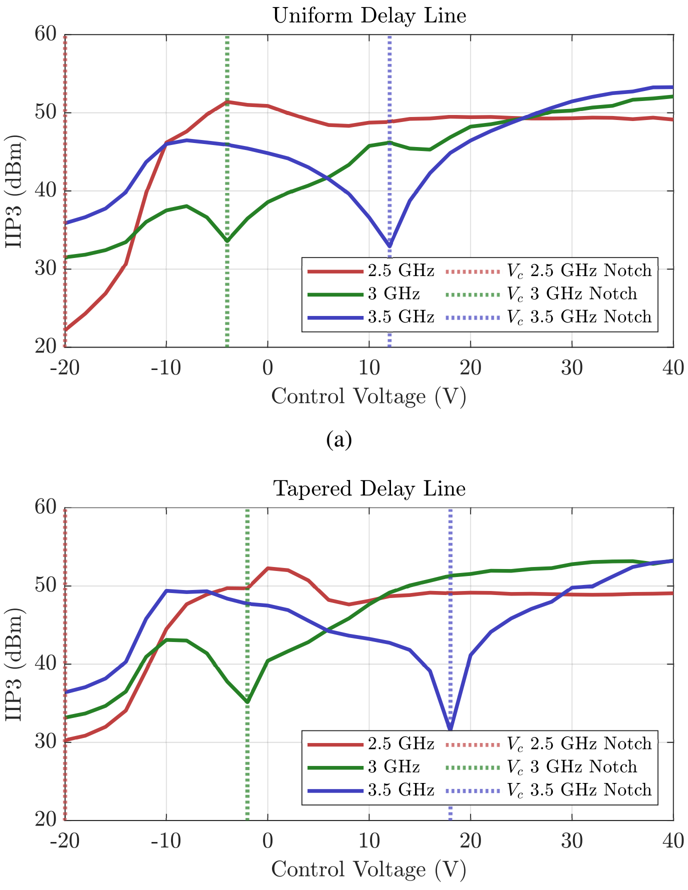

(a)

(b)

Figure 9.10: Measured IIP3 results of a 10 MHz spaced two tone signal centered at 2.5, 3, and 3.5 GHz for the uniform delay line (a) and tapered delay line (b).

between 25 and 40 dB. These AISCs are designed with a wide notch to suppress a single interferer or multiple interfering signals close in frequency. The contributions from this chapter are reported partially in [101] describing a fully monolithic higher frequency 6–12 GHz GaAs AISC MMIC, as well as in [100] which details the hybrid AISCs using GaN MMIC delay lines.

CHAPTER 10

PART II: CONCLUSIONS AND FUTURE WORK

10.1 INTRODUCTION

This chapter summarizes the work in interference suppression presented in Part II of the thesis. Several possible extensions to the AISC architecture are also discussed. Extending off of the single notch AISC a design of the two tunable notch circuit block diagram is shown in Fig. 7.9, where a four-branch interferometer includes a gain stage in each branch followed by a tunable delay lie. Using the interferometer theory combing four tunable delay lines with fixed gain amplifiers will allow for two tunable notches over the 2–4 GHz. The delays are adjusted to provide subtraction of signals at the output at two distinct frequencies.

10.2 EXTENSION OF AISC TO TWO-SIGNAL SUPPRESSION

The circuit is designed on a 20 mil Rogers 4350b substrate with gain provided by MiniCircuits PMA3-83MP+ amplifiers that cover 0.4 to 8 GHz with a drop in gain from 20 – 18.8 dB from 2 to 4 GHz. The 1-4 power divider/combiner is implemented with three microstrip Wilkinson dividers. Fixed microstrip delay lines are meandered symmetrically around the variable delay lines, which are hybridly integrated MMICs mounted on the same circuit board, Fig. 10.1.

Using GaN MMIC delay lines described in chapter 7, the delay tuning of ±62.5 ps can be achieved over

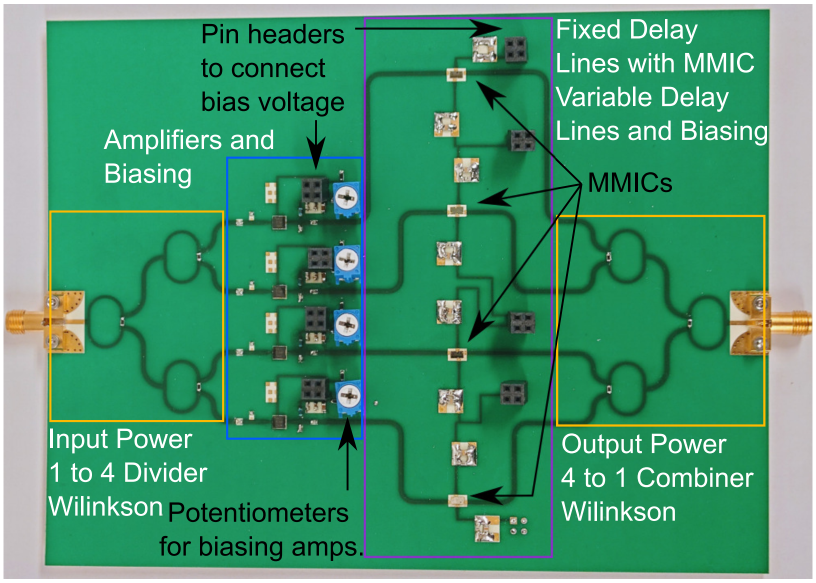

Figure 10.1: Picture of the tunable dual notch fabricated board sized 17.5 cm by 13.5 cm. The microstrip circuit is on a 20 mil Rogers 4350b substrate with 4 QFN amplifiers and 4 GaN MMICs mounted onto the PCB.

the 2–4 GHz desired tuning bandwidth. Briefly, these MMICs implemented in the WIN Semiconductors NP15 process are artificial transmission line $L-C$ networks with 7 sections and with varactor-connected HEMTs in shunt. Four MMICs are mounted with silver epoxy in the circuit and bonded to the 50-Ω microstrip lines. The notch frequencies depend on the voltage bias applied to each line to create the specified time delays. This can be calculated from measurements of the variable delay lines. For the overall delay in each path, equations (7.16) and (7.17) are used to solve for the variable delay based on the notch frequency setting with $C_1 = 477.5$ ps. The simulated delay in each line as a function of the notch frequencies is shown in Fig. 10.2, where each colored line corresponds to a fixed f_2.

Subtracting the fixed delay in each path, implemented through a fixed-length microstrip line, the variable delay is used to calculate voltage settings for the MMICs in each path. The voltage is inversely related to the delay. The trends of the voltage settings for the four lines depending on the two notch frequencies is graphed in Fig. 10.3. Unlike the single interferometer notch the relationship between the voltage and notch frequency are not intuitively related. The delays in path 1 and 4 depend on the sum of the inverse frequencies, eq. (7.16). However the delays in paths 2 and 3 depend on the differences in the inverse frequencies, eq. (7.17).

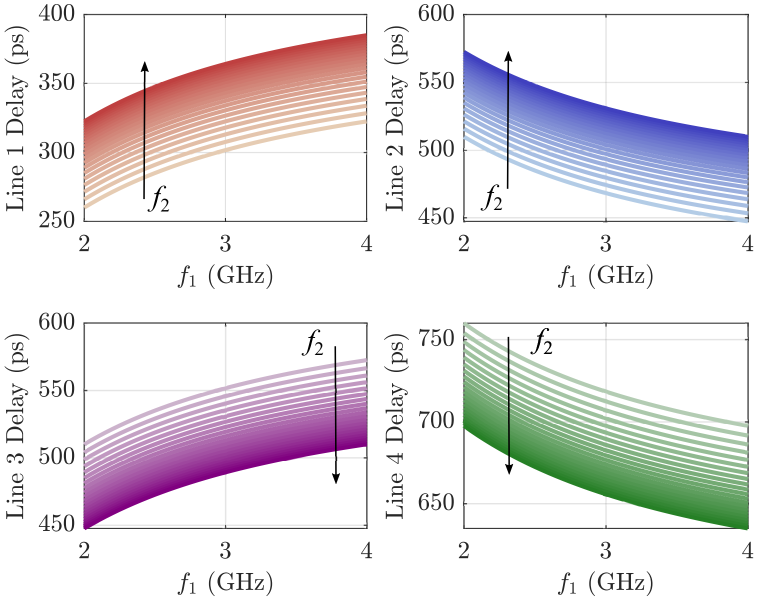

Figure 10.2: Plot of the desired time delay in each path for different notch frequency combinations f_1 and f_2. These were calculated using eqs. (7.16) and (7.17), while holding f_2 and sweeping f_1.

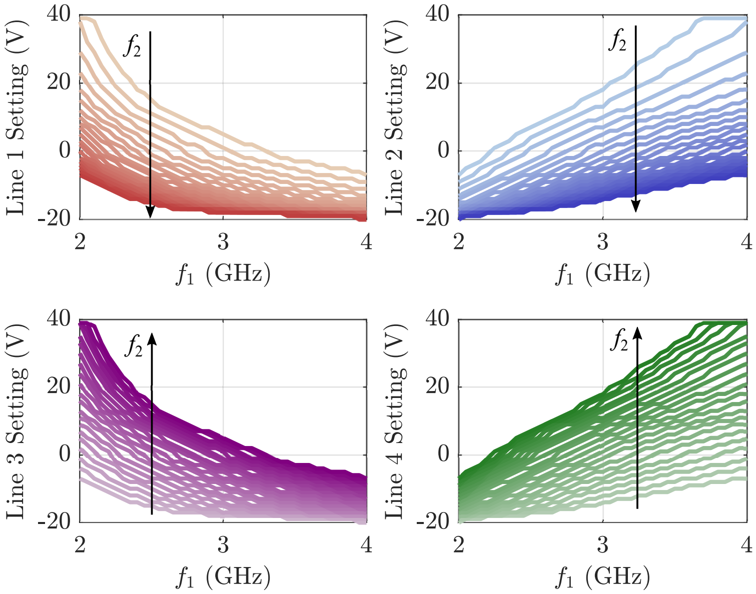

Figure 10.3: Plot of the desired voltage bias in applied to each path for different notch frequency combinations f_1 and f_2. These were calculated using eqs. (7.16) and (7.17), while holding f_2 and sweeping f_1 and subtracting the fixed delay in each path.

10.2.1 Measured Circuit Performance

Small-signal characterization of the hybrid circuit from Fig. 10.1 are performed with a 3.5-mm SOLT calibration and compared to simulations in Fig. 10.4. The simulations are performed with measured MMIC delay line S-parameters, and including 0.1 nH bond-wire inductances at inputs and outputs. Manufacturer-provided S-parameters for the resistors and amplifiers are used. The measured and simulated results were done using the voltage settings in Fig. 10.3. The match remains bellow 9 dB over the measured 1 to 5 GHz range. It is limited by the input match of the chosen broadband amplifier and barely changes with the notch setting. The ideal circuit response resulting from ideal power splitters, amplifiers and delay lines show that the simple theory predicts circuit behavior. The depth of the notch is less than the ideal case, but is predicted in simulation. The measured notch is below 10 dB for all notch settings.

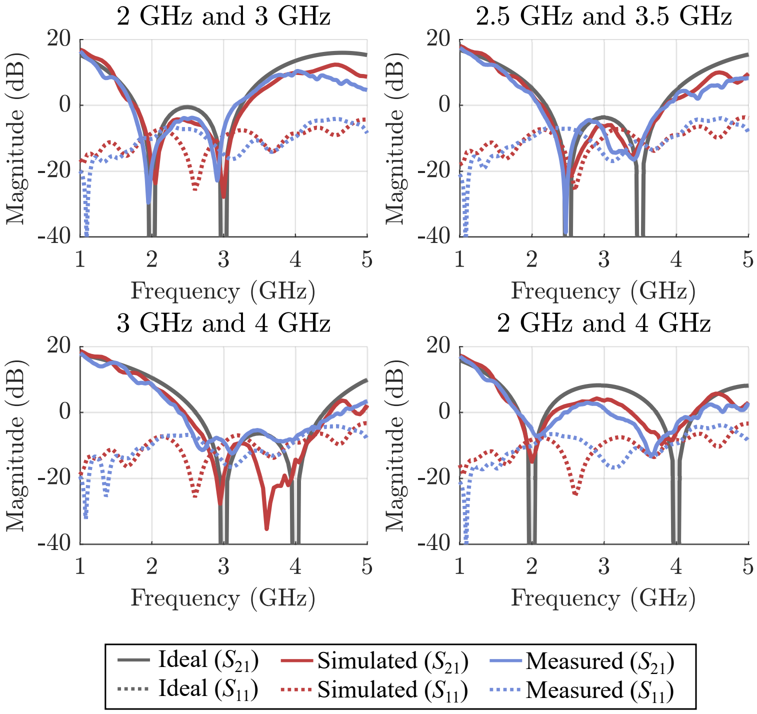

Figure 10.4: Small signal performance of dual notch circuit over frequency with the notch set at the combinations of notch frequencies f_1 and f_2, 2 and 3 GHz, 2.5 and 3.5 GHz, 3 and 4 GHz, and 2 and 4 GHz. Comparing an ideal circuit, simulated PCB, and measured PCB.

For incoming signals with no need for interference suppression, the delays in each path can be set as to create a passband at the signal frequency. For the two edge cases this is shown in Fig. 10.5, though the response can be tuned for signals in the center of the band maintaining gain above 10 dB.

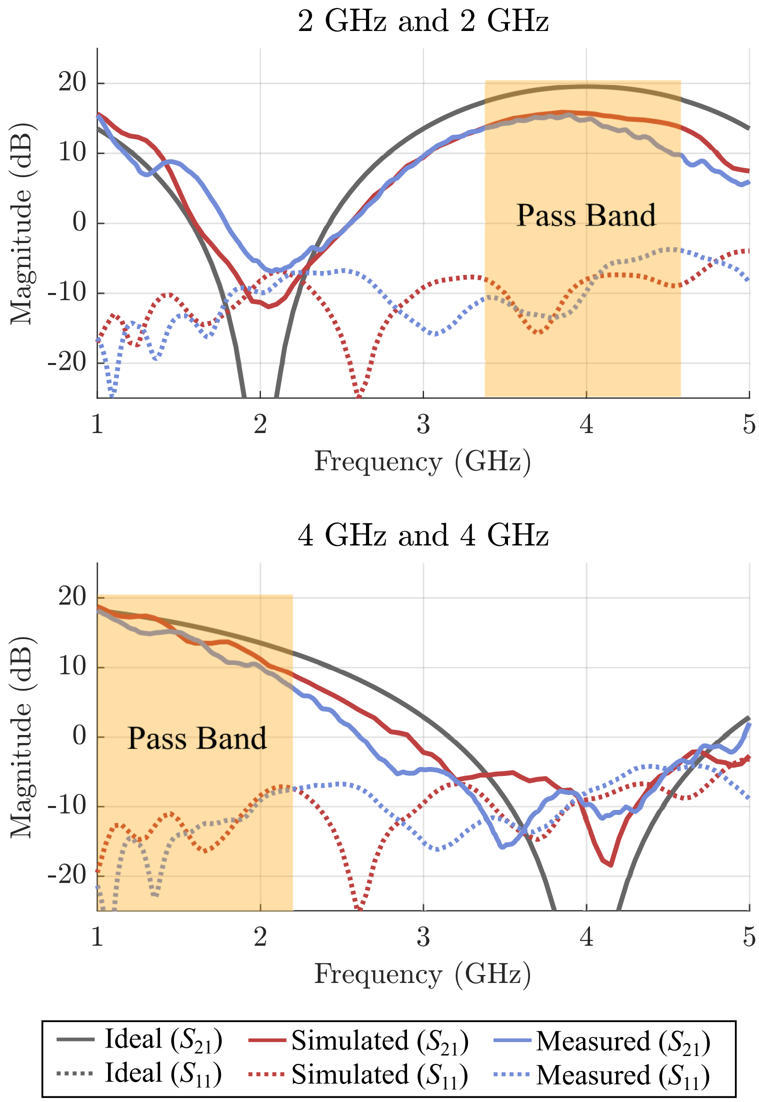

Figure 10.5: Small signal performance of dual notch circuit over frequency with the notch set at the edges of the tuning range f_1 and f_2, 2 and 2 GHz and 4 and 4 GHz. Comparing an ideal circuit, simulated PCB, and measured PCB depicting the passband operation in these two cases.

10.3 AISC Future Work

10.3.1 Tuning speed of the notch

The switching speed of the notch is based on the RC time constant of the variable capacitors and biasing structure. The bias structure was not designed specifically with this is mind and for that reason could be improved. For this reason the inherent switching time of the line, the switching time with the on chip bias, and the switching time including the off chip bias are reported. The minimum potential switching time of the MMICs without redesign, including the on chip bias, is 4.4 ns for the uniform delay line and 3.8 ns for the tapered delay line. The actual time constant of the AISC presented here including the off chip biasing is 66 ns. While this is very fast for a tunable notch, this tuning speed has not been measured. Future work on the bias voltage controls and delay line performance could enable realizable fast switching times for an integrated AISC.

10.3.2 Sensing frequency of the interfering signal

The AISC can be used in a full system that can detect the frequency of the unwanted signal as quickly as possible and suppress it. With the current AISC implementation, sweeping the notch frequency and measuring the receiver power can relate the notch frequency to the incoming unwanted signal. However, this takes time and during this time the system would not be receiving the desired signal. For jammers that are intentionally hopping frequencies this becomes a problem and could be improved by coupling off some of the power in one of the paths. The fixed attenuator in the single notch AISC can be replaced by a coupler to measure the incoming frequencies in real time. Other methods and feedback control can be investigated for integrating sensing within the AISC.

10.3.3 Simultaneous self and external suppression

The AISCs presented here are designed specifically to suppress external out-of-band interference. For many systems the power from the transmitter couples into the receive path and saturates the LNA or mixer, or masks the desired signal. The first power combiner in the AISC can be replaced with a hybrid coupler with two inputs. One input can be connected to a tapped signal from the transmit side with the other input connected to the antenna. If there is phase and amplitude control of the tapped transmit signal, then the single notch AISC tuning could simultaneously cancel self and external interference.

10.4 PART II SUMMARY AND CONCLUSIONS

Part II of this thesis presents simulation and measurement results of a 2-4 GHz octave bandwidth interference suppression circuit. The circuit accomplishes the function of a tunable frequency notch though an interferometer architecture. The relative delay in the interferometer paths is varied with GaN MMIC tunable delay lines. The delay is adjusted by varying the drain voltage of cold-FET connected HEMTs acting as varactors. Two types of periodically-loaded delay lines are compared: a uniform and a tapered design. A simple theoretical study, relating the delays and amplitudes in the interferometer circuit branches, is developed to inform the design. Two interference suppression hybrid circuits are implemented and measurements demonstrate a 25-40 dB notch across the 2.24-4 GHz range for the uniform delay line, and 2.32-4.13 GHz for the tapered design. The return loss for both designs remains below 10 dB. The circuit can handle an input power of 37 dBm and maintains performance with two simultaneous 25 dBm tones spaced 0.5 GHz apart. Linearity is characterized with 10 MHz two-tone measurements and the circuit demonstrates a 3rd-order intercept input power larger than 30 dBm for bias voltages above -12 V. The tunable delay lines that are the basis of the interferometer circuits are demontrasted at 28 GHz and in a phase shifter covering 6-12 GHz showing the viability of scaling to higher frequencies with some reduction in linearity and increased loss. Finally, the AISC topology is expanded to a dual notch configuration including LNAs in the 2–4 GHz octave band. The circuit reduces the power of an interfering signal by at least 10 dB, while amplifying the desired signal by as much as 18 dB. The noise figure ranges from 5–8.5 dB across the octave band and is comparable to similar active tunable circuits in a similar frequency range [102]. Table 10.1 compares published tunable bandstop filters in a similar frequency range, highlighting quantities usually missing in literature, namely the power handling and linearity of the AISCs.

Table 10.1: Comparison with prior work in tunable bandstop filters

Ref.	**Topology**	**Tuning Range (GHz)**	**Voltage Range (V)**	**Suppression (dB)**	**Notch BW BW (MHz)**	**Noise Figure (dB)**	**Power Handling**	**IIP3 (dBm)**
[103]	Gyrator	1.8–2.2	-1.2 to -0.2	35	50	-	-	-
[104]	MEMS-coupled line	3.5–6.5	0 to 17	11	550	< 1	0.1 dBm	10
[105]	MEMS-stripline	1.2–2.6	0 to 65	40	140	< 0.8	-	>25
[106]	Piezoelectric-cavity	3–6	-	60	-	0.37	-	-
[107]	Piezoelectric-SIW cavity	1.57-3.18	0 to 90	47	50	< 2	-	-
[108]	PIN-tuned stubs	0.5–2	1.3 to 27.4	30	200	-	-	-
[109]	Varactor-microstrip	1.8–2	-20 to 0	50	200	<2	-	-
[110]	Varactor-microstrip	1.9–2.6	0 to 15	25	45-160	5.4	-	-
[111]	Varactor-split ring	0.5–2.5	0 to 28	25	500	-	-	-
Uniform	2-path (AISC)	2.2–4	-20 to 40	35	1000	5.01	37 dBm	> 30
Tapered	2-path (AISC)	2.3–4.1	-20 to 40	30	1000	6.16	37 dBm	> 20
[102]	CMOS-N-path	0.2–1.2	Digital Switches	50	50	4.5–6.5	-	0
Dual Notch	4-path (AISC)	2–4	-20 to 40	25	1000	5–8.5	-	> 30

The interferometer topology presented here has a broad tuning range and is inherently absorptive with the major benefit being the high IIP3 compared to similar work. The few reported values are significantly lower, e.g. in [104] a maximum voltage of 1.6 V_{pp} on the MEMS is reported, which corresponds to 0.1 dBm of input power; [91] states 2.6 dBm for a feedforward integrated LNA design. The limitation of this circuits presented here is the bandwidth of the notch. Through the simplified circuit analysis the addition of a phase offset could sharpen the notch, but would affect the tuning range and pass band performance. The addition of a tunable resonance in one or both paths could allow for a frequency dependent phase and create a narrower notch. The use of GaN delay lines allows for high power, broadband interference suppression that can work with other interference mitigation techniques to aid broadband receivers exposed to high power interferers.

10.5 CONTRIBUTIONS

- **The interferometer based AISC can supress high power interference.** The single notch AISC demonstrated tone suppression with two tones of 25 dBm each, power handling up to 5 W, and an IIP3 above 20 dBm for the uniform delay AISC and 30 dBm for the tapered delay AISC.
- **The interferometer based AISC is able to supress signals over the 2–4 GHz octave bandwidth.** Wide tuning bandwidths are difficult to achieve and both AISCs were able to suppress more than 15 dB across the 2–4 GHz band with more than 30 dB suppression between 2.6 and 4.1 GHz.
- **Integration of LNA into the AISC design can improve loss and noise performance.** Showed extension of AISC to two simulataneous notches with included LNAs and investigated effect of dual notch architecture on noise performance.
- **Variable delay lines and therefore the AISC can be scaled in frequency.** Demonstrated a 28 GHz delay line MMIC and a 6–12 GHz delay line based phase shifter MMIC. Both of these the delay line circuits indicate the scalability of the AISC topology in frequency.

The contributions from this work are reported in [99, 101, 112] and in publications currently under review [100, 113].

BIBLIOGRAPHY

[1] A. M. Paz, S. Trabelsi, S. O. Nelson, and E. Thorin, “Measurement of the dielectric properties of sawdust between 0.5 and 15 GHz,” *IEEE Transactions on Instrumentation and Measurement*, vol. 60, no. 10, p. 3384–3390, 2011. ix, 13

[2] S. Trabelsi, “Frequency and temperature dependence of dielectric properties of chicken meat,” in *2012 IEEE International Instrumentation and Measurement Technology Conference Proceedings*, 2012, pp. 1515–1518. ix, 13

[3] A. Reyes, M. Yarlequé, W. Castro, and S. Chuquizuta, “Determination of permittivity values using microwave dielectric spectroscopy for assessing apple and purple sweet potato quality parameters,” in *2018 International Conference on Electromagnetics in Advanced Applications (ICEAA)*, 2018, pp. 593–596. ix, 13

[4] S. O. Nelson, “Dielectric spectroscopy of fresh fruit and vegetable tissues from 10 to 1800 MHz,” *Journal of Microwave Power and Electromagnetic Energy*, vol. 40, no. 1, p. 31–47, 2005. ix, 13

[5] M. Sabet and H. Soleimani, “Mechanical and electrical properties of low density polyethylene filled with carbon nanotubes,” *IOP Conference Series: Materials Science and Engineering*, vol. 64, p. 012001, 2014. ix, 13

[6] H. Saghlatoon, L. Sydanheimo, L. Ukkonen, and M. Tentzeris, “Optimization of inkjet printing of patch antennas on low-cost fibrous substrates,” *IEEE Antennas and Wireless Propagation Letters*, vol. 13, p. 915–918, 2014. ix, 13

[7] J. Algie, “Dielectric constant and conductance changes in wool fibers produced by step changes in the relative humidity,” *Textile Research Journal*, vol. 34, no. 6, p. 477–486, 1964. ix, 13

[8] *CHAPTER 9 THERMAL PROPERTIES OF FOODS*. American Society of Heating, Refrigeration and Air-Conditioning Engineers, 2006. ix, 13

[9] S. O. Keskin, S. O. Keskin, G. Sumnu, G. Sumnu, S. Sahin, and S. Sahin, “A study on the effects of different gums on dielectric properties and quality of breads baked in infrared-microwave combination oven,” *European Food Research and Technology*, vol. 224, no. 3, pp. 329–334, 2007. ix, 13

[10] O. Sipahioglu, S. Barringer, and C. Bircan, “The dielectric properties of meats as a function of temperature and composition,” *Journal of Microwave Power and Electromagnetic Energy*, vol. 38, no. 3, pp. 161–169, 2003. ix, 13, 27

[11] T. V. Koutchma and V. V. Yakovlev, “Computer modeling of microwave heating processes for food preservation,” in *Mathematical Modeling of Food Processing*. M.M. Farid, Ed. CRC Press, 2010, pp. 625–658. ix, 28

[12] M. Celuch and P. Kopyt, “Modeling microwave heating in foods,” in *Development of Packaging and Products for Use in Microwave Ovens*. M.W. Lorence and P.S. Pesheck, Eds, Woodhead Publishing, 2009, p. 305–348. ix, 28

[13] V. V. Yakovlev, S. M. Allan, M. L. Fall, H. S. Shulman, and J. Tao, “Computational study of thermal runaway in microwave processing of zirconia,” in *Microwave and RF power applications*. J. Tao, Ed., Cépaduès Éditions Toulouse, 2011, pp. 303–306. ix, 28

[14] P. Kopyt and M. Celuch, “Coupled electromagnetic-thermodynamic simulations of microwave heating problems using the FDTD algorithm,” *Journal of Microwave Power and Electromagnetic Energy*, vol. 41, no. 4, p. 18–29, 2007. ix, 28

[15] H. Wang, T.-Y. Huang, N. S. Mannem, J. Lee, E. Garay, D. Munzer, E. Liu, Y. Liu, B. Lin, M. Eleraky, H. Jalili, J. Park, S. Li, F. Wang, A. S. Ahmed, C. Snyder, S. Lee, H. T. Nguyen,

and M. E. D. Smith, “Power amplifiers performance survey 2000-present.” [Online]. Available: https://gems.ece.gatech.edu/PA_survey.html x, 2

[16] S. Taranovich, “Si vs. GaN vs. SiC: Which process and supplier are best for my power design?” Jun 2020. [Online]. Available: https://www.edn.com/si-vs-gan-vs-sic-which-process-and-supplier-are-best-for-my-power-design/ x, 3

[17] A. Moore and E. Reese, “Rf applications of gan for dummies,” Qorvo, Tech. Rep., 05 2014. x, 4

[18] M. Ives, “Recyclers cringe as southeast asia says it’s sick of the west’s trash,” Jun 2019. [Online]. Available: https://www.nytimes.com/2019/06/07/world/asia/asia-trash.html x, 8

[19] A. Nakagawa, “Ocean plastic: What you need to know,” Feb 2023. [Online]. Available: https://www.ecowatch.com/ocean-plastic-guide-2653277768.html x, 8

[20] “National overview: Facts and figures on materials, wastes and recycling,” Mar 2020. [Online]. Available: https://www.epa.gov/facts-and-figures-about-materials-waste-and-recycling/national-overview-facts-and-figures-materials#NationalPicture x, 7, 8, 9

[21] J. F. Sopko, C. Hagel, L. J. Austin, J. F. Campbell, and T. P. Bostick, “Final assessment: What we have learned from our inspections of incinerators and use of burn pits in afghanistan,” Feb 2015. [Online]. Available: https://www.sigar.mil/pdf/alerts/SIGAR-15-33-AL.pdf x, 8, 10

[22] “Bioenergy : Bioenergy : Research.” [Online]. Available: https://engineering.purdue.edu/LORRE_Dev/research/bioenergy/prototypes x, 10

[23] M. Ives, “Recyclers cringe as southeast asia says it’s sick of the west’s trash,” Jun 2019. [Online]. Available: https://www.nytimes.com/2019/06/07/world/asia/asia-trash.html 7

[24] R. H. . T. Edgington, “Recycling: Where is the plastic waste mountain?” Jan 2019. [Online]. Available: https://www.bbc.com/news/science-environment-46566795 7

[25] “Ocean plastics.” [Online]. Available: https://www.nps.gov/subjects/oceans/ocean-plastics.htm 7

[26] M. Igarashi, Y. Hayafune, R. Sugamiya, Y. Nakagawa, and K. Makishima, "Pyrolysis of Municipal Solid Waste in Japan," *Journal of Energy Resources Technology*, vol. 106, no. 3, pp. 377–382, 09 1984. 8

[27] J. J. Valdes and J. Warner, "Tactical garbage to energy refinery," Jan 2009. 8, 9

[28] "Waste-to-energy machine reveals power of trash." [Online]. Available: https://www.army.mil/article/165910/waste_to_energy_machine_reveals_power_of_trash 8

[29] "Stennis' waste management saves money, environment," May 2011. [Online]. Available: https://stennis74.wordpress.com/2011/05/10/stennis-waste-management-saves-money-environment/ 9

[30] D. Czajczyńska, T. Nannou, L. Anguilano, R. Krzyżyńska, H. Ghazal, N. Spencer, and H. Jouhara, "Potentials of pyrolysis processes in the waste management sector," *Energy Procedia*, vol. 123, p. 387–394, 2017. 9, 13

[31] J. C. Solarte-Toro, Y. Chacón-Pérez, and C. A. Cardona-Alzate, "Evaluation of biogas and syngas as energy vectors for heat and power generation using lignocellulosic biomass as raw material," *Electronic Journal of Biotechnology*, vol. 33, p. 52–62, 2018. 9

[32] A. L. Tasca, M. Puccini, R. Gori, I. Corsi, A. M. R. Galletti, and S. Vitolo, "Hydrothermal carbonization of sewage sludge: A critical analysis of process severity, hydrochar properties and environmental implications," *Waste Management*, vol. 93, p. 1–13, 2019. 9

[33] Z. Wang, J. Cao, and J. Wang, "Pyrolytic characteristics of pine wood in a slowly heating and gas sweeping fixed-bed reactor," *Journal of Analytical and Applied Pyrolysis*, vol. 84, no. 2, p. 179–184, 2009. 9

[34] A. Sarkar and R. Chowdhury, "Co-pyrolysis of paper waste and mustard press cake in a semi-batch pyrolyzer—optimization and bio-oil characterization," *International Journal of Green Energy*, vol. 13, no. 4, p. 373–382, 2014. 10, 18

[35] S. Barışçı and M. S. Öncel, "The disposal of combed cotton wastes by pyrolysis," *International Journal of Green Energy*, vol. 11, no. 3, p. 255–266, Mar 2013. 10, 15, 18

[36] S. A. Opatokun, V. Strezov, and T. Kan, "Product based evaluation of pyrolysis of food waste and its digestate," *Energy*, vol. 92, p. 349–354, 2015. 10, 18

[37] J. A. Onwudili, N. Insura, and P. T. Williams, "Composition of products from the pyrolysis of polyethylene and polystyrene in a closed batch reactor: Effects of temperature and residence time," *Journal of Analytical and Applied Pyrolysis*, vol. 86, no. 2, p. 293–303, 2009. 10, 13, 18

[38] Y. Fernandez, A. Arenillas, and J. Angel, "Microwave heating applied to pyrolysis," *Advances in Induction and Microwave Heating of Mineral and Organic Materials*, 2011. 10

[39] H. B. Sharma, S. Panigrahi, and B. K. Dubey, "Hydrothermal carbonization of yard waste for solid bio-fuel production: Study on combustion kinetic, energy properties, grindability and flowability of hydrochar," *Waste Management*, vol. 91, p. 108–119, 2019. 10

[40] C. Liu, H. Huang, Z. Liu, F. Huo, and K. Huang, "Experimental study on microwave power combining based on injection-locked 15-kW S-band continuous-wave magnetrons," *IEEE Transactions on Plasma Science*, vol. 44, no. 8, p. 1291–1297, 2016. 10, 55

[41] "RF cooking with Goji." [Online]. Available: http://www.gojifoodsolutions.com/ 10

[42] E. F. Brown, "The next-generation consumer microwave oven: A review," *Journal of Microwave Power and Electromagnetic Energy*, vol. 56, no. 2, p. 82–86, 2022. 11

[43] Jan 2014. [Online]. Available: https://www.sandiego.gov/sites/default/files/legacy/environmental-services/pdf/recycling/CompMilitary.pdf 13

[44] C. Song, W. Pan, and S. T. Srimat, "Tri-reforming of natural gas using CO_2 in flue gas of power plants without CO_2 pre-separation for production of synthesis gas with desired h2/co ratios," *Environmental Challenges and Greenhouse Gas Control for Fossil Fuel Utilization in the 21st Century*, p. 247–267, 2002. 13

[45] M. J. Franco, “An 80% power efficient, 125-watt, GaN-based RF power amplifier designed for continuous duty and linear operation on L-band,” in *2013 IEEE MTT-S International Microwave Symposium Digest (MTT)*, 2013, pp. 1–3. 13

[46] H. Jeong, T. Yoon, H. Yoo, H. Jung, and S. Cho, “A highly efficient and compact 6kW GaN solid-state microwave generator for CW 2.45 GHz applications,” in *2019 IEEE MTT-S International Microwave Symposium (IMS)*, 2019, pp. 572–575. 13

[47] C. Liu, H. Huang, Z. Liu, F. Huo, and K. Huang, “Experimental study on microwave power combining based on injection-locked 15-kW S-band continuous-wave magnetrons,” *IEEE Transactions on Plasma Science*, vol. 44, no. 8, p. 1291–1297, 2016. 14

[48] M. Robinson and Z. Popović, “Scalable microwave waste-to-fuel conversion,” in *Proc. AMPERE 2019; 17th Annual Conference on Microwave and High Frequency Heating*, 2019. 20, 62

[49] K. Halden, A. De Alwis, and P. Fryer, “Changes in the electrical conductivity of foods during ohmic heating,” *International Journal of Food Science & Technology*, vol. 25, no. 1, pp. 9–25, 1990. 27

[50] J. M. Catalá-Civera, A. J. Canós, P. Plaza-González, J. D. Gutiérrez, B. García-Baños, and F. L. Peñaranda-Foix, “Dynamic measurement of dielectric properties of materials at high temperature during microwave heating in a dual mode cylindrical cavity,” *IEEE Transactions on Microwave Theory and Techniques*, vol. 63, no. 9, pp. 2905–2914, 2015. 27, 29

[51] QuickWave, QWED Sp. z o. o., 1998-2021. [Online]. Available: http://www.qwed.eu/ 28

[52] E. M. Moon, C. Yang, and V. V. Yakovlev, “Microwave-induced temperature fields in cylindrical samples of graphite powder – experimental and modeling studies,” *Intern. J. of Heat & Mass Transfer*, vol. 87, no 8, pp. 359–368, 2015. 28

[53] M. T. Porter, J. Binner, P. Kumi, K. E. Stern, and V. V. Yakovlev, “Computational characterization of microwave-enhanced CVI production of SiCf/SiC composites,” *Proc. 18th AMPERE Conference*

on Microwave and High Frequency Heating (Virtual, September 2021), pp. 48–55, 10.5281/zenodo.5 716 071. 28

[54] P. Kumi, S. A. Martin, V. V. Yakovlev, M. S. Hilario, B. W. Hoff, and I. M. Rittersdorf, "Electromagnetic-thermal model of a millimeter-wave heat exchanger based on an AlN: Mo susceptor," *COMPEL-The Intern. J. for Computation and Math in Electrical and Electronic Engng*, vol. 39, no. 2, pp. 481–496, 2020. 28

[55] C. M. Hogan, B. Hoff, I. Rittersdorf, and V. V. Yakovlev, "Computational characterization of a millimeter-wave heat exchangers with AlN:Mo susceptor of multiple cylindrical elements," *J. Microwave Power & Electromagnetic Energy*, vol. 56, no. 1, pp. 18–36, 2022. 28

[56] L. A. Bronckers and A. B. Smolders, "Broadband material characterization method using a cpw with a novel calibration technique," *IEEE Antennas and Wireless Propagation Letters*, vol. 15, pp. 1763–1766, 2016. 28

[57] P. K. Varshney and M. J. Akhtar, "A high q substrate integrated waveguide resonator for microwave sensing of low loss materials," in *2019 International Conference on Electrical, Electronics and Computer Engineering (UPCON)*, 2019, pp. 1–4.

[58] D. Marqués-Villarroya, F. Pcñaranda-Foix, A. J. Canós, B. García-Baños, and J. M. Catalá-Civera, "Determination of the complex permittivity of high loss liquids with a novel reentrant cavity," in *2018 IEEE/MTT-S International Microwave Symposium - IMS*, 2018, pp. 1381–1384.

[59] P. Kumi and V. V. Yakovlev, "Computational procedure for quantitative characterization of uniformity of high frequency heating," *Proc. 53rd IMPI's Microwave Power Symp. (Las Vegas, NV, June 2019*, pp. 123–125. 29

[60] M. C. Robinson, J. A. Molles, V. V. Yakovlev, and Z. Popović, "Solid-state power combining for heating small volumes of mixed waste materials," *IEEE Journal of Microwaves*, pp. 1–13, 2023. 32, 53, 62

[61] “Picolog 6 data logging software.” [Online]. Available: https://www.picotech.com/library/data-loggers/picolog-6-data-logger-software 34

[62] S. C. Cripps, *RF Power Amplifiers for Wireless Communications*, 2nd ed. Artech House, 2006. 39

[63] Z. Abbas, R. Pollard, and R. Kelsall, “Complex permittivity measurements at ka-band using rectangular dielectric waveguide,” *IEEE Transactions on Instrumentation and Measurement*, vol. 50, no. 5, pp. 1334–1342, 2001. 44

[64] M. Robinson, V. Yakovlev, and Z. Popović, “Experimental and computational study of microwave heating in single- stream waste processing,” in *Proc. 56*th *IMPI’s Annual Microwave Power Symp. (Savannah, GA, June 2022)*, pp. 52–54. 53, 62

[65] J. Molles, M. Robinson, and Z. Popović, “Experimental study of microwave heating in mixed waste materials,” in *Proc. 57*th *IMPI’s Annual Microwave Power Symp. (Denver, CO, June 2023)*. 53, 62

[66] “GaN on SiC solutions for S-band applications.” [Online]. Available: https://www.wolfspeed.com/products/rf/s-band/ 55

[67] “GaN HEMTs.” [Online]. Available: https://www.qorvo.com/products/discrete-transistors/gan-hemts#ta0041;;;aa0135:asc/ 55

[68] B. Henricksen, G. Scott, M. Irvine, and R. Santhakumar, “A 1.4kW, highly-efficient, GaN, partially-matched FET for L-band applications,” in *2018 IEEE/MTT-S International Microwave Symposium - IMS*, 2018, pp. 640–642. 55

[69] “QPD1025 data sheet.” [Online]. Available: https://www.qorvo.com/products/discrete-transistors/gan-hemts#ta0041;;;aa0135:asc/ 55

[70] “CGHV40200 data sheet.” [Online]. Available: https://assets.wolfspeed.com/uploads/2020/12/CGHV40200PP.pdf 55

[71] H. Sun, C. Gu, Z. Li, Q. Xu, J. Song, B. Xu, X. Dong, K. Wang, and F. Martin, "Enhancing the number of modes in metasurfaced reverberation chambers for field uniformity improvement," *Sensors*, vol. 18, 09 2018. 57, 58

[72] S. Rani, A. Marwaha, and S. Marwaha, "Investigation of substrate materials for graphene oxide absorber loaded antenna array increased ambient temperature," *Photonic Network Communications*, vol. 40, no. 2, p. 94–102, 2020. 60

[73] Y. Yu, B. Han, and F. Xia, "PDC-SiAlCN ceramic based wireless passive temperature sensors using integrated resonator/antenna up to 1100°C," *Sensor Review*, vol. 40, no. 1, p. 62–70, 2020. 60

[74] J.-M. Boccard, T. Aftab, J. Hoppe, A. Yousaf, R. Hutter, and L. M. Reindl, "High-resolution, far-field, and passive temperature sensing up to 700 °C using an isolated zst microwave dielectric resonator," *IEEE Sensors Journal*, vol. 16, no. 3, p. 715–722, 2016. 60

[75] K. E. Kolodziej, *In-Band Full-Duplex Wireless Systems Handbook.* Artech House, 2021. 64, 65

[76] S. Garikapati, A. Gaonkar, A. Nagulu, T. Chen, G. Zussman, and H. Krishnaswamy, "Performance comparison of time-domain and frequency-domain RF self-interference cancellation in full-duplex wireless systems," in *2020 54th Asilomar Conference on Signals, Systems, and Computers*, pp. 1574–1578. 65

[77] M. Kunes and G. Connor, "A digitally controlled tunable high power output filter for space applications," in *1989 19th European Microwave Conference*, pp. 681–686. 65

[78] D. Psychogiou, R. Gómez-García, and D. Peroulis, "A class of fully-reconfigurable planar multi-band bandstop filters," in *2016 IEEE MTT-S International Microwave Symposium (IMS)*, pp. 1–4. 65

[79] T. Yang and G. M. Rebeiz, "Bandpass-to-bandstop reconfigurable tunable filters with frequency and bandwidth controls," *IEEE Transactions on Microwave Theory and Techniques*, vol. 65, no. 7, pp. 2288–2297, 2017. 65

[80] H. Darabi, A. Mirzaei, and M. Mikhemar, “Highly integrated and tunable RF front ends for reconfigurable multiband transceivers: A tutorial,” *IEEE Transactions on Circuits and Systems I: Regular Papers*, vol. 58, no. 9, pp. 2038–2050, 2011. 65

[81] S. Reynolds, P. Pepeljugoski, J. Schaub, J. Tierno, and D. Beisser, “A 7-tap transverse analog-FIR filter in 0.12 μm CMOS for equalization of 10Gb/s fiber-optic data systems,” in *ISSCC. 2005 IEEE International Digest of Technical Papers. Solid-State Circuits Conference, 2005.*, pp. 330–601 Vol. 1. 65

[82] A. Momtaz and M. M. Green, “An 80 mw 40 Gb/s 7-tap t/2-spaced feed-forward equalizer in 65 nm CMOS,” *IEEE Journal of Solid-State Circuits*, vol. 45, no. 3, pp. 629–639, 2010. 65

[83] J. Lee and A. Freundorfer, “MMIC adaptive transversal filtering using Gilbert cells and is suitable for high-speed lightwave systems,” *IEEE Photonics Technology Letters*, vol. 12, no. 2, pp. 196–198, 2000. 65

[84] A. Nagulu, A. Gaonkar, S. Ahasan, S. Garikapati, T. Chen, G. Zussman, and H. Krishnaswamy, “A full-duplex receiver with true-time-delay cancelers based on switched-capacitor-networks operating beyond the delay–bandwidth limit,” *IEEE Journal of Solid-State Circuits*, vol. 56, no. 5, pp. 1398–1411, 2021. 65

[85] M. Darvishi, R. van der Zee, E. A. M. Klumperink, and B. Nauta, “Widely tunable 4th order switched G $_m$-C band-pass filter based on n-path filters,” *IEEE Journal of Solid-State Circuits*, vol. 47, no. 12, pp. 3105–3119, 2012. 65

[86] M. C. M. Soer, E. A. M. Klumperink, Z. Ru, F. E. van Vliet, and B. Nauta, “A 0.2-to-2.0 GHz 65nm CMOS receiver without LNA achieving >>11dBm IIP3 and <<6.5 dB NF,” in *2009 IEEE International Solid-State Circuits Conference - Digest of Technical Papers*, 2009, pp. 222–223,223a. 65

[87] G. Lasser, R. Langwieser, R. Dallinger, and C. F. Mecklenbräuker, “Broadband leaking carrier cancellation for RFID systems,” in *2012 IEEE/MTT-S International Microwave Symposium Digest*, 2012, pp. 1–3. 65

[88] C. Andrews and A. C. Molnar, “A passive mixer-first receiver with digitally controlled and widely tunable RF interface,” *IEEE Journal of Solid-State Circuits*, vol. 45, no. 12, pp. 2696–2708, 2010. 66

[89] C. Wu, Y. Wang, B. Nikolić, and C. Hull, “An interference-resilient wideband mixer-first receiver with LO leakage suppression and I/Q correlated orthogonal calibration,” *IEEE Transactions on Microwave Theory and Techniques*, vol. 64, no. 4, pp. 1088–1101, 2016. 66

[90] Y. Lien, E. Klumperink, B. Tenbroek, J. Strange, and B. Nauta, “A mixer-first receiver with enhanced selectivity by capacitive positive feedback achieving +39dbm IIP3 and <3dB noise figure for SAW-less LTE radio,” in *2017 IEEE Radio Frequency Integrated Circuits Symposium (RFIC)*, 2017, pp. 280–283. 66

[91] H. Darabi, “A blocker filtering technique for SAW-less wireless receivers,” *IEEE Journal of Solid-State Circuits*, vol. 42, no. 12, pp. 2766–2773, 2007. 66, 107

[92] T. D. Werth, C. Schmits, R. Wunderlich, and S. Heinen, “An active feedback interference cancellation technique for blocker filtering in rf receiver front-ends,” *IEEE Journal of Solid-State Circuits*, vol. 45, no. 5, pp. 989–997, 2010. 66

[93] S. Ayazian and R. Gharpurey, “Feedforward interference cancellation in radio receiver front-ends,” *IEEE Transactions on Circuits and Systems II: Express Briefs*, vol. 54, no. 10, pp. 902–906, 2007. 66

[94] D. Bharadia, E. McMilin, and S. Katti, “Full duplex radios,” *SIGCOMM Comput. Commun. Rev.*, vol. 43, no. 4, p. 375–386, aug 2013. [Online]. Available: https://doi.org/10.1145/2534169.2486033 67

[95] C. S. Chu, Y. Zhu, R. Chu, K. Chen, and K. M. Lau, “GaN-based radio-frequency planar interdigitated metal-insulator-semiconductor varactors,” in *Proceedings. 7th International Conference on Solid-State and Integrated Circuits Technology, 2004.*, vol. 3, pp. 2257–2260. 80

[96] R. Amirpour, D. Schwantuschke, F. Van Raay, P. Brueckner, R. Quay, and O. Ambacher, “Large-signal modeling of a scalable high-Q AlGaN/GaN high electron-mobility varactor,” *IEEE Transactions on Microwave Theory and Techniques*, vol. 67, no. 3, pp. 922–927, 2019. 80

[97] A. Hamdoun, M. Himidi, R. Langis, and O. Lafond, “Large signal and analytic non-linear modelling of GaN HEMT-based varactors,” in *2019 IEEE International Conference on Electron Devices and Solid-State Circuits (EDSSC)*, pp. 1–3. 80

[98] R. Amirpour, D. Schwantuschke, P. Brueckner, R. Quay, and O. Ambacher, “High-Q anti-series AlGaN/GaN high electron-mobility varactor,” in *2019 IEEE MTT-S International Microwave Symposium (IMS)*, pp. 599–602. 80

[99] M. Robinson, P. Danielson, and Z. Popović, “Continuous broadband GaAs and GaN MMIC phase shifters,” *IEEE Microwave and Wireless Components Letters*, vol. 32, no. 1, pp. 56–59, 2022. 86, 107

[100] M. Robinson, G. Lasser, and Z. Popović, “Linear broadband interference suppression circuit based on GaN MMICs,” *IET Circuits, Devices Systems*, vol. 1. 88, 98, 107

[101] P. Danielson, M. Robinson, G. Lasser, and Z. Popović, “GaAs MMIC interferometer for broadband interference suppression,” in *2022 17th European Microwave Integrated Circuits Conference (EuMIC)*, 2022, pp. 17–20. 98, 107

[102] M. N. Hasan, Q. J. Gu, and X. Liu, “Tunable blocker-tolerant rf front-end filter with dual adaptive notches for reconfigurable receivers,” in *2016 IEEE MTT-S International Microwave Symposium (IMS)*, 2016, pp. 1–4. 105, 106

[103] F. Giannini, E. Limiti, G. Orengo, and P. Sanzi, “High-Q gyrator-based monolithic active tunable bandstop filter,” *IEE Proceedings - Circuits, Devices and Systems*, vol. 145, no. 4, p. 243, 1998. 106

[104] Z. Wu, Y. Shim, and M. Rais-Zadeh, “Miniaturized UWB filters integrated with tunable notch filters using a silicon-based integrated passive device technology,” *IEEE Transactions on Microwave Theory and Techniques*, vol. 60, no. 3, pp. 518–527, 2012. 106, 107

[105] C.-C. Cheng and G. M. Rebeiz, “A three-pole 1.2–2.6-GHz RF MEMS tunable notch filter with 40-db rejection and bandwidth control,” *IEEE Transactions on Microwave Theory and Techniques*, vol. 60, no. 8, pp. 2431–2438, 2012. 106

[106] M. D. Hickle and D. Peroulis, “Tunable absorptive bandstop filter with an ultra-broad upper passband,” in *2017 IEEE MTT-S International Microwave Symposium (IMS)*, 2017, pp. 733–736. 106

[107] M. F. Hagag, M. Abdelfattah, and D. Peroulis, “Balanced octave-tunable absorptive bandstop filter,” in *2018 IEEE 19th Wireless and Microwave Technology Conference (WAMICON)*, 2018, pp. 1–4. 106

[108] B. Carey-Smith and P. Warr, “Broadband-configurable bandstop-filter design employing a composite tuning mechanism,” *IET Microwaves, Antennas & Propagation*, vol. 1, no. 2, p. 420, 2007. 106

[109] D. R. Jachowski and C. Rauscher, “Frequency-agile bandstop filter with tunable attenuation,” in *2009 IEEE MTT-S International Microwave Symposium Digest*, 2009, pp. 649–652. 106

[110] T. Yang and G. M. Rebeiz, “A 1.9–2.6GHz filter with both bandpass-to-bandstop reconfigurable function and bandpass-and-bandstop cascading function,” in *2017 IEEE MTT-S International Microwave Symposium (IMS)*, 2017, pp. 264–266. 106

[111] V. A., F. Aznar, D.-S. M., J. Bonache, and M. F., “Tunable coplanar waveguide band-stop and band-pass filters based on open split ring resonators and open complementary split ring resonators,” *IET Microwaves, Antennas & Propagation*, vol. 5, no. 3, p. 277, 2011. 106

[112] L. Marzall, M. Robinson, P. Danielson, A. Robinson, N. Ehsan, and Z. Popović, “Active and passive components for broadband transmit phased arrays: Broadband transmit front-end components,” *IEEE Microwave Magazine*, vol. 23, no. 2, pp. 56–74, 2022. 107

[113] M. Robinson, G. Lasser, and Z. Popović, “Tunable dual notch hybrid circuit based on GaN MMIC delay lines,” in *2023 European Microwave Conference (EuMC)*, 2023. 107